2016

Analysis of Benzopyrenes and Benzopyrene Metabolites by Fluorescence Spectroscopy Techniques

Bassam Al-Farhani
University of Central Florida

ANALYSIS OF BENZOPYRENES AND BENZOPYRENE METABOLITES BY FLUORESCENCE SPECTROSCOPY TECHNIQUES

by

BASSAM AL-FARHANI
B.Sc. Alnahrain University Iraq, 2002
M.Sc. Alnahrain University Iraq, 2005

A dissertation submitted in partial fulfilment of the requirements
for the degree of Doctor of Philosophy
in the Department of Chemistry
in the College of Sciences
at the University of Central Florida
Orlando, Florida

Spring Term
2016

Major Professor: Andres D. Campiglia

ABSTRACT

Polycyclic aromatic hydrocarbons (PAHs) are some of the most common and toxic pollutants encountered worldwide. Presently, monitoring is restricted to sixteen PAHs, but it is well understood that this list omits many toxic PAHs. Among the "forgotten" PAHs, isomers with molecular weight 302 are of particular concern due to their high toxicological properties. The chromatographic analysis of PAHs with MW 302 is challenged by similar retention times and virtually identical mass fragmentation patterns.

The first original component of this dissertation evolves from a high-resolution spectroscopic approach specifically developed to fulfil this gap. Herein, 4.2 K Laser-Excited Time-Resolved Shpol'skii Spectroscopy (4.2K LETRSS) is applied to the analysis of HMW-PAHs in a complex coal tar standard reference material (SRM 1597a). The spectral and lifetime information obtained with LETRSS provide the required selectivity for the unambiguous determination of PAH isomers in the high-performance liquid chromatography (HPLC) fractions. Complete LETRSS analysis is possible with microliters of HPLC fractions and organic solvent. The excellent analytical figures of merit associated to its non-destructive nature, which provides ample opportunity for further analysis with other instrumental methods, makes this approach a unique alternative for the analysis of isomers of HMW-PAHs in complex environmental samples.

The second original component of this dissertation focuses on the development of screening methodology for the routine analysis of PAH metabolites in urine samples. It explores the room-temperature fluorescence (RTF) properties of 3-hydroxy-benzo[*a*]pyrene, benzo[*a*]pyrene-*trans*-9,10-dihydrodiol, benzo[a]pyrene-r-7,t-8,c-9-tetrahydrotriol and benzo[*a*]pyrene-*r*-7,*t*-8,*c*-9,*c*-10-tetrahydrotetrol previously extracted with octadecyl-silica

membranes. RTF measurements from extraction membranes are carried out with the aid of fiber optic probe that eliminates the need for manual optimization of signal intensities. Relative standard deviations varying from 2.07% (benzo[a]pyrene-r-7,t-8,c-9-tetrahydrotriol) to 8.55% (3-hydroxy-benzo[*a*]pyrene) were obtained with a straightforward procedure. Analytical recoveries from human urine samples varied from 87.54 ± 3.11% (3-hydroxy-benzo[*a*]pyrene) to 99.77 ± 2.48% (benzo[*a*]pyrene-*r*-7,*t*-8,*c*-9,*c*-10-tetrahydrotetrol). The excellent analytical figures of merit and the simplicity of the experimental procedure demonstrate the potential of Solid phase extraction-RTF for screening biomarkers of PAH exposure in numerous urine samples.

This thesis is dedicated to

My wife

Israa

For her constant, unconditional support of my every endeavor

My lovely kids

Hayder and Baneen

For inspiring me to not give up and finish the raise

My parents and my father-in-law

For endless love

ACKNOWLEDGMENTS

I would like to express my sincerest gratitude to my advisor Prof. Andres D. Campiglia for his enormous help and support towards the fulfillment of my Ph.D. degree. For imparting his knowledge, time, patience, and enthusiasm towards our research work. To my dissertation committee: Dr. James Harper, Dr. Shengli Zou, Dr. Andrew Frazer and Dr. Woo Hyoung Lee, Thank You. It was such a privilege to have you on my dissertation committee.

I would like to thank the Iraqi government and the Higher Committee for Education development (HCED) for providing this opportunity and their continuous support.

I would like to thank the friends I gained during my PhD studies. You are too many to mention but you always touched my heart and made my days at UCF more enjoyable.

I would like to thank my lab mates and Chemistry colleagues for their valuable help: Dr. Brent Wilson, Dr. Anthony Moore, Dr. Ebrahim Ghazvini, Nirvani Mujumdar, Khang Trieu, Madelein Johnson, Maha Altammimi, Alaa Fadhel, Hugh Hayes and Luciano Violante.

Special thanks to my brothers, Yaqdhan, Ali and Sajad and my sisters, Ashwaq and Baidaa for their love and support.

Lastly, thank you Allah for everything you have given to me, Alhamdulillah.

TABLE OF CONTENTS

LIST OF FIGURES

LIST OF TABLES

CHAPTER 1. INTRODUCTION

1.1. Photoluminescence Phenomena

A partial Jablonski diagram, depicting the various activation and deactivation processes for an aromatic molecule, is shown in Figure 1[1]. An absorption, or excitation, process (A) can occur into the first or higher excited singlet state. Excitations into the first and second singlet states (S_1 and S_2) are shown. This process is relatively fast and it takes approximately 10^{-15} s. Following excitation, the molecule typically undergoes vibrational relaxation (VR) into the ground vibrational level of the electronic excited state. The excess of vibrational energy is converted to thermal and/or translational energy. VR occurs on the order of 10^{-11} to 10^{-10} s. If the molecule resides in an upper excited singlet state (S_2), internal conversion (IC) into the S_1 electronic level can occur. This process is efficient if the ground vibrational level of the S_2 state has the same energy as an upper vibrational lever of the S_1 state. The internal conversion process occurs on order of 10^{-12} s. Following IC, VR occurs into the ground vibrational level of the S_1 state.

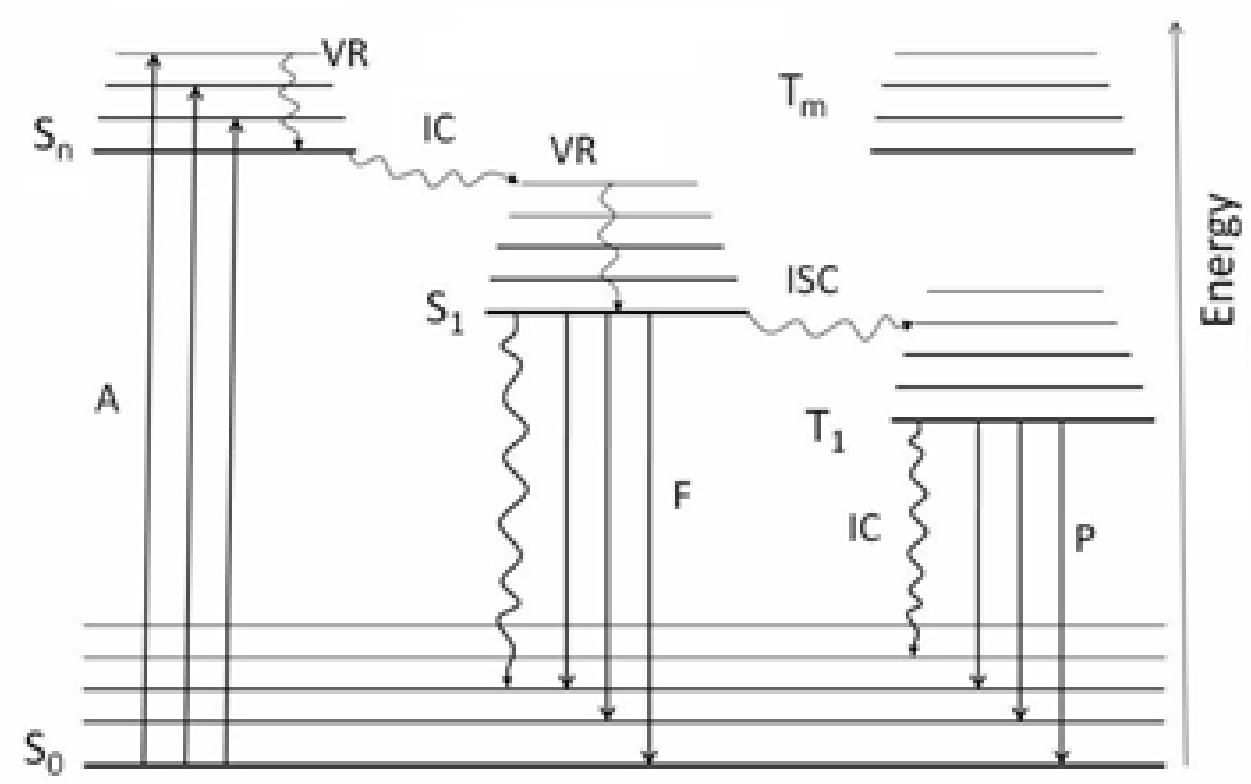

Figure 1. Jablonski diagram. A is absorption, F is fluorescence, P is phosphorescence, VR is vibrational relaxation, IC is internal conversion, and ISC is intersystem crossing.

From the S_1 state, deactivation of the molecule may happen through various processes. External conversion (EC) is a non-radiative deactivation process in which the excited molecule transfers its excess electronic energy to surrounding molecules or solvent molecules through collisions. From the lowest vibrational level of S_1, the molecule may also release the excess of electronic energy in the form of a photon. This process is known as fluorescence (F) and it occurs on order of 10^{-10} to 10^{-6}s. Since IC and VR are comparatively rapid process, fluorescence most often occurs from the ground vibrational lever of the first excited single state and it is of a longer wavelength than absorption. Fluorescence from the S_2 state is rare and will only occur if the energy gap between the S_1 and S_2 states is large enough that IC is not favoured.

The S_1 state also may be deactivated by a non-radiative process called inter-system crossing (ISC). This process involves a crossover of electronic states similar to IC but it occurs between states of different spin multiplicity. Population of the upper vibrational levels of the triplet state manifold is followed by VR and IC into the ground vibrational level of the first triplet excited state (T_1). Deactivation of T_1 via the emission of a photon is called phosphorescence (P) and it occurs on the order of 10^{-3} to 10^{3} s. Since phosphorescence occurs on a relatively long time scale, T_1 is particularly susceptible to collisional deactivations[2]. Non-radiative deactivation of T_1, or quenching, can be significant in the presence of oxygen. Molecular oxygen resides naturally in a ground triplet configuration possessing two low-lying singlet states with excitation energies of approximately 23 and 38 kcal/mol. Any species having excitation energy as low as 23 kcal/mol may be quenched by oxygen via energy transfer. Excited singlet states may also be affected by oxygen, but since oxygen quenching is diffusion controlled, a high oxygen concentration is necessary to quench the relatively short-lived excited singlet state.

The removal of oxygen is often accomplished through de-oxygenation of sample solution by purging the sample compartment with inert gasses. Similar to phosphorescence, fluorescence is always in competition with the various non-radiative deactivation processes of the excited state. As a result, fluorescence and phosphorescence intensities intrinsically depend on the relative efficiencies of all competing processes affecting their respective excited states. The efficiencies of fluorescence and phosphorescence are often expressed in terms of quantum yields (ϕ).

The quantum yield for fluorescence (ϕ_F) is the ratio between the rate of fluorescence and the rate of absorption, Φ_F/Φ_A, where $\Phi_F = k_F n_{S1} V$ and $\Phi_A = k_A n_{S0} V$. V is the volume of sample illuminated; n_{Sx} is the number of molecules occupying the given electronic state x; and k_F and k_A are the rates of fluorescence and absorption, respectively. Under steady state conditions, we can assume that $n_{S1} = n_{S0} k_A / (k_F + k_{nr})$, where k_{nr} is the sum of rates for the non-radiative processes (external conversion, k_{ec}; internal conversion, k_{ic}; and inter-system crossing, k_{isc}). Using these relationships, the fluorescence quantum yield in terms of the rate constants of the various activation and deactivation processes is given by equation (1.1):

$$\phi_F = \frac{k_F}{k_F + k_{nr}} \tag{1.1}$$

Which shows that, in order to improve the fluorescence quantum yield, and hence the fluorescence intensity, one needs to minimize the rate contributions from non-radiative processes .A similar situation arises for phosphorescence. The phosphorescence quantum yield (ϕ_P) can expressed as:

$$\phi_P = \frac{k_{isc}}{k_{isc} + k_F + k_{nr}} \times \frac{k_P}{k_P + k_{nr}} \tag{1.2}$$

Note that the first term in equation (1.2) takes into account the efficiency of inter-system crossing. Therefore, to maximize the phosphorescence efficiency, hence the phosphorescence intensity, minimization of both non-radiative processes and fluorescence relative to inter-system crossing becomes evident.

Because the excited states (S_1 and T_1) are often deactivated by first-order processes, the decay of either fluorescence or phosphorescence can described by equation (1.3):

$$I_t = I^0 e^{-t/\tau_L} \tag{1.3}$$

Where I_0 is the luminescence (fluorescence or phosphorescence) intensity at time zero and τ_L is the luminescence lifetime. The lifetime decay is defined as the time it takes for the luminescence signal to decay to 1/e of its initial value. The lifetimes for fluorescence and phosphorescence are related to the rate constants for deactivation by equations (1.4) and (1.5):

$$\tau_F = (k_F + k_{nr})^{-1} \tag{1.4}$$

$$\tau_P = (k_P + k_{nr})^{-1} \tag{1.5}$$

Equations (1.1), (1.2), (1.4) and (1.5) indicate that non-radiative decay processes decrease the fluorescence and phosphorescence intensities and lifetimes by the same factor. In other words, the lifetime and the quantum efficiency are proportional to $(k_L + k_{nr})^{-1}$.

1.2. Shpol'skii Spectroscopy

Apart from possible instrumental contributions, inhomogeneous and homogeneous broadening effects determine the spectral line-width in condensed phase electronic spectra. Inhomogeneous broadening is related to the fact that in a sample we are usually studying a large ensemble of molecules that – although chemically identical – may still show slightly different spectra. That is mainly the result of differences in the structure of the solvation shell surrounding the chromophore molecules: each individual molecule will experience a slightly different interaction with the solvent, resulting in a Gaussian distribution of transition energies (as illustrated in Figue 2a. In flexible molecules, the occurrence of different conformations may also play a role. However, when solute molecules adopt the same conformation and experience exactly the same environment, such as the one in a theoretically perfect crystalline matrix, their transition energies would coincide exactly, as shown in Figure 2b.

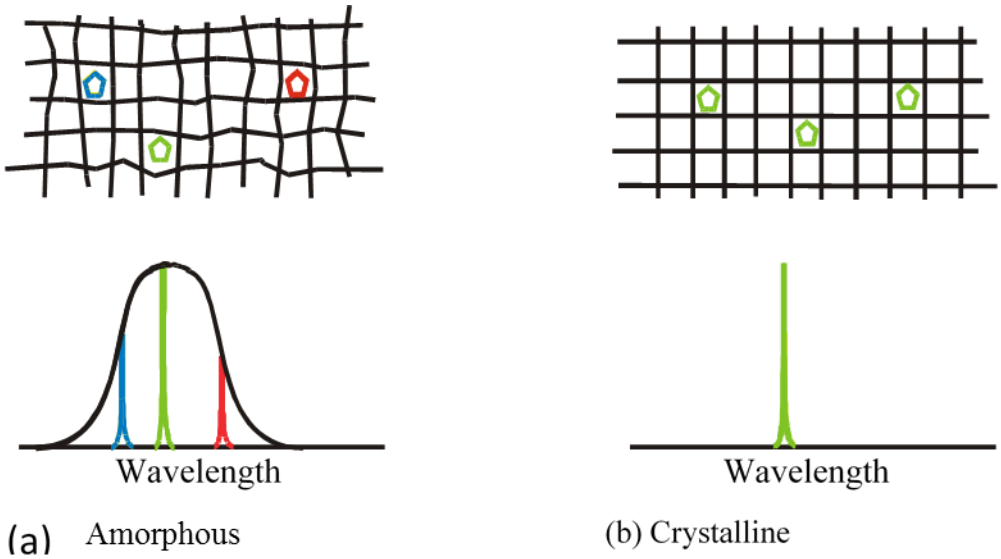

Figure 2. Cartoon of analyte in amorphous and crystalline matrix and resulting spectral bandwidth.

In practice, the inhomogeneous broadening can strongly be reduced but not completely removed. Typical bandwidths in Shpol'skii experiments carried out in *n*-alkane matrices at temperatures of 20k or lower are 1-3 cm^{-1}. That is sufficient to obtain vibrational resolved spectra, but in low-temperature single-molecule experiments, thousand-fold narrower transitions have been observed[3]. Homogeneous broadening factors affect each individual molecule to the same extent. In condensed-phase spectroscopy, it originates mostly from electron-phonon interactions. A phonon is a quantized lattice vibration of the matrix. During an electronic transition, one or several lattice vibrations can be simultaneously excited.

The homogeneous spectrum will therefore consist of a superposition of a narrow zero-phonon line (ZPL) and a broad phonon side band or phonon wing (PW) as shown in Figure 3. In emission the PW appears as a broad continuum at the low-energy side of the ZPL and in absorption at the high-energy side. In a low-temperature environment, this phonon sideband is often well distinguishable from the ZPL, as shown in Figure 3. For most applications one would like to obtain strong ZPLs, which means that the temperature should be as low as possible, and solute-matrix interactions should be weak. Both requirements are usually met when working under cryogenic conditions with non-polar compounds in an *n*-alkane matrix, but other solute-matrix combinations have also shown Shpol'skii-type spectral narrowing.[4, 5]

The intensity (I) may be described in the form:

$$I(\nu,T) = I_{ZPL}(\nu,T) + I_{PW}(\nu,T) \tag{1.6}$$

Where T is time and ν is frequency. The relative intensity of the ZPL can be characterized by the Debye-Waller factor α (T),

$$\alpha(T) = \frac{I_{ZPL}}{I_{ZPL} + I_{PW}} = \exp[-S(T)] \tag{1.7}$$

Where S, the so-called Huang-Rhys parameter, is a dimensionless quantity that indicates the strength of the electron-phonon coupling as a function of temperature.[4]

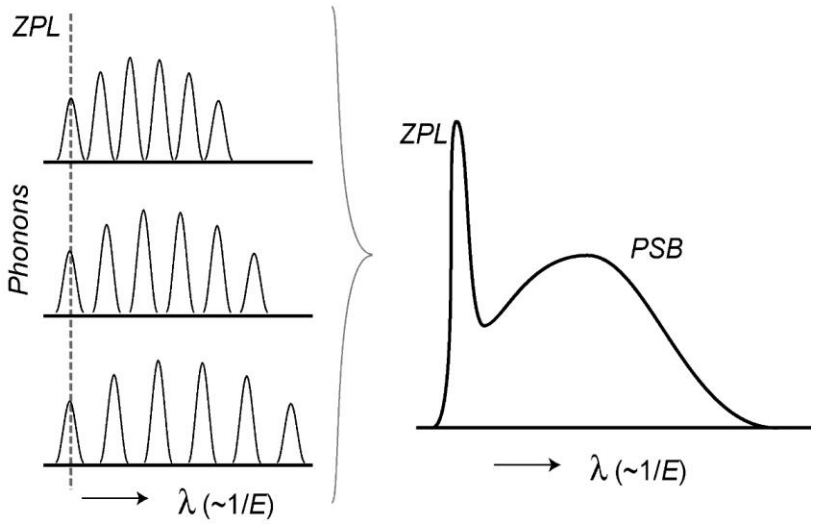

Figure 3. Electron phonon coupling in emission. On the left side three of the many possible phonons are shown, present in a number of overtones. The zero phonon transitions for all phonons coincide, resulting in a sharp zero-phonon line (ZPL). The phonons and their overtones do not overlap exactly and show up as a broad phonon side band (PSB), red-shifted in emission. In practice, excitation into a PSB results in additional broad red shifted emission from an inhomogeneous distribution of ZPLs.

Ultimately, the remaining source of homogeneous broadening is mainly determined by the lifetimes of the different states involved in the transitions. The shorter the lifetime, the less precise its energy and the broader the corresponding spectral lines will be. This so-called lifetime broadening is a quantum mechanical effect related to Heisenberg's uncertainty principle [6,] and it will be discussed later in this chapter.

In order to obtain a Shpol'skii spectrum the solvent should form a poly-crystalline matrix at low temperature.

In practice, mostly *n*-alkane solvents are used, but cycloalkanes are also possible. Finding the most appropriate solvent is not always evident and may involve some trial and error. For the analyte to fit into the poly-crystalline matrix, the three-dimensional shape, polarity, rigidity and the number of substituents of the fluorophore are very important. Ideally, the analyte molecule should displace a distinct number of solvent molecules in the lattice to only fit in a single, well-defined manner in the available space. In that case, all the analyte molecules will experience exactly the same interaction with the crystalline matrix, which means that the S_0-S_1 energy differences will be identical. However, sometimes there are two or several ways in which the molecule fits in the matrix; the molecule is said to occupy different sites (see Figure 4). For each site the S_0-S_1 energy difference is likely to be different. As a result, a multiplet will appear in the spectrum, both in absorption and emission and for every vibronic transition. In other words, two or more identical spectra will be observed, but shifted over a small amount of energy. The intensity ratio, which reflects the relative populations of each site, is constant for every multiplet. By using a tuneable laser, one of these subpopulations can selectively be excited in the 0-0 transition or in a vibration of the first excited state. Only this site will then appear in the emission spectrum.

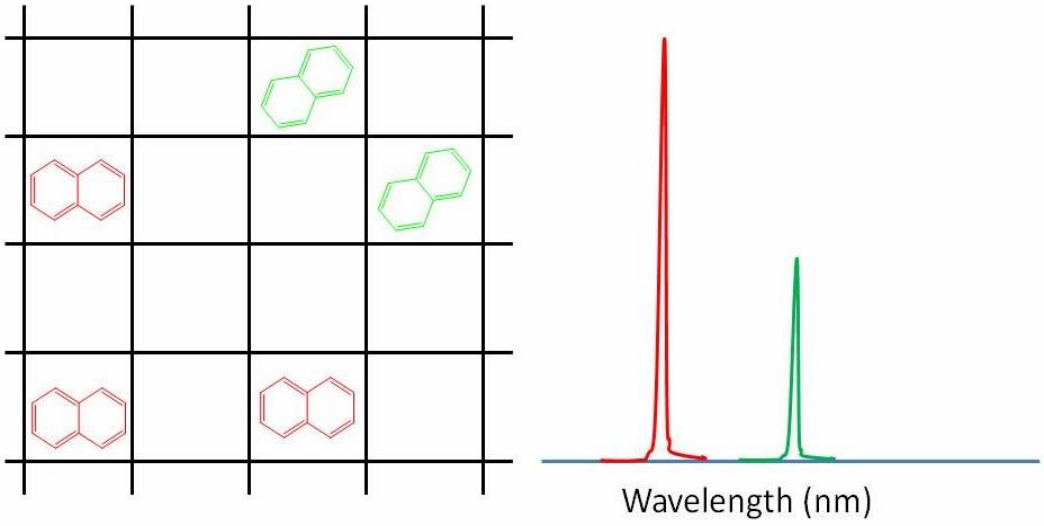

Figure 4. Cartoon showing the occurrence of different sites if the molecule fits in more than one way in the crystal. The relative line intensities in the spectrum reflect the respective populations.

A laser is not strictly needed to obtain high-resolution spectra in Shpol'skii spectroscopy. Literature reports show that high quality Shpol'skii spectra can be recorded with a standard spectrofluorimeter equipped with a broad-band, continuous wave xenon arc lamp.[8,9] The main pre-requisite in Shpol'skii spectroscopy is that the solvent forms a regular poly-crystalline matrix upon cooling. In the ideal situation, the analyte molecule displaces a distinct number of solvent molecules in the lattice and fits in a well-defined manner in the available space thus provided. Under excellent host-guest compatibility conditions, all solute molecules experience the same interactions with the environment and the broadening due to matrix inhomogeneity is reduced to about $1cm^{-1}$. As depicted in Figure 5, the resulting spectrum provides vibrational information for "fingerprint" compound identification.

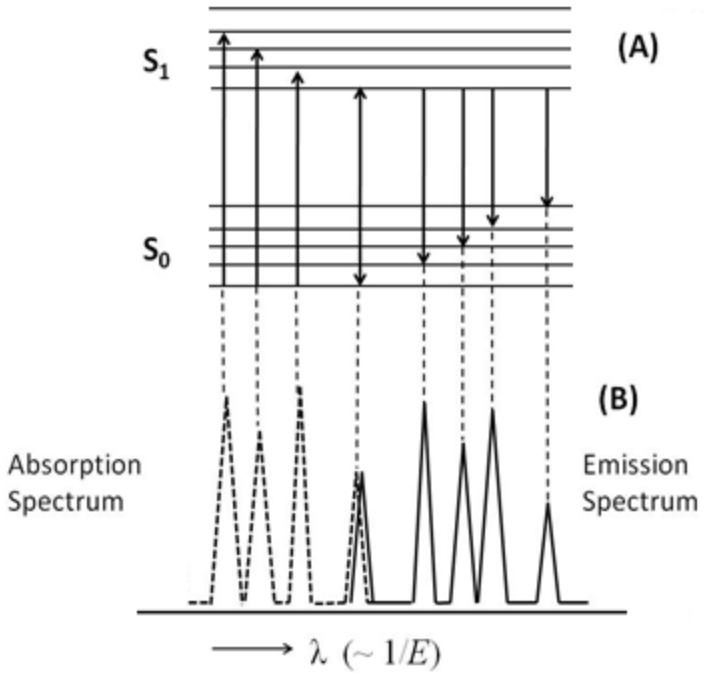

Figure 5. Jablonski diagram illustrating the concept of Shpol'skii spectroscopy (A) and the resulting spectrum (B). Only four vibrations are shown; in the absence of reorientation during the fluorescence lifetime.

Significant extra broadening can be observed if one of the states involved in excitation or emission has a lifetime shorter than approximately one picosecond. The origin of this so-called lifetime broadening is the time-energy uncertainty relationship, i.e. when the time of the transition can be determined accurately its energy cannot and vice versa. From the broadened spectral lines the lifetime can be calculated according to the following equation:

$$\tau = \frac{1}{2 \cdot \pi \cdot \Delta \nu \cdot c} \tag{1.8}$$

Where τ is the lifetime of the short-living state, Δυ the homogeneous broadening (in cm^{-1}) and c the speed of light (in cm/s).

Usually, in Shpol'skii spectroscopy these effects are only observed in excitation when higher electronic states (S2, S1 ...) are involved, since subsequent vibrational relaxation and/or internal conversion is fast. As a result, the bands observed in the excitation and/or absorption spectrum tend to be broader at shorter wavelengths.[7, 10] that is the main reason selective excitation is best accomplished within the S_1 band.

1.3. High Molecular Weight PAHs

Recent toxicological studies attribute a significant portion of the biological activity of PAHs contaminated samples to the presence of high molecular weight (HMW) PAH, i.e. PAHs with MW $\geq$ 300. The first group of HMW PAHs, i.e. the MW 300 and MW 302 isomers, has been identified in combustion related samples with high PAHs content such as coal tar,[11-14] carbon black,[15-17] and fuel combustion exhaust.[18-20] Their presence has also been confirmed in environmental samples such as air particulate matter,[13,14,21-24] mussels,[614] sediments[13,14,24-27] and soils.[26-28] Coronene is generally the only MW 300 isomer measured, even though a number of other isomers are possible.[18,29] Up to date, only a limited number of studies have reported the quantification of individual isomers.[12-14, 20] The majority of the reports have only been able to make a tentative identification of individual isomers or had to report concentrations in terms of a total fraction composed of several isomers. Because the carcinogenic properties of HMW PAHs differ significantly from isomer to isomer, it is of paramount importance to determine the most toxic isomers even if they are present at much lower concentrations than their less toxic isomers.

The need for unambiguous isomer identification is further intensified by recent findings showing that some HMW PAHs can exhibit far higher carcinogenic properties than EPA-PAHs. A crucial example is Dibenzo[*a*,*l*]pyrene (DB[*a*,*l*]P).

This compound is the most potent carcinogenic PAHs known to date[30-32]. Its carcinogenic potency is approximately 100 times higher than that of Benzo[*a*]pyrene (B[*a*]P). There are several more isomers of dibenzopyrene - including dibenzo[*a,e*]pyrene (DB[*a,e*]P), dibenzo[*a,h*]pyrene (DB[*a,h*]P), dibenzo[*a,i*]pyrene (DB[*a,i*]P) and dibenzo[*e,l*]pyrene (DB[*e,l*]P) (Figure 6) which are also carcinogenic, but not to the extent DB[*a,l*]P is. Thus, unambiguous identification of DB[*a,l*]P in environmental samples is highly relevant even if the other isomers are present at 10 to 100 times higher concentrations. Although DB[*a,l*]P is the most potent carcinogenic PAHs known to man, there are only limited data on its formation and presence in the environment. Early carcinogenicity studies mistakenly used the relatively weaker carcinogen dibenzo[*a,e*]fluoranthene.[33] As a matter of fact, only recently the U.S. Department of Health and Human Services listed DB[*a,l*]P, DB[*a,e*]P, DB[*a,h*]P and DB[*a,i*]P as potential carcinogens to humans.[34]

Unfortunately, EPA methodology cannot always meet the challenge of specifically analyzing structural isomers at the low concentration levels of environmental samples. The main problems that confront EPA methodology arise from the relatively low concentration levels and the large number of HMW PAHs isomers with very similar elution times and similar, possibly even identical, fragmentation patterns. An important component of our research, then, focuses on developing methods with the ability to efficiently and reliably detect the presence and determine the amounts of the most toxic HMW PAHs, even if their less toxic isomers are present in far higher concentrations.

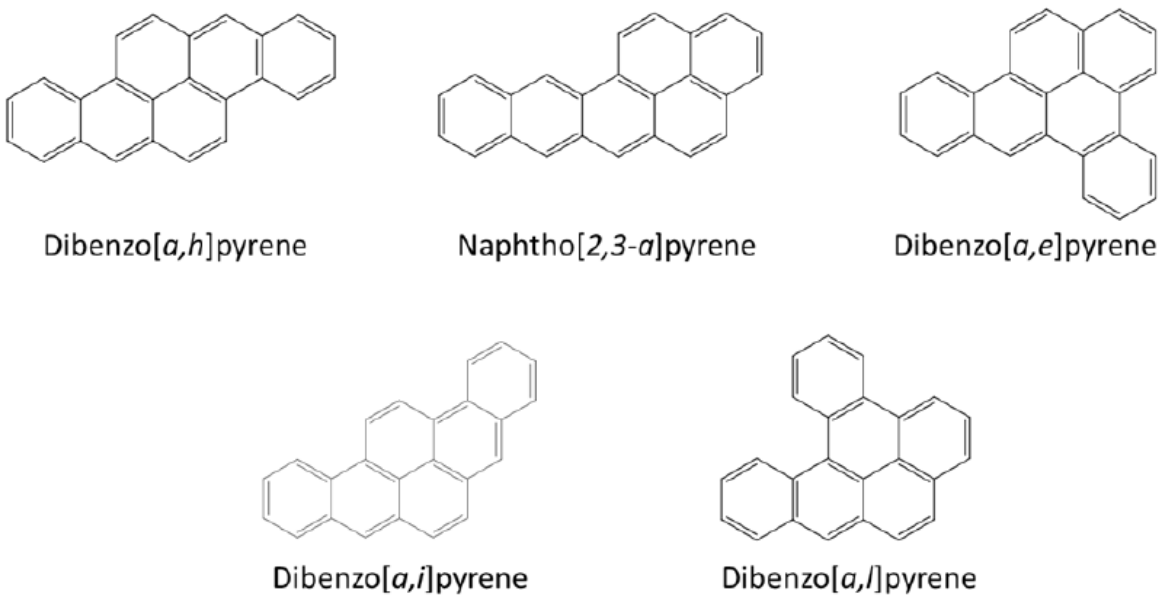

Figure 6. Molecular structure of 5 HMW-PAHs with MW 302.

1.4. Benzo[*a*]pyrene and Benzo[*a*]pyrene Metabolites

Parent PAHs are relatively inert and need metabolic activation to express their carcinogenicity. Covalent binding to DNA is believed to be the first critical step in the initiation of the tumour formation process.[36, 37] Complex heterogeneity makes the identification of the type(s) of chemical lesion(s) an extremely challenging problem. For instance, a given metabolite may bind to different bases or different nucleophilic centers of a base and exist in distinctly different adduct-DNA conformations.[38-41] Metabolism may also lead to a distribution of stereoisomeric metabolites and, as a consequence, stereo specific additions to DNA. The complexity of the problem is well illustrated in Figure 7. In the initial step of the metabolic activation of B[*a*]P, cytochrome P450s A1, 1A2, 1B1, 3A4, and 2C catalyze the formation of arene oxides and phenols [42-45].

The arene oxides may arrange spontaneously to phenols or undergo hydration catalyzed by epoxide hydrolase, leading to dihydrodiols. 7,8-Dihydro-7,8-dihydroxybenzo[*a*]pyrene is further oxidized to *anti*- and *syn*-7,8-dihydroxy-7,8,9,10-tetrahydrobenzo[*a*]pyrene (BPDE) in a reaction catalyzed by P450s 1A1, 1A2, and 1B1, as well as other enzymes.[46-48] Among the four BPDE enantiomers produced in these reactions, the (7R,8S,9S,10R)-enantiomer of anti-BPDE is generally formed to the greatest extent and shows the highest carcinogenic activity.[46-49] This diol epoxide reacts with DNA in vitro and in vivo, producing a major adduct in which the exocyclic amino group of deoxyguanosine undergoes *trans* addition to carbon 10 of BPDE. Convincing evidence clearly supports the hypothesis that the formation of this and related minor DNA adducts is the major metabolic activation pathway of B[*a*]P [46-51] . Other pathways of B[*a*]P metabolism lead predominantly to detoxification. These include phenol formation, glutathione conjugation of arene oxides and diol epoxides involving GSTM1, GSTA1, and GSTP1, and glucuronidation of dihydrodiols.

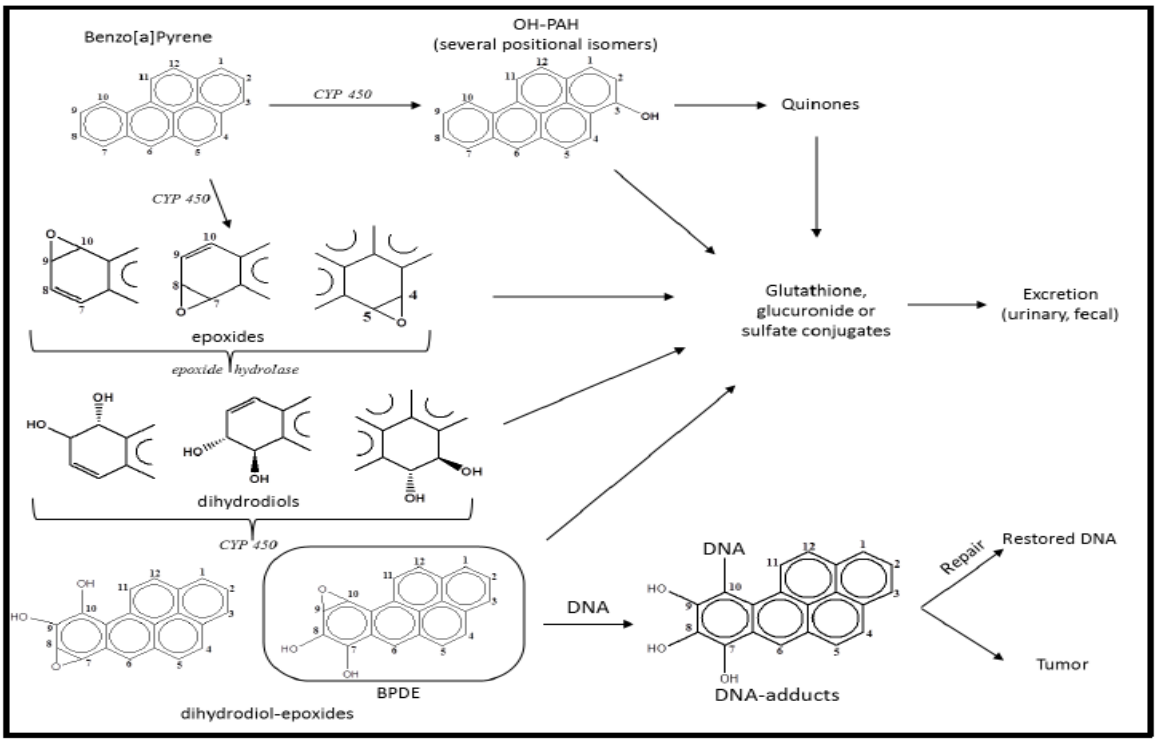

Figure 7. Overview of B[*a*]P metabolism. CYP: Cytochrome P450.[69]

By virtue of the rich heterogeneous distribution of metabolic products they produce, PAHs provide a full spectrum of the complexity associated with understanding the initial phase of carcinogenesis. During the past decades, tremendous efforts have been made to develop bio-analytical techniques that possess the selectivity and sensitivity for the problem at hand. The general scheme consists of metabolites separation and determination.[52-54] Separation of metabolites has been accomplished via HPLC, capillary electrophoresis (CE) and GC.

Ultraviolet –visible absorption and room temperature fluorescence detection have been widely used with both HPLC and CE.[60-65] The ultimate specificity belongs to high-resolution MS either coupled to gas chromatography (GC-MS) or HPLC (HPLC-MS).[52-54, 66-68].

Depending on the complexity of the sample and the relative concentrations of the targeted metabolites, a combination of preparation techniques is often necessary to reach the limits of detection of the instrumental method of analysis.[56-59] The numerous preparation steps open ample opportunity to metabolite loss and collection of inaccurate data. This dissertation presents an experimental approach based on solid-surface room temperature fluorescence spectroscopy. Octadecyl-silica membranes are employed with the dual purpose of metabolite extraction and solid substrates for spectroscopic measurements. The simplicity of the experimental procedure and the excellent analytical figures of merit demonstrate its potential for screening biomarkers of PAH exposure in numerous urine samples

CHAPTER 2. LASER EXCITED TIME-RESOLVED SHPOL'SKII SPECTROSCOPY

2.1. Introduction

Prior to our involvement with Shpol'skii spectroscopy, most of the applications towards the analysis of PAHs were based on the interpretation of fluorescence spectra [71, 72]. Although time-resolved spectroscopy had shown to reduce spectral overlapping [70], information on fluorescence lifetimes as qualitative parameters for PAHs identification was practically inexistent. The same was true for phosphorescence spectra and lifetimes.

One contribution we have made to this area is the introduction of methodology to efficiently collect multidimensional data formats during the lifetime decays of fluorescence (nanoseconds to microseconds) and phosphorescence (milliseconds to seconds) emission [73-75]. Our approach – which we have coined laser excited time-resolved Shpol'skii spectroscopy (LETRSS) - takes advantage of the full dimensionality of luminescence spectroscopy combining spectral and lifetime information in multidimensional formats known as wavelength time matrices (WTM). Adding the temporal dimension to the highly resolved Shpol'skii spectra provides an extremely selective tool for the determination of structural isomers in complex mixtures with numerous PAHs.

We developed an instrument to collect multidimensional data formats in both the fluorescence and phosphorescence time domains. Unambiguous isomer identification was made possible on the bases of spectral and lifetime analysis.

In addition to providing a qualitative parameter for PAHs identification, fluorescence and/or phosphorescence decays report on spectral peak purity, an essential condition for the accurate quantitative determination of PAHs without previous chromatographic separation. Another significant improvement we made was the introduction of cryogenic fiber optic probes for sample freezing at 77 K and 4.2 K. It is now possible to easily perform reproducible measurements at liquid nitrogen liquid helium temperatures in a matter of seconds.

2.2. Cryogenic Fiber Optic Probes

The classic sample preparation procedure for 77 K measurements consists of immersing a solution-filled small-diameter tube into an optical Dewar filled with liquid nitrogen. The fragility of the Dewar flask, bubbling in the cryogen at irregular intervals from small ice particles that act as nucleation sites, and condensation on the outside of the Dewar are nuisances. However, scattering at each of the interfaces encountered by the excitation light on its way to the sample is a much more severe problem, as stray light in the emission monochromator degrades the reproducibility of measurements and the LOD. The classic approach typically involves three air/glass interfaces, two liquid nitrogen/glass interfaces, and one matrix/glass interface. The number of scattering interfaces can be reduced with closed-cycle refrigerators or Joule-Thomson miniature refrigerators that employ contact cooling or cold vapor directed onto the sample cell. Trade-offs include higher cost, reduced sample throughput, and possibly less efficient or slower cooling of the sample. Depending on the cooling device and final temperature, and sample size and solvent, freezing times can take between 40 and 100 min per sample. The constancy of the freezing rate is a concern, because it can affect the population distribution in the various sites and the corresponding signal intensity for a given set of excitation and emission wavelengths.

Several attempts have been made to improve closed-cycle helium refrigerators. Ariese and co-workers [70] developed a user-friendly closed-cycle refrigerator that enables the simultaneous cooling of four 10µL samples placed in a gold-plated copper holder surrounded with sapphire windows. The high thermal conductivity of the sample holder material provides fast sample cooling for good quality Shpol'skii spectra.

We use fiber optic probes for cryogenic measurements at both 77 K and 4.2 K. Our probes are similar to the one reported by Hieftje and co-workers [76] for phosphorescence measurements at 77 K. Hieftje's probe consisted of one excitation and six emission fibers bundled in a quartz tube with the opposite end connected to a plastic sample vial. Sample excitation and emission collection was made through a quartz window placed between the quartz tube and the sample vial. Our probes retain the simplicity of "dunking" the sample into the liquid cryogen for fast and reproducible freezing, but eliminate all interfaces that could scatter excitation light into the detection system. Figure 8A shows an example of a probe for cryogenic measurements at 4.2 K. At the sample end, the fibers are epoxied in a six-around-one configuration with the delivery fiber in the center. At the collection end, the excitation and collection fibers are separated and vertically aligned with the spectrograph entrance slit. After the sample is introduced into the sample tube, the tip of the probe is positioned above the solution surface as the sample tube is lowered into a container filled with liquid cryogen. The cell is allowed to cool for 90 s prior to luminescence measurements to ensure complete sample freezing. Because there is no physical contact between the fiber and the sample, fiber clean up between samples is not necessary. Preparing frozen samples for luminescence measurements at 77 K and 4.2 K is now a routine technique. Samples are frozen in a matter of seconds.

2.3. Instrumentation for Multidimensional Luminescence Spectroscopy

Pulsed excitation sources offer prospects for time-resolving the emission to improve signal-to-background ratios and reduce spectral interference. Early reports on laser excited Shpol'skii spectrometry implemented time resolution at fixed delay time intervals by using laboratory-constructed gated integrators or commercial boxcar averagers [77-81]. Later, advantage was taken of commercially available delay generators and intensified linear photodiode arrays. Multi-channel detectors can acquire emission spectra at good signal-to-noise ratios much faster than is possible with scanning monochromators. Collecting the entire emission spectrum at once avoids problems associated with pulse-to-pulse fluctuation, laser intensity drift, and photodecomposition that could degrade analytical figures of merit.

Our group has shown that the combination of a pulsed tunable dye laser, a pulsed delay generator, a spectrograph, and an intensifier-charged coupled device (ICCD) is well suited for the rapid collection of WTMs, excitation-emission matrices (EEMs) and time resolved EEMs (TREEMs) in both the fluorescence and the phosphorescence time domains. Figure 8B shows a schematic diagram of the instrumental set-up mounted in our lab. As an excitation source, we have used a compact frequency doubled pulsed tunable dye laser whose bandwidth (< 0.03 nm) is well matched for selective excitation of narrow Shpol'skii excitation spectra. The ICCD is coupled to a spectrograph to rapidly collect a series of emission spectra at different delay times between the laser firing and the opening of the gate on the ICCD. The integration of the mechanical shutter in the path of the dye laser excitation beam facilitates the collection of multidimensional data in the phosphorescence time domain.

The shutter has a rise time (open time) of 1.5 ms and a fall time (close time) of 3.0 ms with a maximum pulse width of 6.5 ms. The shutter is controlled either manually (always open or always closed) via a switch on the controller front panel or programmatically through a transistor-transient logic (TTL) pulse. This TTL pulse is programmed through the A + B outputs of the digital delay generator via a general purpose interface bus (GPIB) interface.

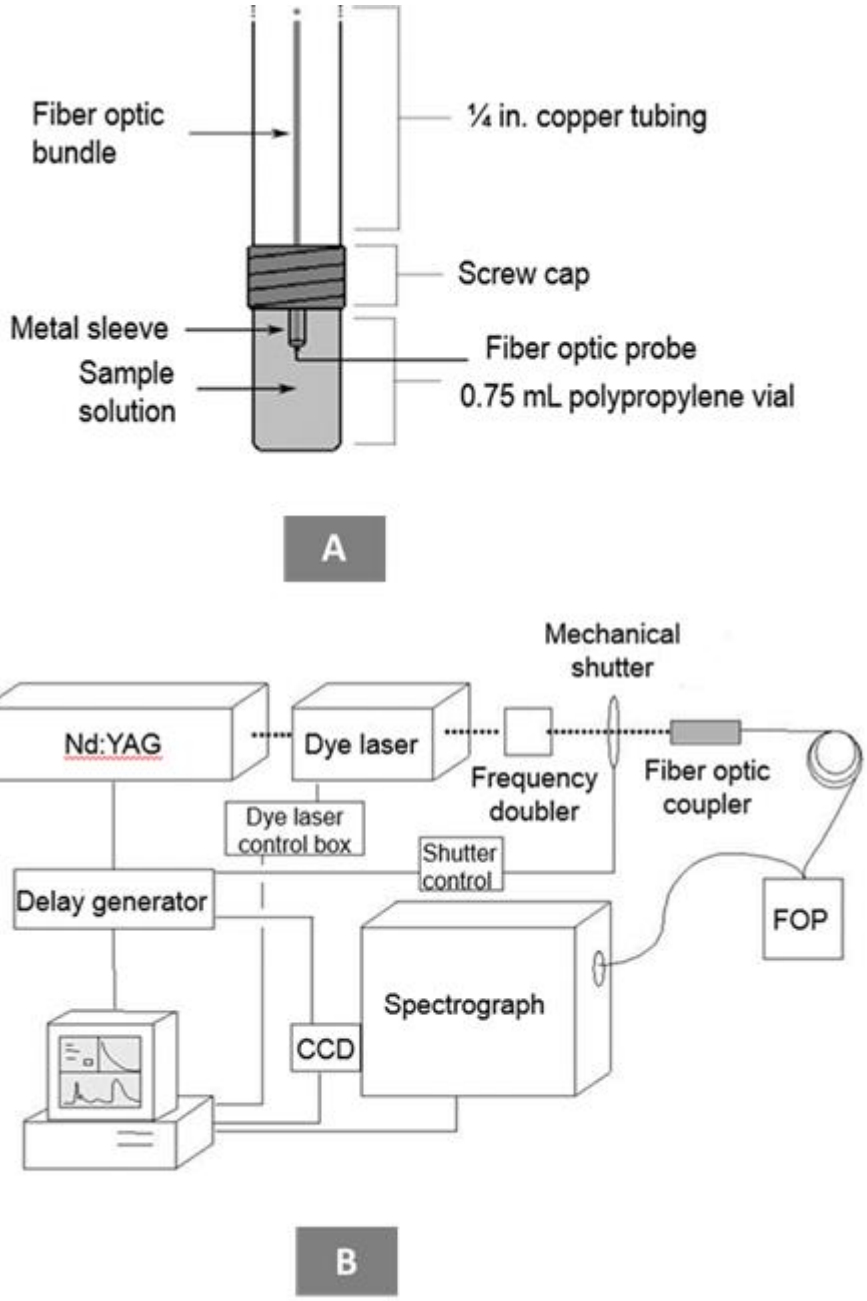

Figure 8. Instrumental system and fiber optic probe for 4.2 K laser-induced fluorescence spectrometry with single channel and multi-channel fluorescence detection.

Fluorescence measurements are made with the mechanical shutter in the open position. Time resolution is achieved with the intensifier in front of the ICCD, which acts as a superfast shutter with a minimum gate of 2 ns (full width at half-maximum). Once triggered by the laser, the pulse delay generator uses this information to determine when the image intensifier in the detector head is gated on (gate delay, *D*) and for how long it is gated on (gate width, *G*). These parameters are entered on the control computer with commercial software. The ICCD acquires data while the intensifier is gated on. While the intensifier is gated off, the acquired data are transferred from the detector head to the controller card (32-bit Intelligent Bus-Mastering PCI card) in the computer. Typically, fluorescence spectra from PAHs result from the accumulation of emission of 100 laser pulses. This process takes approximately 10 ms/40 nm spectrum. If a wavelength range larger than 40 nm is of interest, the spectrograph is tuned to the new wavelength range and the process is repeated.

Previous reports on WTM collection utilized a rather tedious and time consuming procedure, in which the wavelength of either the laser source or the emission monochromator was incremented while the luminescence intensity-luminescence decay waveform was collected at each wavelength. By setting the ICCD gate step parameter, our system automatically increments the time interval between successive fluorescence scans so that a WTM is easily built up. The duration of the steps by which the gate delay is progressively increased in the course of the sequence of acquisitions is entered on the control computer with commercial software.

Fluorescence lifetimes are recorded via a three-step procedure: (1) full sample and background WTM collection; (2) Background decay curve subtraction from the fluorescence or phosphorescence decay curve at a wavelength of maximum emission for each PAH; and (3) fitting of the background corrected data to single-exponential decays. Commercial software is used for curve fitting of fluorescence and phosphorescence lifetimes. Fitted decay curves $y = y_0 + A_1 e^{[-(x-x_0))t_1]}$ are obtained by fixing x_0 and y_0 at a value of zero.

2.4. Multidimensional Data Formats from Single-Site and Multi-Site PAH/N-Alkane Systems

The experimental value (0.09 nm) of the full width at half maximum for a mercury (Hg) line (313 nm) emitted from a Hg lamp placed at the analysis end of the fiber optic probe is within the theoretical value calculated from the spectral range of an individual pixel in the CCD array. Based on the reciprocal linear dispersion (R_L = 0.8 nm/mm) of the spectrograph, the number of active pixels (690 x 256) in the array, and the dimensions (18 x 6.7 mm) of the active area of the CCD chip, the spectral range of one pixel should give a 0.02 nm limiting resolution. Because of the detector crosstalk and the intensifier, the factual limiting resolution corresponds to 4-5 pixels (5), i.e. 0.08 - 0.10 nm. This resolution is sufficient to collect accurate spectra from both single-site and multiple-site PAH/n-alkane systems. Figure 9 shows an example of a single-site (naphthalene in n-pentane) multiple-site system, i.e. benzo[*a*]pyrene in n-octane. Upon fast cooling in n-heptane, benzo[*a*]pyrene occupies four crystallographic sites that yield four distinct fluorescence spectra slightly shifted by small wavelength differences.

The maximum wavelengths of the quartet emissions from the 0-0 transitions appear at 402.3, 402.7, 403.1 and 403.8 nm. The maximum wavelengths and the relative intensities of the fluorescence peaks correlate well to those previously reported with conventional methodology [70-72].

Figure 10 shows two WTMs recorded with the fiber optic probe at 77 K along with their respective I_f vs. t_d plots.

The gate delay (t_d) was advanced in 20 ns increments for pyrene and 5 ns increments for dibenz[*a,h*]anthracene. The fluorescence spectrum at each gate delay t_d was averaged over 100 laser pulses. Table 1 summarizes the lifetimes of the 6 PAHs obtained by this procedure. In all cases, single exponential decays were observed. The agreement between the calculated and observed points over the first two lifetimes of the decay is within about 1% and the residuals show no systematic trends. Background emissions from n-alkanes have relatively short lifetimes (~ 5 ns). With long-lived compounds, such as benzo[*g,h,i*]perylene (183 ns) and pyrene (527 ns), the collection of strong PAH fluorescence can start at relatively long delay times ($t_d > 30$ ns), in which case the main contribution to the background is instrumental noise. For PAHs with shorter fluorescence lifetimes, such as dibenz[*a,h*]anthracene (41 ns), complete time-resolution of fluorescence background is not possible, but the t_d and gate time (t_g) values can be selected to collect most of the fluorescence emitted by the PAH.

Interesting to note are the significant lifetimes differences we have observed from PAHs molecules occupying different crystallographic sites in the same matrix. Some examples are summarized in Table 1.

No other reports exist on this phenomenon but our observations are consistent with the well-known sensitivity of fluorescence lifetimes to the microenvironment of the fluorophore. It is generally accepted that the multiplet structure of fluorescence spectra arise from the different orientations of the PAH molecule in the solid matrix. The different orientations lead to non-equivalent crystal field effects and hence wavelength shifts [89, 90]. Most likely, the field effects are also sensed by the PAH fluorescence lifetime. The lifetime differences from site to site are usually larger than their wavelength shifts.

This fact helped us to identify the two crystallographic sites of benzo[a]pyrene in n-octane, which had been previously reported as a single site system. Although we have not unfolded the analytical potential of site selective lifetime analysis yet, the rather large lifetime differences anticipate a promising contribution to enhancing the specificity of site-selective excitation. As we will later show in this review, the specificity of lifetime measurements plays an important role in the analysis of closely related structural isomers.

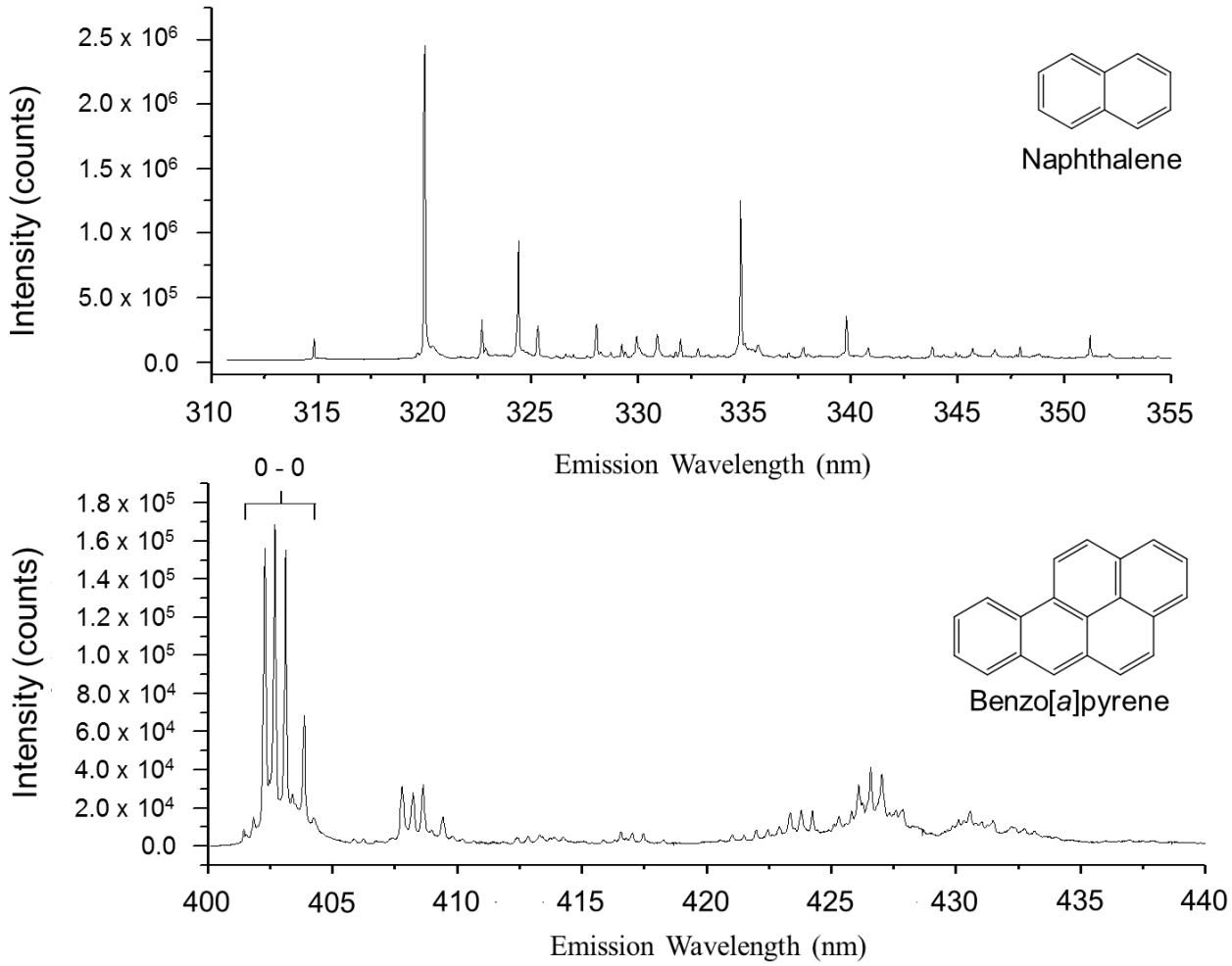

Figure 9. 4.2 K fluorescence spectrum of 10 µg mL^{-1} naphthalene in n-pentane (top) and 0.2 µg mL^{-1} benzo[a]pyrene in n-heptane (bottom) recorded with the fiber-optic probe, spectrograph, and ICCD camera. The naphthalene spectrum was recorded with an excitation wavelength of 306.0 nm, spectrograph entrance slit of 42 µm, delay of 10 ns and a gate of 1000 ns. The benzo[*a*]pyrene spectrum was recorded with an excitation wavelength of 366.0 nm, spectrograph entrance slit of 25 µm, delay of 20 ns and a gate of 200 ns. Both spectra correspond to the accumulation of 100 laser shots.

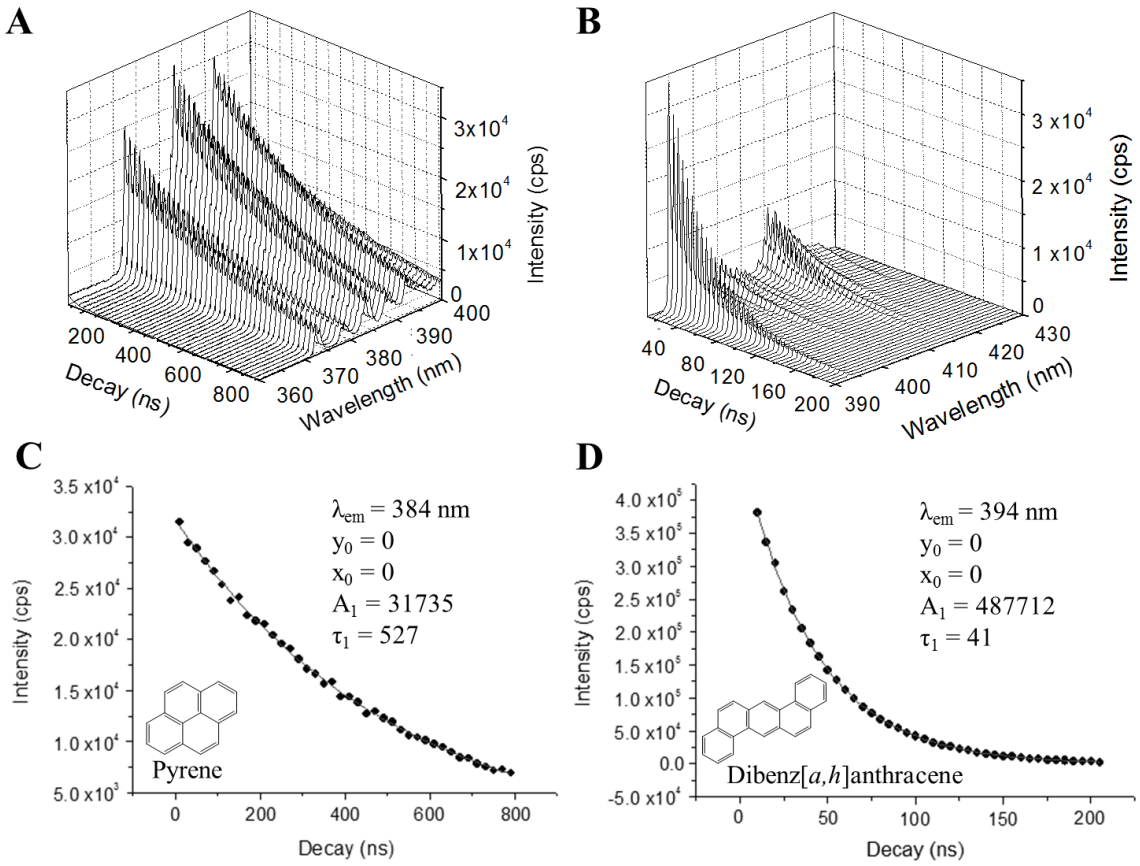

Figure 10. 77 K WTMs recorded from 1 µg mL^{-1} standards of (A) pyrene and (B) dibenz[*a*,*h*]anthracene in n-hexane. The following acquisition parameters were used for spectra collection: (A) λ_{exc} = 280 nm, t_d = 10 ns, t_g = 200 ns and gate step = 20 ns; (B) λ_{exc} = 290 nm, t_d = 10 ns, t_g = 200 ns and gate step = 5 ns. Each fluorescence spectrum in the WTMs corresponds to the accumulation of 100 laser pulses. Entrance slit of spectrograph was 100 µm. Fluorescence decays of pyrene (C) and dibenz[*a*,*h*]anthracene (D) built with fluorescence intensities stripped from the WTMs at the maximum wavelengths of emission.

Table 1 Fluorescence lifetimes (τ) of PAHs molecules occupying different crystallographic sites in the frozen matrix

	n-hexane		n-heptane		n-octane	
PAH[a]	λ_{em}[b] (nm)	τ (ns)	λ_{em}[b] (nm)	τ (ns)	λ_{em}[b] (nm)	τ (ns)
Benzo[*a*]pyrene	403.56	27.02 ± 0.50	402.31	52.09 ± 0.93	403.10	36.04 ± 0.61
	403.94	43.44 ± 1.00	402.72	46.93 ± 0.49	403.20	45.68 ± 0.84
	404.53	31.95 ± 0.89	403.15	42.77 ± 0.89		
			403.89	41.29 ± 1.18		
Pyrene	376.63	503.98 ± 6.01	--------[c]	--------[c]	--------[c]	--------[c]
	372.45	577.43 ± 3.47				
Benzo[*a*]anthracene	383.34	53.63 ± 0.50	--------[c]	--------[c]	--------[c]	--------[c]
	383.94	56.43 ± 0.76				

[a] PAHs solutions were prepared at 0.5 μg mL^{-1}.

[b] Wavelength of maximum fluorescence emission. All data obtained using λ_{exc} = 288.50.

[c] Spectra and decay data were not measured for this PAH/solvent system.

Recording two-dimensional (2-D) fluorescence spectra – i.e. plots correlating fluorescence intensities to emission wavelengths - from a mixture with numerous fluorescence components only provides partial information on the total fluorescence of the sample. The emission profile of a mixture with numerous fluorescence components varies with the relative position of the excitation wavelength to the excitation maxima of the fluorophores in the mixture. Individual fluorophore contributions to the total fluorescence spectrum of the sample also depend on the fluorescence quantum yields of the fluorophores and possible quenching due to synergistic effects. EEM gather all this information in a single data format to provide a true signature of the total fluorescence of a multi-fluorophore mixture.

Most of the work on low-temperature EEM has been performed with high-resolution spectrometers that built up fluorescence EEM with numerous repetitive scans [70]. The main drawbacks of this approach are the long EEM acquisition times, the need for relatively large excitation and emission bandwidths and the inability to record phosphorescence EEM. The large bandwidths, which are imposed by the low throughput of the high-resolution spectrometers, limit the spectral resolution of the EEM and the selectivity of analysis.

Our system is well suited for rapid collection of low-temperature fluorescence and phosphorescence EEM. Because of the spectrograph and the ICCD, both formats are collected in short analysis time. The tunable dye laser provides intense excitation energy in a narrow excitation bandwidth. Its scanning capability is essential to take full advantage of the specificity obtainable from the highly resolved PAH excitation spectra in Shpol'skii matrixes. Its intense excitation energy promotes strong PAH fluorescence to recording spectra with optimum spectrograph slits for maximum spectral resolution.

Figure 11 displays the 4.2 K fluorescence and phosphorescence EEM of chrysene in n-octane. The dye laser was automatically tuned in 0.1 nm steps between 310 and 335 nm. Collecting the entire fluorescence and phosphorescence data sets took no longer than 5 and 8 min, respectively. Both EEM show similar features shifted from each other with regards to emission wavelengths. This pattern is often an indication that multiple sites are present in the frozen matrix. Our lifetime measurements (see Table 1) confirm this multiple structure of fluorescence and phosphorescence emission.

In comparison to EEM, chemical analysis based on TREEM is potentially more selective because it adds the temporal dimension to the orthogonal spectral dimension of EEM. TREEM are basically a series of fluorescence WTM acquired at different excitation wavelengths.

The complete data set consists of fluorescence intensity as a function of excitation wavelength, emission wavelength, and delay time after the short duration of pulse excitation. All the intensity values (as a function of excitation and emission wavelengths) for a particular decay time can be assembled into an EEM format specific for that decay time.

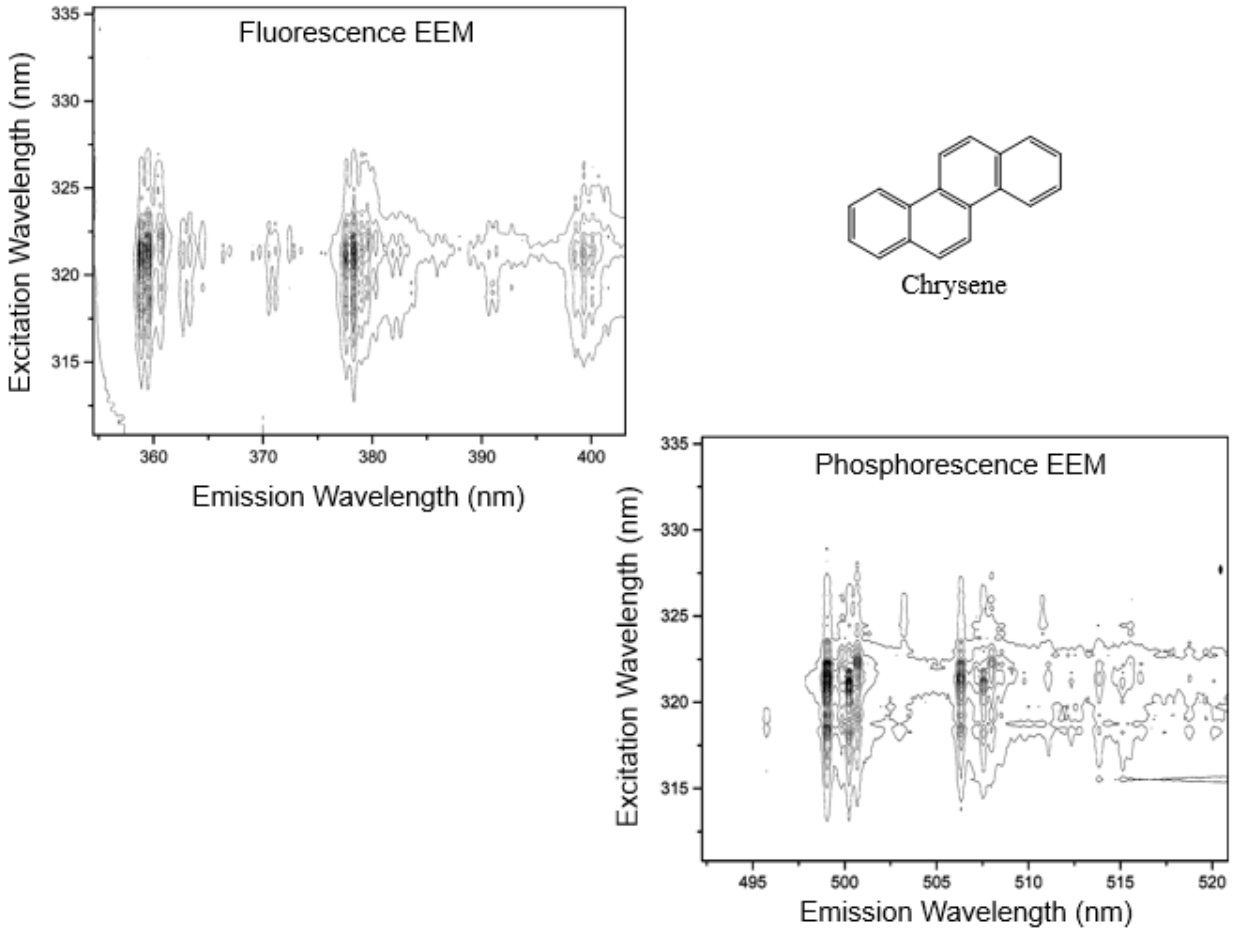

Figure 11. 4.2 K fluorescence and phosphorescence EEM recorded from a 0.2 μg mL^{-1} chrysene solution in n-octane. The fluorescence EEM was recorded using a 20 ns delay and a 200 ns gate time. The phosphorescence EEM was collected using 10 μs delay and 40 ms gate times. The excitation wavelength step was 0.1 nm.

The potential of TREEM is here illustrated with the direct determination of DB[*a,l*]P in a heavily contaminated water sample from the American Petroleum Institute (API). API water is used to desalt and scrub crude oil and oil fractions in the refinery process and shows a visible surface petroleum layer at the separator trough. Previous HPLC analysis of this water has shown heavy contamination with fluorescent pollutants, including several EPA-PAHs. The complexity of this sample is illustrated in Figure 12 with the UV-VIS chromatogram of the sample extract and the 4.2 K EEMs collected within the wavelength ranges of DB[*a,l*]P. At the top EEM, the delay (10 ns) and the gate (1000 ns) were selected to collect a substantial portion of the total fluorescence of the sample. The low-intensity features throughout most of the EEM indicate extensive fluorescence background from several concomitants in the sample. The bottom EEM was collected after spiking the API water with DB[*a,l*]P at the 0.5 ng mL^{-1} concentration level. Because the delay (10 ns) and the gate (250 ns) were optimized to enhance the spectral features of DB[*a,l*]P, the fluorescence background disappears and the presence of DB[*a,l*]P is clearly noted.

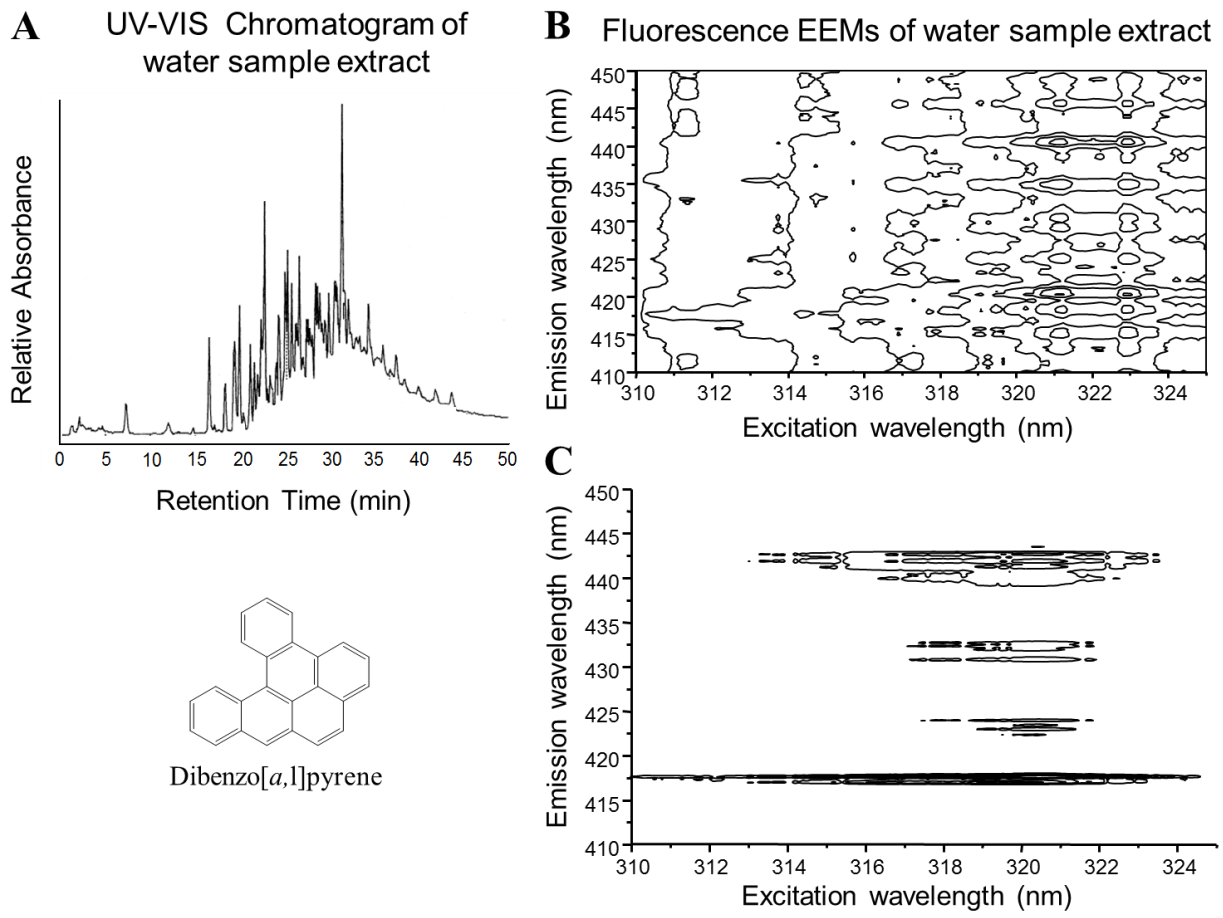

Figure 12. (A) Chromatogram of API water extract using Supelcosil LC-PAH column. (B) 4.2 K EEM of API water recorded from an extraction membrane spiked with 100 µL of n-octane. Delay and gate times were 10 and 1000 ns, respectively. (C) 4.2 K EEM of API water spiked with 5 ng mL^{-1} DB[*a,l*]P prior to SPE. EEM was recorded from an extraction membrane spiked with 100 µL of n-octane. Delay and gate times were 10 and 150 ns, respectively. In both cases, spectra were accumulated over 100 laser shots at each excitation wavelength using increments of 0.2 nm. Spectrograph slits were 42 µm.

2.5. LLE-LETRSS and SPE-LETRSS

The use of cryogenic fiber optic probes facilitates the hyphenation of LETRSS to sample pre-concentration techniques for the analysis of aqueous samples. LLE-LETRSS and SPE-LETRSS methods have been developed in our lab for the determination of polycyclic aromatic compounds in HPLC fractions and sample extracts [83-88]. Figure 13A shows the main steps of the experimental procedure for LLE-LETRSS. Millilitre volumes of aqueous sample are mixed with micro-litters of Shpol'skii solvent (n-alkane) in the vessel of the fiber optic probe. After shaking the vessel for 1-2 min, the mixture is allowed to stand for ~ 1 min to separate the two liquid layers.

The sample vial is then attached to the optical probe and the fiber assembly is lowered into the liquid cryogen for LETRSS measurements. Quantitative analysis is based on the linear relationship that exists between analyte concentration in the Shpol'skii layer (C_{SS}) and its concentration in the aqueous sample (C_{AS}):

$$C_{AS} = (1/K_d) \times (V_{SS}/V_{AS}) \times C_{SS} \quad (2.1)$$

Where K_d is the partition coefficient of the analyte between the Shpol'skii solvent and the aqueous sample ($K_d = C_{SS}/C_{AS}$), and V_{SS} and V_{AS} are the volumes of Shpol'skii solvent and aqueous sample, respectively.

Two different procedures have been developed for SPE-LETRSS analysis. Figure 13B depicts the main steps of the eluting method. A 13 mm octadecyl (C-18) membrane is placed into a 100 mL extraction syringe. Positive pressure is used to force all liquid solutions through the disk. Prior to sample extraction, the C-18 membrane is conditioned with 1 mL of methanol.

Following water extraction, void water is mechanically removed by forcing three 100 mL volumes of air through the disk.

PAHs are eluted from the extraction membrane using an appropriate volume of Shpol'skii solvent. The quantitative correlation between the PAHs concentration in the aqueous sample and the layer of Shpol'skii solvent is given by the following equation:

$$C_{AS} = [f_2/f_1] \times [V_{SS}/V_{AS}] \times C_{SS} \quad (2.2)$$

Where f_1 and f_2 are the fractions of extracted and eluted PAHs, respectively. For a 10 mL sample volume (V_{AS} = 10 mL) and 5 mL of eluting solvent (V_{SS} = 5 mL), the best sample pre-concentration factor ($[f_2/f_1] \times [V_{SS}/V_{AS}]$) that one could obtain would be 2, i.e. when $f_1$and f_2 are both equal to 1. Table 2 summarizes f_1 and f_2 values of several EPA-PAHs. The amounts of extracted PAHs are statistically equivalent to 100% (P = 0.05; N = 6), i.e. $f_1 = 1$. The same is not true for the f_2 values of some PAHs. Two factors are known to deteriorate PAHs recovery from extraction membranes: (a) non-reversed-phase interactions (hydrogen bonding and dipole-dipole interactions) between the PAH and the unreacted (residual) silanol and siloxane groups on the surface of octadecyl silica phases; and (b) the presence of trapped and sorbed water in the silica particles. The strength of hydrogen bonding and dipole-dipole interactions varies with the physico-chemical properties of the PAH, which might explain some of the variations in recoveries. The air-drying procedure prior to PAH elution removes the majority of the water in the void volume. The water in the smallest pores (trapped water) and water sorbed to the silica surface remains on the membrane. This water possibly blocks the interaction between n-alkane and the PAH, deteriorating the extraction efficiency of the non-polar solvent.

Table 2 Solid-Phase Extraction of EPA-PAHs

PAH	f_1 [a]	f_2 [b]
Naphthalene	0.994 ± 0.003	0.578 ± 0.035
Acenaphthene	0.999 ± 0.016	0.551 ± 0.016
Fluorene	0.988 ± 0.023	0.534 ± 0.039
Phenanthrene	0.997 ± 0.030	0.571 ± 0.064
Anthracene	0.999 ± 0.005	0.103 ± 0.033
Fluoranthene	0.999 ± 0.020	0.937 ± 0.061
Pyrene	0.999 ± 0.019	0.992 ± 0.022
Benzo[*a*]anthracene	0.998 ± 0.021	0.969 ± 0.014
Chrysene	0.997 ± 0.018	0.105 ± 0.065
Benzo[*b*]fluoranthene	0.994 ± 0.034	0.883 ± 0.056
Benzo[*k*]fluoranthene	0.954 ± 0.063	0.977 ± 0.035
Benzo[*a*]pyrene	0.949 ± 0.083	0.574 ± 0.076
Dibenz[*a,h*]anthracene	0.723 ± 0.040	0.104 ± 0.048
Benzo[*g,h,i*]perylene	0.959 ± 0.082	0.588 ± 0.026
Indeno[*1,2,3-cd*]pyrene	0.929 ± 0.038	0.889 ± 0.018

[a] Based upon fluorescence of PAH solution before and after extraction.
[b] Determined by standard additions on eluent.

Better pre-concentration factors are obtained with the spiking method. The main steps of the spiking procedure are shown in Figure 13C. The 5.5 mm diameter allows for the membrane to fit into the vessel of the fiber optic probe (~ 6 mm inner diameter). Quantitative analysis obeys the following equation:

$$C_{AS} = (V_{SS}/f_1V_{AS} + KV_M/f_1V_{AS}) \times C_{SS} \quad (2.3)$$

where K is the distribution ratio between the analyte concentration on the membrane (C_M) and in the Shpol'skii solvent – i.e., $K = C_M/C_{SS}$ - and V_M is the volume of the extraction membrane, i.e. 23.8 µL. V_M is calculated using the standard formula for the volume of a cylinder $V = \pi r^2 h$, where r is the radius of the membrane (2.75 mm) and h is its thickness (~ 1 mm).

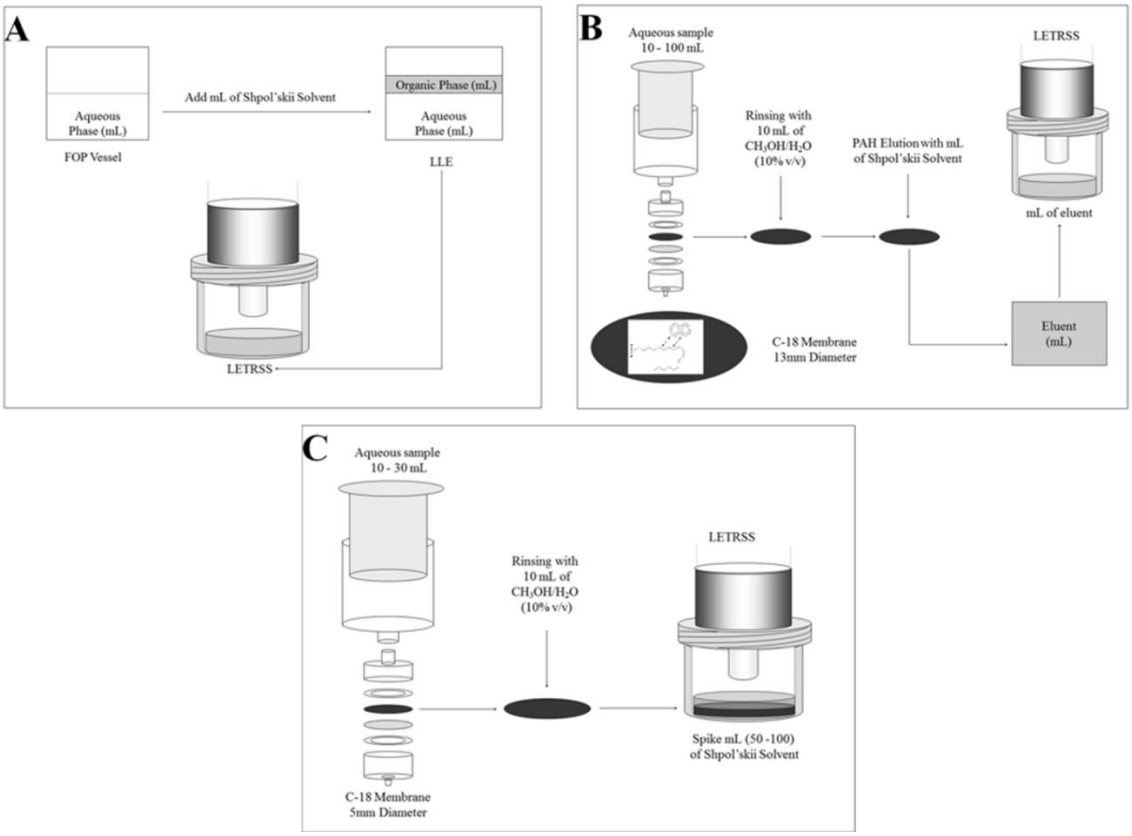

Figure 13. Schematic diagram of the experimental procedures for (A) LLE-LETRSS, (B) eluting SPE-LETRSS and (C) spiked SPE-LETRSS for the analysis of aqueous samples.

For phenanthrene (K = 3.3 ± 0.41), chrysene (K = 10.80 ± 2.50) and fluorene (K = 8.0 ± 1.4), 10 mL of water sample (V_{AS} = 10 mL; f_1= 1) and 100 µL of n-hexane (V_{SS} = 100 mL), equation (3) predicts pre-concentration factors ranging from ~ 34 (fluorene) to ~ 79 (chrysene).

The spiking method is particularly useful for the analysis of polychlorinated biphenyls (PCBs) and polychlorinated dibenzofurans (PCDBFs). PCBs and PCDBFs show strong phosphorescence emission in Shpol'skii matrixes at both 77 K and 4.2 K. Many cases exist where the amount of eluted PCB or PCDBF behaves randomly and makes SPE unsuited for analytical use. In other cases, the low amount of eluted PCB or PCDBF provides poor analyte recoveries. In our lab, the worst-case scenario was observed with 4-chlorobiphenyl, which had a zero recovery from the extraction membrane. Table 3 summaries the K values for biphenyl, dibenzofuran, three PCBs and three PCDBFs obtained with 100 µl of n-heptane. The tabulated values were obtained from the slopes of the C_{SS} vs. C_M plots. The standard deviations of the slopes were calculated via the bivariate least-squares regression method, which takes into account the uncertainties in both axes of the C_{SS} vs. C_M plots [91, 93]. The variances close to unity show the linear relationships between C_{SS} and C_M and the constant slopes demonstrate that K remains the same within the studied concentration range. The K values demonstrate the highest affinity of 4-chlorobiphenyl for the extraction membrane, which correlates well to the zero percent recovery of the eluting procedure. It is also interesting to note that the distribution ratio of biphenyl (K = 9.78) is lower than the K values of the three PCBs. The same is true for dibenzofuran (K = 4.08) and the three PCDBFs. The higher affinity of the chlorinated pollutants for the membrane can be attributed to non-reversed-phase interactions (hydrogen bonding and dipole–dipole interactions) with the unreacted (residual) silanol and siloxane groups on the surface of octadecyl silica phases.

Although hydrogen bonding and dipole–dipole interactions might also occur with biphenyl and dibenzofuran, the presence of chlorine atoms possibly enhances their effect.

Table 3 Distribution ratios of organic pollutants between SPE membrane and Shpol'skii solvent

Analyte	K[a]	S[b]
Dibenzofuran	4.08	0.45
Biphenyl	9.78	0.88
2-Chlorodibenzofuran	7.34	0.55
2,8-Dichlorodibenzofuran	24.75	3.16
2,3,7,8Tetrachlorodibenzofuran	9.33	0.10
4-chlorobiphenyl	133.84	16.32
3,3',4,4'-Tetrachlorobiphenyl	13.42	2.21
2,3',4,4',5-Pentaclorobiphenyl	24.58	3.11

[a] K, distribution ratio defined as $K = C_M/C_{SS}$. Where C_M is the analyte concentration in the SPE membrane and C_{SS} is the analyte concentration in the organic solvent.

[b] S = standard deviation of the slope (K). K and S were obtained from linear regression plots.[91]

Despite the rather large K values, the analysis of PCBs and PCDBFs with the spiking procedure is still possible. Table 4 summaries the analytical figures of merit (AFOMs) obtained with 10 mL of water and 100 μL of n-heptane. The correlation coefficients (R) of the calibration curves are close to unity, the linear dynamic ranges (LDR) extend over two orders of magnitude and the limits of detection (LODs) are at the parts-per-billion level. The relative standard deviations (RSD) measured at medium concentrations within the LDR are lower than 10%, which is excellent for fluorescence measurements. It is important to note that the RSD represent the precision of the method and include the random errors propagated from water extraction to signal measurements. It is also important to note that the spiking method makes the analysis of 4-chlorobiphenyl feasible.

Table 4 4.2 K LETRSS analytical figures of merit of PCBs and PDBFs on SPE spiked with Shpol'skii solvent

Analyte[a]	$\lambda_{exc}/\lambda_{em}$[b] (nm)	R^2[c]	LDR[d] (ng mL^{-1})	LOD[e] (ng mL^{-1})	RSD[f] (%)
2-Chlorodibenzofuran	284/440	0.9984	0.27-150	0.27	9.1
2,8-Dichlorodibenzofuran	284/434	0.9998	0.85-200	0.85	8.4
2,3,7,8-Tetrachlorodibenzofuran	284/440	0.9987	0.76-200	0.76	7.7
4-chlorobiphenyl	284/482	0.9996	12.8-2000	7.7	7.2
3,3',4,4'-Tetrachlorobiphenyl	284/494	0.9996	5.3-1000	5.3	8.8
2,3',4,4',5-Pentaclorobiphenyl	284/491	0.9998	5.5-2000	5.5	6.4

[a] Analytical figures of merit were obtained with 10 mL of aqueous standard solution. 100 µL of n-heptane as Shpol'skii solvent were used to spike the SPE membrane.

[b] Excitation (λ_{exc}) and phosphorescence (λ_{em}) wavelengths.

[c] R, correlation coefficient of the calibration curve.

[d] LDR, linear dynamic range estimated from the limit of detection to the upper linear concentration.

[e] LOD, limit of detection calculated from equation $LOD = 3S_B/m$, where S_B is the standard deviation of the blank based on 16 measurements and *m* is the slope of the calibration curve based on five concentrations within the LDR.

[f] RSD, relative standard deviation from three sample measurements at medium concentration within LDR.

CHAPTER 3. DETERMINATION OF HIGH-MOLECULAR WEIGHT POLYCYCLIC AROMATIC HYDROCARBONS IN HIGH PERFORMANCE LIQUID CHROMATOGRAPHY FRACTIONS OF COAL TAR STANDARD REFERENCE MATERIAL 1597A VIA SOLID-PHASE NANOEXTRACTION AND LASER-EXCITED TIME-RESOLVED SHPOL'SKII SPECTROSCOPY

3.1. Introduction

Standard reference material (SRM) 1597 is a natural complex sample from Coal Tar originally issued by the National Institute of Standards and Technology (NIST) in 1987 [94]. The Certificate of Analysis for the original SRM 1597 included 12 certified concentrations of PAHs along with 18 noncertified (reference) concentrations that included PAHs and other polycyclic aromatic compounds. Information on the certified concentrations was obtained with a combination of gas chromatography-flame ionization detection (GC/FID) and HPLC-fluorescence detection (HPLC-FL). Noncertified concentrations assignments were solely based on GC/FID.

Since then, SRM 1597 has found widespread and continued use within the analytical community for the validation of methods in environmental matrices. In addition to the compounds included in the original Certificate of Analysis, this SRM has been used to develop methods for the determination of polycyclic aromatic sulfur heterocycles (PASHs) [95,96] .PAHs of molecular mass (MM) 278, 300 and 302 Da [94,97-98], methyl substituted benzo[*a*]pyrene isomers [99,106,108], other methyl and dimethyl-substituted PAHs [100], stable carbon isotope values and radiocarbon content of individual PAH [101], and to investigate the effects of complex PAH mixtures on the activation of carcinogenic PAHs to DNA-binding derivatives and carcinogenesis [102-104].

To address the need for updating the original certified values and expanding the number of PAHs with assigned values, NIST re-analyzed SRM 1597 and reissued it as SRM 1597a [105]. Its Certificate of Analysis included certified concentrations for thirty-four PAHs and reference values for an additional 36 PAHs and 10 PASHs. PAH concentrations were assigned based on results obtained with a combination of GC/MS and reversed-phase HPLC-FL. PASHs concentrations from gas chromatography/mass spectrometry (GC/MS) and reversed-phase LC-FL. PASHs concentrations were determined based on gas chromatography/mass spectrometry (GC/MS) and reversed-phase LC-FL. PASHs concentrations were determined based on GC/MS and GC with atomic emission detection (GC/AED). [95]

This chapter deals with the determination of PAH isomers with MM 302 Da in SRM 1597a. NIST has identified a total of 23 HMW-PAHs with a MM 302 in SRM 1597a [105]. The assignment of mass fraction values for 17 of these HMW-PAHs was based on the analytical approach shown in Figure 14. In methods I – III, the coal tar sample was fractionated by normal phase-LC (NPLC) using a semi-preparative aminopropylsilane (NH_2) column that isolated isomeric fractions prior to PAHs determination via HPLC-FL or GC/MS. HPLC separation was carried out with a silica modified stationary phase (C_{18}).

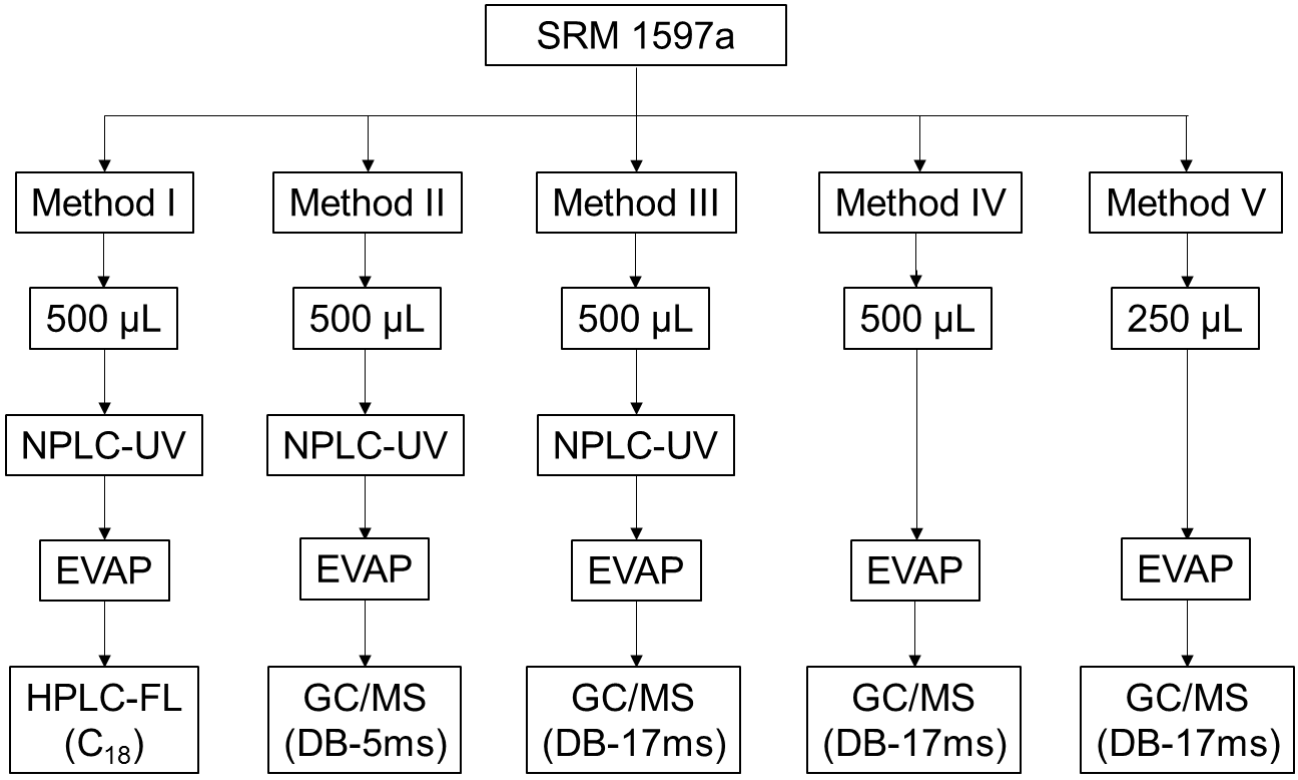

Figure 14. Schematic diagram of the 5 analytical methods listed in the certificate of analysis of SRM1597a for determining the mass fraction values for HMW-PAHs. EVAP = evaporation.

GC separation was accomplished using fused silica capillary columns with one of two stationary phases, namely 5% phenyl-substituted methylpolysiloxane (DB-5ms) or 50% phenyl-substituted methylpolysiloxane (DB-17ms). DB-17ms was also used as the stationary phase in GC/MS methods IV and V to attempt isomers determination without previous sample fractionation.

Herein, DB[*a,e*]P, DB[*a,i*]P, DB[*a,h*]P and N[*2,3-a*]P were selected to evaluate the potential of LETRSS for the analysis of dibenzopyrenes in HPLC fractions of SRM 1597a extracts. The advantages of using solid-phase nanoextraction (SPNE) [114,118-124] for HPLC-fraction pre-concentration are supported with excellent analytical figures of merit. The accuracy of HPLC-SPNE-LETRSS is with dibenzopyrene concentrations statistically equivalent to NIST certified values.

3.2. Experimental

3.2.1. Chemicals and reagents

Nanopure water from a Barnstead Nanopure Infinity water system was used throughout. 20 nm average diameter gold nanoparticles (Au NPs) in aqueous solutions (7×10^{11} particles mL^{-1}) were purchased from Ted Pella, Inc. (Redding, CA). HPLC grade methanol and acetonitrile was purchased from Fisher Scientific (Pittsburg, PA). Analytical grade 1-pentanethiol, toluene, n-octane, n-nonane and n-decane were purchased from Acros Organics (Atlanta, GA). DB[*a,l*]P, DB[*a,e*]P, DB[*a,h*]P and DB[*a,i*]P were purchased from Accustandard at their highest available purity (100%). N[*2,3-a*]P was acquired from Sigma-Aldrich (Milwaukee, WI) at 98% purity. The SRM 1597a extract was prepared by NIST (Gaithersburg, MD) according to an experimental procedure reported previously [126]. Briefly, 36 g of the coal tar sample were processed through an open LC column containing attapulgus clay to remove the highly polar constituents in the sample. The column was eluted with approximately 7 L of 10% methylene chloride in n-pentane and the eluent was collected, evaporated and re-dissolved in 4.5 L of toluene. These quantity values were found to extract a large fraction of PAHs from the original coal tar sample.

Note: use extreme caution when handling PAHs that are known to be extremely toxic.

3.2.2. Pre-concentration of HPLC fractions

HPLC fractions were pre-concentrated via evaporation (EVAP) and SPNE. The SPNE procedure has been described in detail previously [122-125]. Briefly, aliquots of HPLC fractions were mixed with 1 mL of 20 nm gold nanoparticles (Au NPs). The mixture was shaken for 5 min at 1400 rpm and centrifuged for 10 min at 13,400 rpm. The supernatant was separated from the precipitate with a micro-pipette. 2 µL of 1-pentanethiol, 48 µL of methanol, and 50 µL of n-alkane (n-octane, n-nonane, or n-decane) were added to the precipitate. The new mixture was shaken for 5 min at 1400 rpm. The n-alkane was removed with a micro-pipette and analyzed via 4.2 K LETRSS. The EVAP procedure involved drying the HPLC fractions under a gentle stream of ultra-high pure nitrogen and then re-dissolving them in 400 µL of n-alkane for 4.2 K LETRSS analysis.

3.2.3. Ultraviolet-visible absorption spectroscopy

Absorbance spectra were recorded with a single-beam spectrophotometer (model Cary 50, Varian) equipped with a 75-W pulsed xenon lamp, 2-nm fixed bandpass, ± 0.1 nm wavelength precision, and 24 000 nm min^{-1} maximum scan rate. All measurements were made with a 600 µL quartz cuvette with a 1 cm path length.

3.2.4. Room temperature fluorescence spectroscopy

Steady-state excitation and fluorescence spectra were acquired with a commercial spectrofluorimeter (Photon Technology International). The excitation source was a continuous wave 75-W xenon lamp with broadband illumination from 200 to 2000 nm. The excitation and emission monochromators had the same reciprocal linear dispersion (4 nm mm^{-1}), accuracy (± 1 nm), reproducibility (± 2 nm) and spectral resolution (0.25 nm).

Both gratings had 1200 grooves/nm and were blazed at 300 nm (excitation) and 400 nm (emission). Detection was made with a photomultiplier tube (model 1527) with spectral response from 185 to 650 nm. Instrument control was carried out with commercial software (Felix32) specifically designed for the system. Excitation and emission spectra were corrected for wavelength dependence of excitation light source and detector sensitivity, respectively. Correction was made in the post-acquisition mode using the radiometric correction factors included in Felix32 software. Long pass filters were used when necessary to eliminate second-order emission from the excitation source. Room-temperature measurements were made from un-degassed solutions in 600 µL quartz cuvettes with 1 cm optical path length. 77 K measurements followed the classical procedure of immersing an un-degassed sample solution in a quartz tube into a nitrogen-filled Dewar flask. The length of the quartz tube (25 m) and the design of the Dewar allow for samples to be analyzed without any interference from condensation. Condensation occurs at the top of the Dewar but the sample is analyzed at the bottom section of the quartz tube. A 90^{o} excitation/emission configuration was used in all measurements

3.2.5. HPLC Instrumentation

HPLC analysis was performed using a computer-controlled Hitachi (San Jose, CA) HPLC system equipped with a (model L-7100) gradient pump, an (L-7400 UV) detector, and (L-7485) fluorescence detector, an online degasser (L-761) and a (D-7000) control interface. Separation was carried out on a Supelco (Bellefonte, PA) Supelcosil TM LC-PAH column with the following characteristics: 15 cm length, 4 mm diameter, and 5 µm average particle diameters. All sample injections were held constant at 20 µL using a fixed-volume injection loop.

HPLC fractions were collected in 7.0 mL amber sample vials with the aid of a Gilson fraction collector (model FC 20313).

3.2.6. Instrumentation for 4.2K LETRSS

Measurements were carried out with the multidimensional luminescence system described previously in section 2.3 of this dissertation.

3.2.7. Sample freezing procedures

4.2 K fluorescence measurements were carried out with the cryogenic fiber optic probe and the freezing procedure described in chapter 2.2.

3.3. Results and Discussion

3.3.1. HPLC analysis of SRM 1597a for HMW-PAHs

Previous work reported by Wise et al. demonstrated the ability to separate 12 isomers of MM 302 – including – from an SRM 1597 extract using a polymeric C_{18} column [94]. Separation was achieved using a 100% acetonitrile mobile phase, a flow rate of 1.5 mL min^{-1} and a column temperature of 29 ^{o}C. Figure 15A shows a typical fluorescence chromatogram of a standard mixture of DB[*a,l*]P, DB[*a,e*]P, DB[*a,i*]P, N[*2,3-a*]P and DB[*a,h*]P in toluene recorded in our lab under similar chromatographic conditions. With the exception of the 29 ^{o} C column temperature, which we had no instrumental capability to reproduce, the chromatographic conditions were the same as those reported previously [94].

At room temperature, the separation of the five isomers was achieved in 40 min of analysis time. Fluorescence detection used the following time-programmed excitation/emission wavelengths: 0.0 min, 316/424; 10.0 min, 303/398; 20.0 min, 394/434; 29.3 min, 332/460; and 33.0 min, 313/447.

All excitation and emission wavelengths corresponded to the maximum values obtain from pure standard spectra in 100% acetonitrile (see spectra in appendix A). Three chromatographic runs of the same standard mixture recorded from three independent injections of 20 μL aliquots provided the following average retention times (min): 8.89 ± 0.02 (DB[*a,l*]P), 12.8 ± 0.06 (DB[*a,e*]P), 28.5 ± 0.23 (DB[*a,i*]P), 30.0 ± 0.25 (N[*2,3-a*]P) and 35.6 ± 0.29 (DB[*a,h*]P). Figure 15B shows the fluorescence chromatogram of the SRM 1597a sample diluted with toluene to a ratio that provided concentrations of DB[*a,l*]P (19.5 μg L^{-1}), DB[*a,e*]P (157.3 μg L^{-1}), DB[*a,i*]P (67.0 μg L^{-1}), N[*2,3-a*]P (74.3 μg L^{-1}) and DB[*a,h*]P (44.5 μg L^{-1}) identical to those from the pure standards. The complexity of the coal tar sample can be clearly noticed by the large number of chromatographic peaks. Comparison of fluorescence intensities to those in Figure 15A, suggests potential overlapping of co-eluted peaks that could result in the inaccurate determination of the targeted isomers via HPLC analysis.

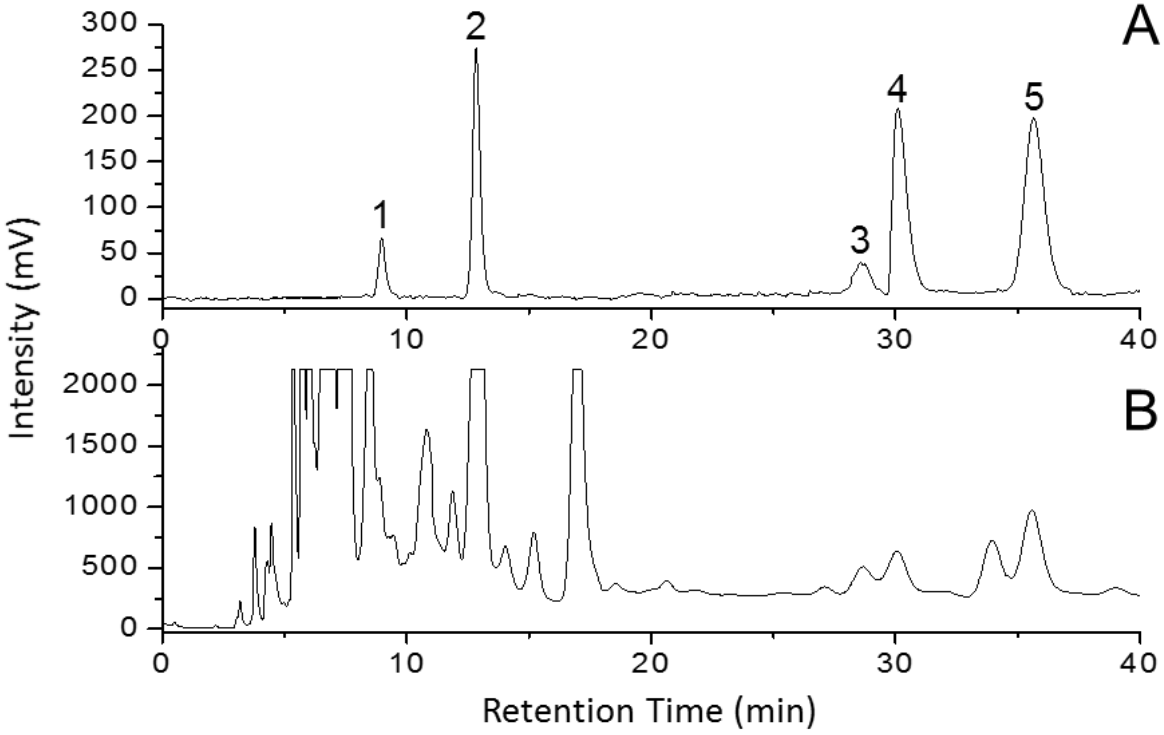

Figure 15. (A) Fluorescence chromatogram of a synthetic mixture containing (1) DB[*a,l*]P at 19.4 µg L^{-1}, (2) DB[*a,e*]P at 157.3 µg L^{-1}, (3) DB[*a,i*]P at 67.0 µg L^{-1}, (4) N[*2,3-a*]P at 74.3 µg L^{-1} and (5) DB[*a,h*]P at 44.5 µg L^{-1}. These concentrations match the certified concentrations reported for the HMW-PAHs in the certificate of analysis for SRM 1597a. The mobile phase was 100% acetonitrile and a flow rate of 1.5 mL min^{-1}. Excitation and emission wavelengths were as follows: 316/424 nm (DB[*a,l*]P), 303/398 nm (DB[*a,e*]P), 332/465 nm (DB[*a,i*]P and N[*2,3-a*]P), and 313/447 nm (DB[*a,h*]P). (B) Fluorescence chromatogram of the SRM 1597a using the same conditions in Figure 15A.

3.3.2. 4.2 K LETRSS analytical figures of merit

Figure 16 shows the molecular structures of the 23 isomers with molecular mass of 302 Da previously identified by NIST in the SRM 1597a. For the specific case of the 5 targeted isomers, the host - guest molecular length matching criterion for best spectral resolution [122-127] leads to one of the following three n-alkanes: n-octane (DB[*a,l*]P and DB[*a,e*]P), n-nonane (DB[*a,i*]P), and n-decane (N[*2,3-a*]P and DB[*a,h*]P).

As shown in Figures17-21, these three solvents provide excitation and fluorescence spectra with vibrational features commonly observed in 77 K Shpol'skii spectroscopy. Sample excitation with our tunable dye laser at the maximum excitation wavelength of each isomer – i.e., 321 nm (DB[*a,l*]P), 307 nm (DB[*a,e*]P), 398 nm (DB[*a,i*]P, 336 nm (N[*2,3-a*]P) and 314 nm (DB[*a,h*]P) – would require the use of three laser dyes, namely Rhodamine 640 (DB[*a,e*]P and DB[*a,h*]P), DCM (DB[*a,l*]P and N[*2,3-a*]P) and LDS 798 (DB[*a,i*]P). For the sake of operational simplicity, we opted to use a single laser dye (DCM) for sample excitation within the 305– 325 nm range.

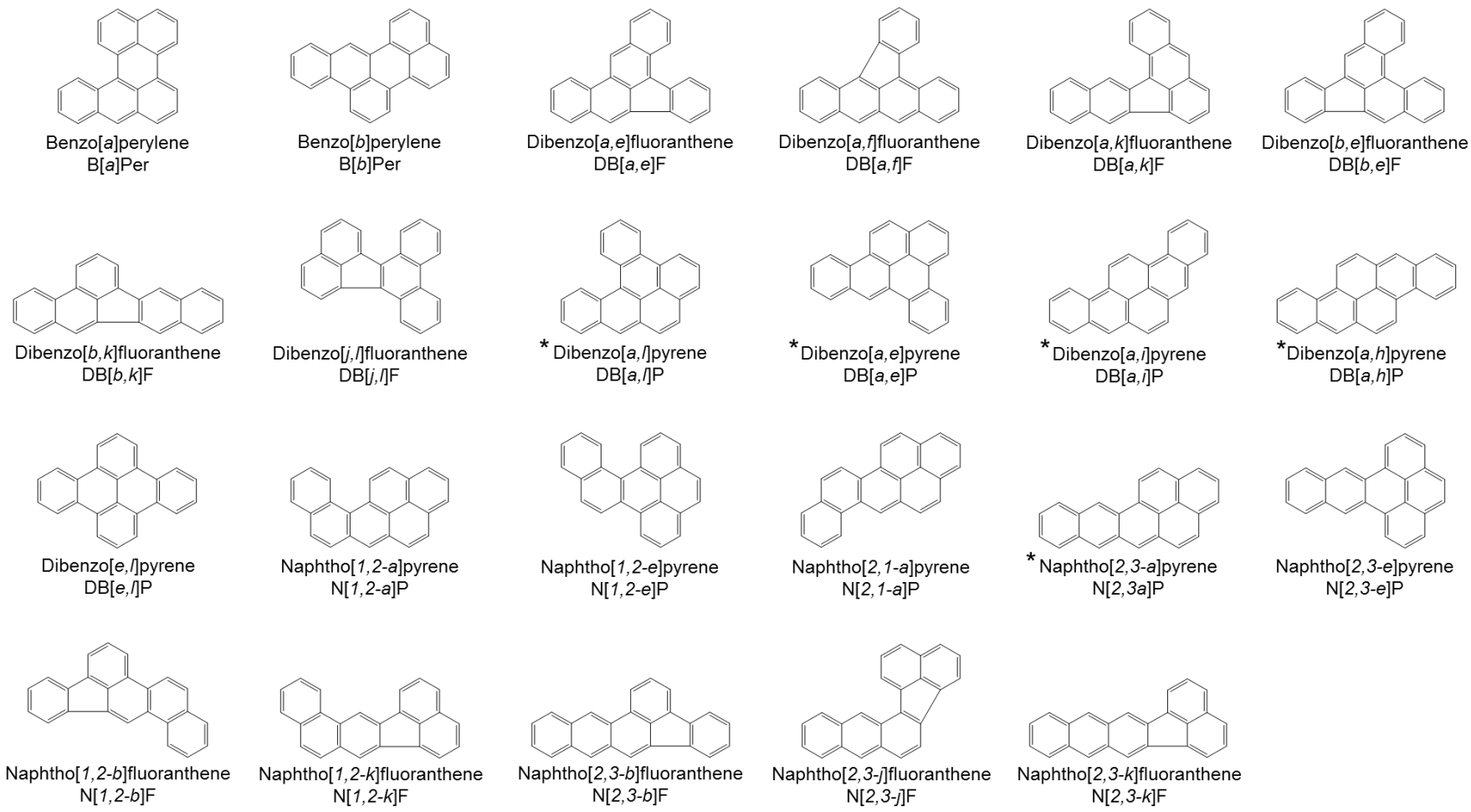

Figure 16. Molecular structures of the 23 PAHs isomers with molecular mass of 302 Da previously identified by NIST in the SRM 1597a. (*) denotes isomers investigated in this study.

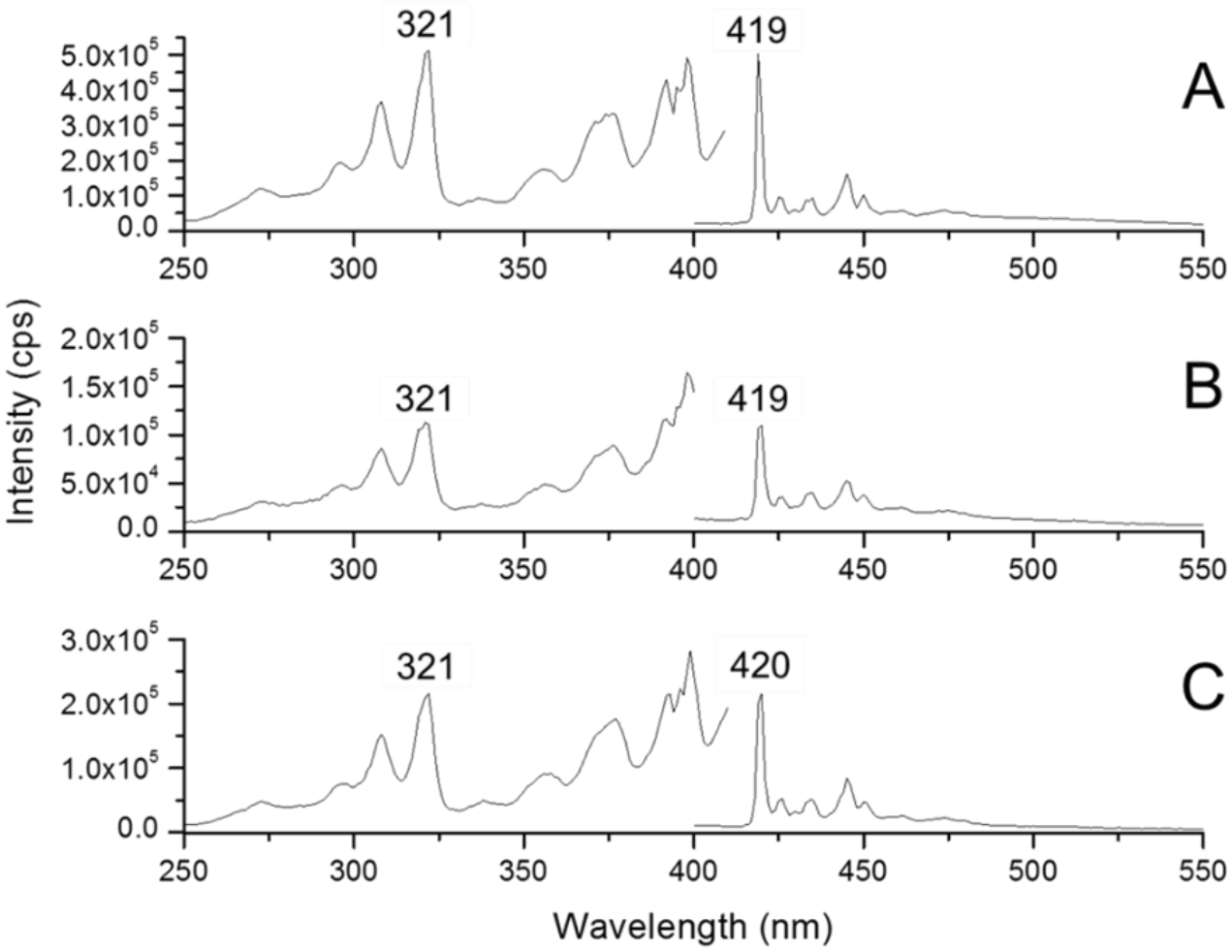

Figure 17. 77 K excitation and fluorescence spectra of DB[*a*,*l*]P in (A) n-octane, (B) n-nonane and (C) n-decane at 100 ng mL^{-1}. The spectra were collected at maximum excitation and emission wavelengths with a 1 nm band pass

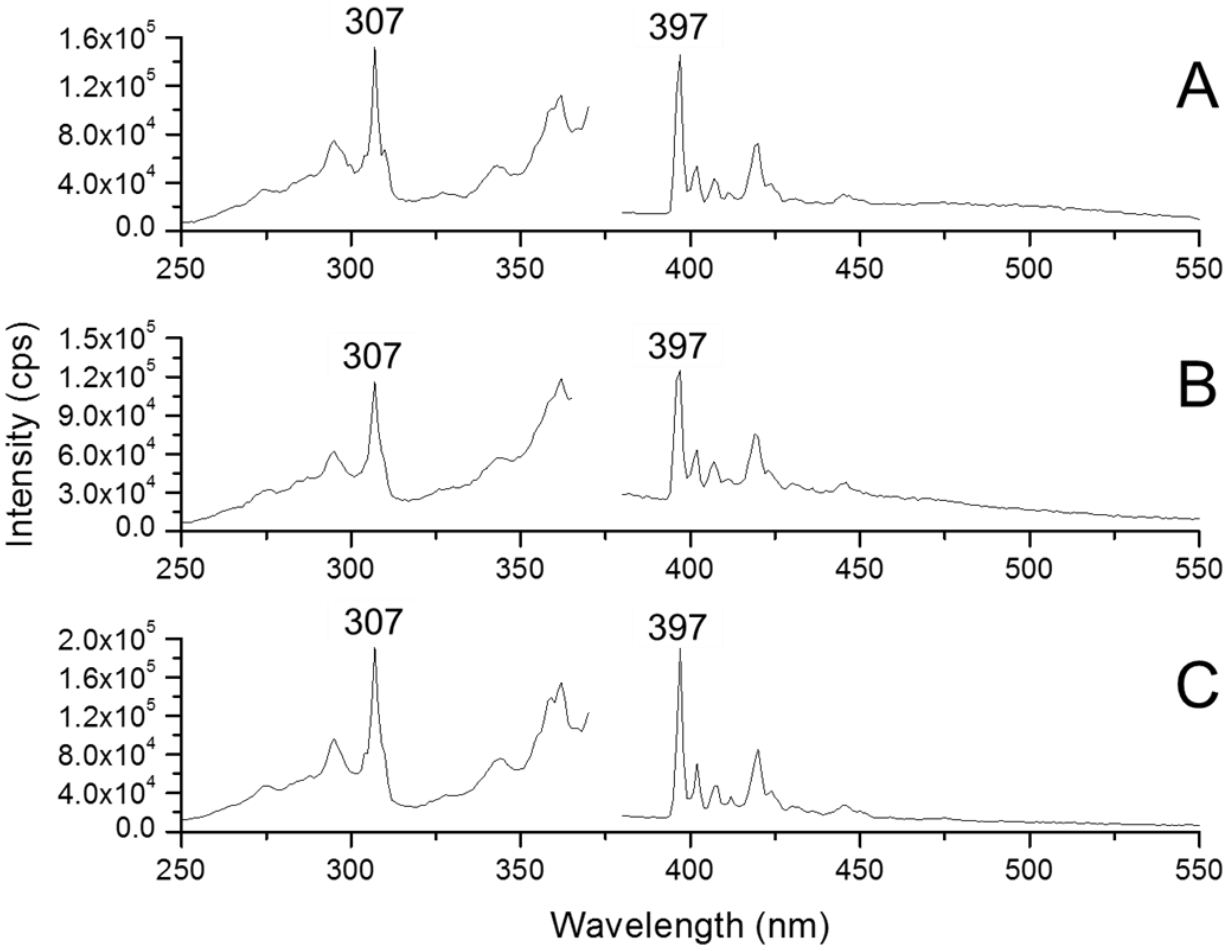

Figure 18. 77 K excitation and fluorescence spectra of DB[*a*,*e*]P in (A) n-octane, (B) n-nonane and (C) n-decane at 100 ng mL^{-1}. The spectra were collected at maximum excitation and emission wavelengths with a 1 nm band pass.

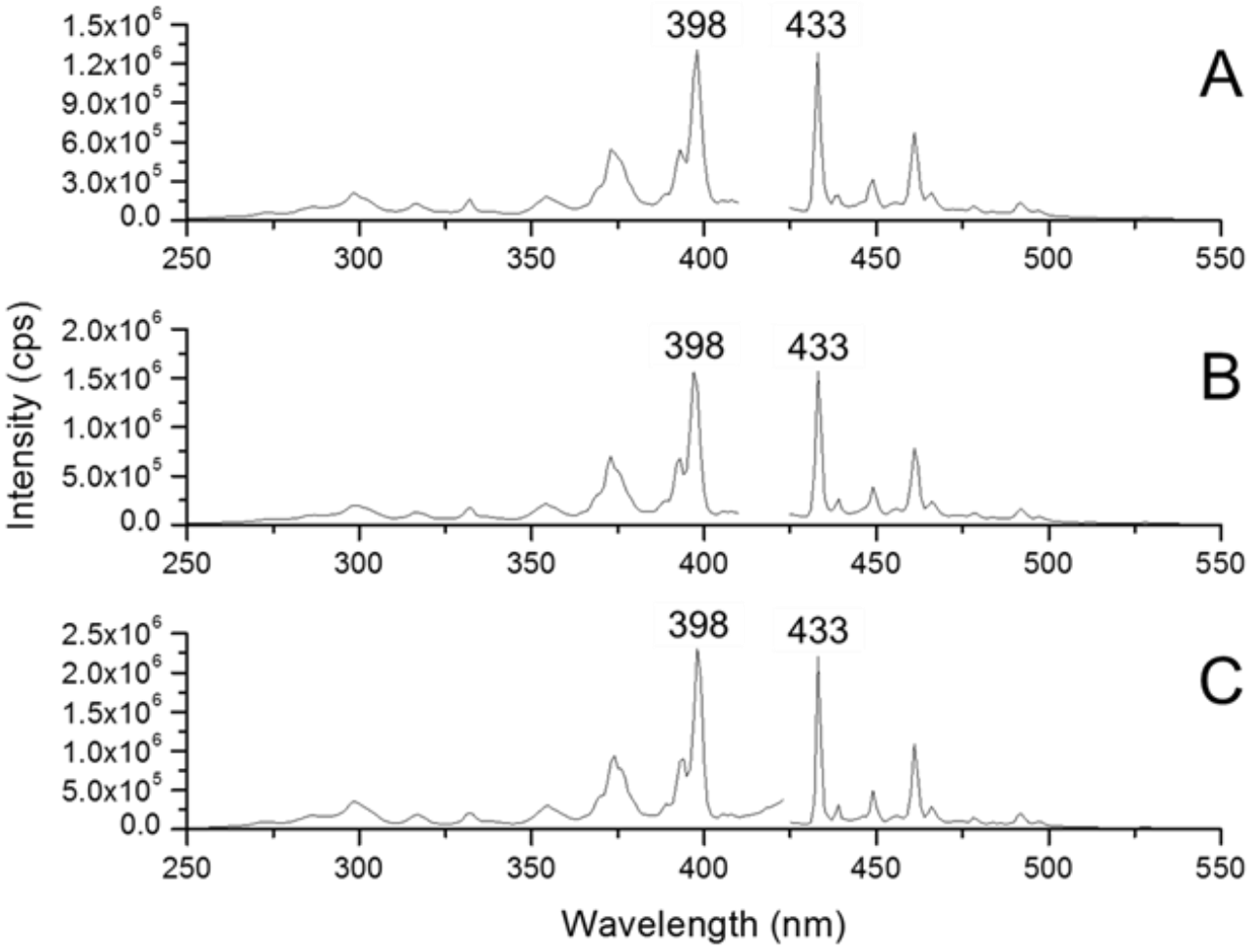

Figure 19. 77 K excitation and fluorescence spectra of DB[*a*,*i*]P in (A) n-octane, (B) n-nonane and (C) n-decane at 100 ng mL^{-1}. The spectra were collected at maximum excitation and emission wavelengths with a 1 nm band pass.

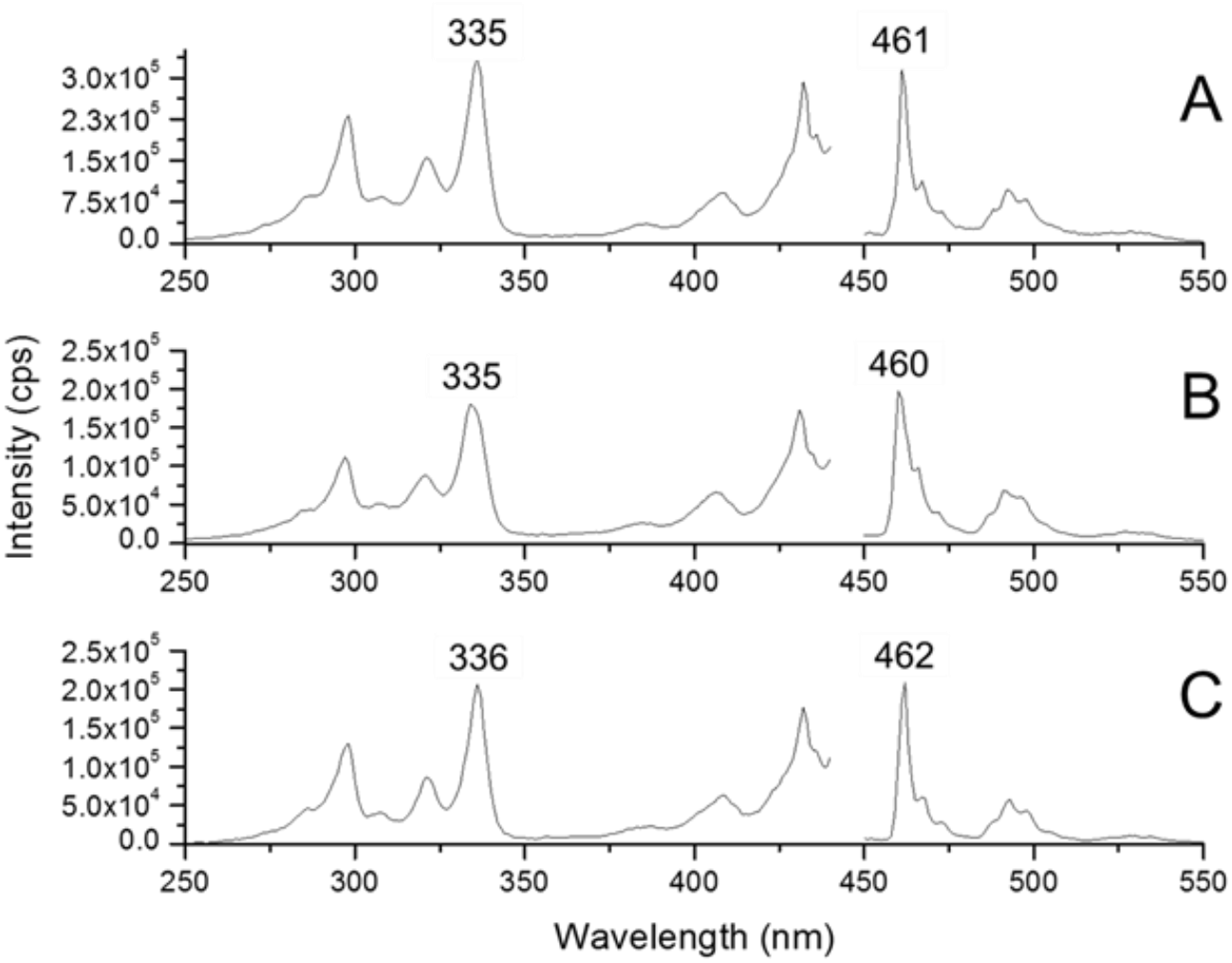

Figure 20. 77 K excitation and fluorescence spectra of DB[*a*,*h*]P in (A) n-octane, (B) n-nonane and (C) n-decane at 100 ng mL^{-1}. The spectra were collected at maximum excitation and emission wavelengths with a 1 nm band pass

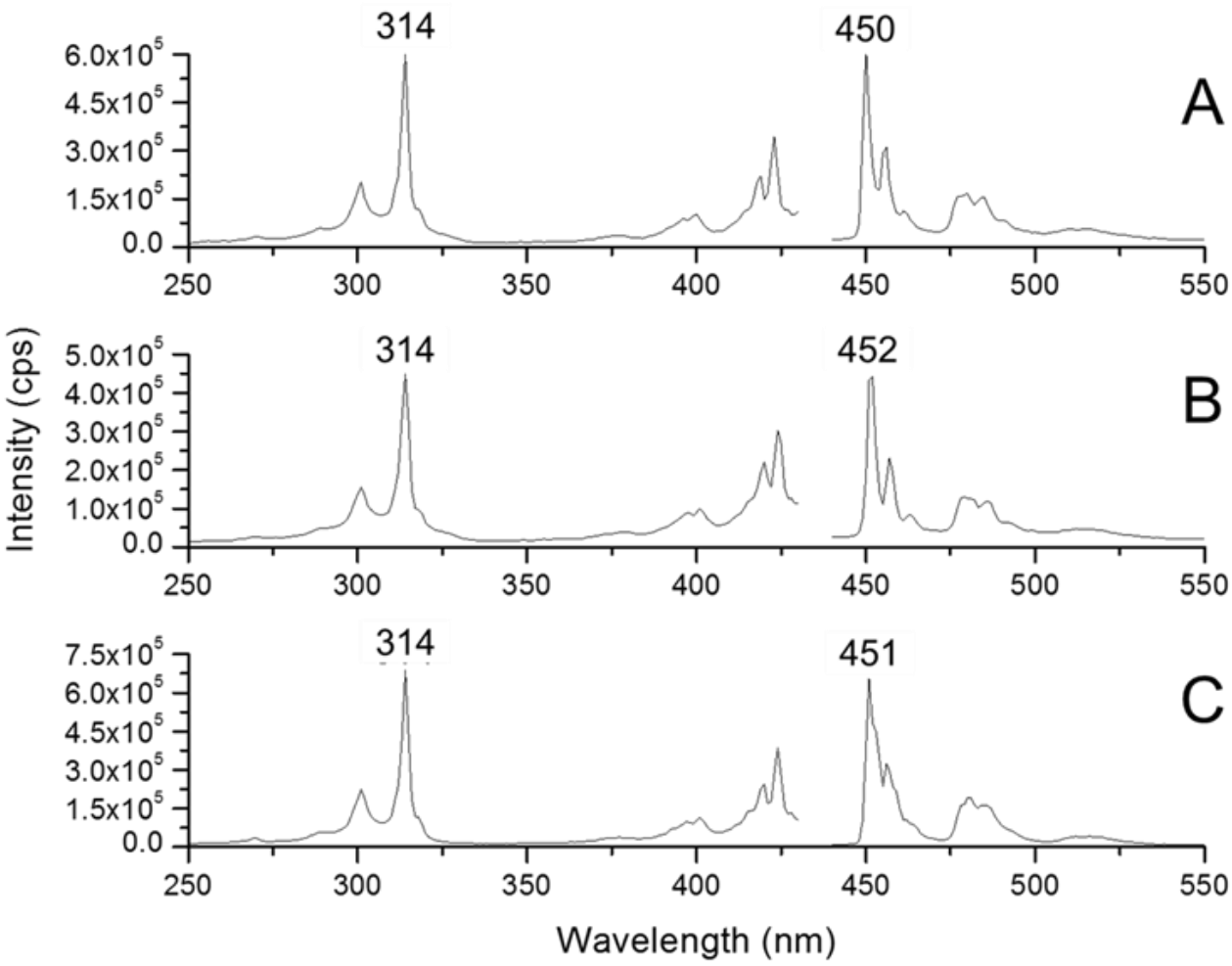

Figure 21. 77 K excitation and fluorescence spectra of DB[*a*,*h*]P in (A) n-octane, (B) n-nonane and (C) n-decane at 100 ng mL^{-1}. The spectra were collected at maximum excitation and emission wavelengths with a 1 nm band pass.

Table 5 lists the excitation wavelengths that provided the highest fluorescence intensity for each HMW-PAHs within the wavelength excitation range of DCM. The delay (t_d) and gate (t_g) widths were optimized to collect most of the PAH fluorescence and still avoid instrumental noise. The gate steps (t_s) were optimized to record a sufficient numbers of data points within the lifetime decay of each PAHs. With the exception of DB[*a,i*]P, the highest fluorescence intensity and narrowest full-width half-maximum (FWHM) were obtained with the n-alkane that best matched the length of the PAH. Within a confidence interval of 95% ($N_1 = N_2 = 3$), [128] the highest fluorescence intensity and narrowest FWHM of DB[*a,i*]P were obtained in n-octane and n-decane. The choice of n-alkane did not cause considerable changes in the lifetimes of the studied PAHs. Well-behaved, single exponential decays of fluorescence intensity versus time were observed in all cases. The first two lifetimes decay agreed to within about 1% and the residuals showed no systematic trends.

Figure. 22A – E show the 4.2 K LETRSS fluorescence spectra of DB[*a,l*]P, DB[*a,e*]P, DB[*a,i*]P, N[*2,3-a*]P and DB[*a,h*]P in their best matching n-alkane solvent. Table 6 summarizes the 4.2 K LETRSS AFOMs of each isomer using the current International Union for Pure and Applied Chemistry (IUPAC) guidelines [129.] Calibration curves were built using a minimum of five standard solutions of each PAHs. All fluorescence measurements were made at the maximum emission wavelength of each PAHs. No attempts were made to reach the upper concentration limit of the linear dynamic range (LDR). All intensities plotted in the calibration graphs were measured under the optimum delay and gate times for each PAHs (see Table 5). The existence of linear relationships was confirmed by comparing experimental F-test values (F_{exp}) to critical F-test values (F_{crit}). F_{exp} were calculated using equation 3.1:

$$F_{exp} = \left(\frac{S_{y/x}}{S_y}\right)^2 \quad (3.1)$$

Where $S_{y/x}$ is the residual standard deviation and S_y is the pure error. These parameters can be calculated from the calibration data with equations 3.2 and 3.3:

$$S_{y/x} = \sqrt{\frac{\sum_{i=1}^{I}(y_i - \hat{y}_l)^2}{I-2}} \quad (3.2)$$

$$S_y = \sqrt{\frac{\sum_{l=1}^{L}\sum_{q=1}^{Q}\left(y_{lq} - y_l\right)^2}{I-Q}} \quad (3.3)$$

where y_i and $\hat{y}_l$ are the experimental and estimated response values for sample i, y_{lq} is the calibration response for replicate q at level l, y_l is the mean response at level l, and I, L, and Q are the total number of calibration samples, levels, and replicates at each level, respectively. In all cases, the F_{exp} was lower than F_{crit} demonstrating the excellent linear relationships between PAH concentrations and fluorescence signal. The LODs were calculated according to equation 3.4:

$$LOD = \frac{3.3 S_{y/x}}{A}\sqrt{1 + h_0 + \frac{1}{I}} \quad (3.4)$$

where A to the slope of the calibration graph, I is the number of calibration samples, and h_0 is the leverage for the blank sample shown equation 3.5:

$$h_0 = \frac{C_{cal}^2}{\sum_{i=1}^{I}(C_i - C_{cal})^2} \quad (3.5)$$

Where C_{cal} refers to the mean calibration concentration and C_i is each of the calibration concentration values.

The LODs varied from 0.02 µg L^{-1} (DB[*a*,*l*]P and N[*2*,*3*-*a*]P) to 0.24 µg L^{-1} (DB[*a*,*e*]P). Similar concepts apply to the limit of quantitation (LOQ) as shown in equation 3.6,

$$LOQ = \frac{10S_{y/x}}{A}\sqrt{1 + h_0 + \frac{1}{I}} \tag{3.6}$$

Which corresponds to lowest linear concentration in LDR. The RSD values reflect the excellent reproducibility of LETRSS measurements. All further studies were carried out using the n-alkane solvents listed in Table 6.

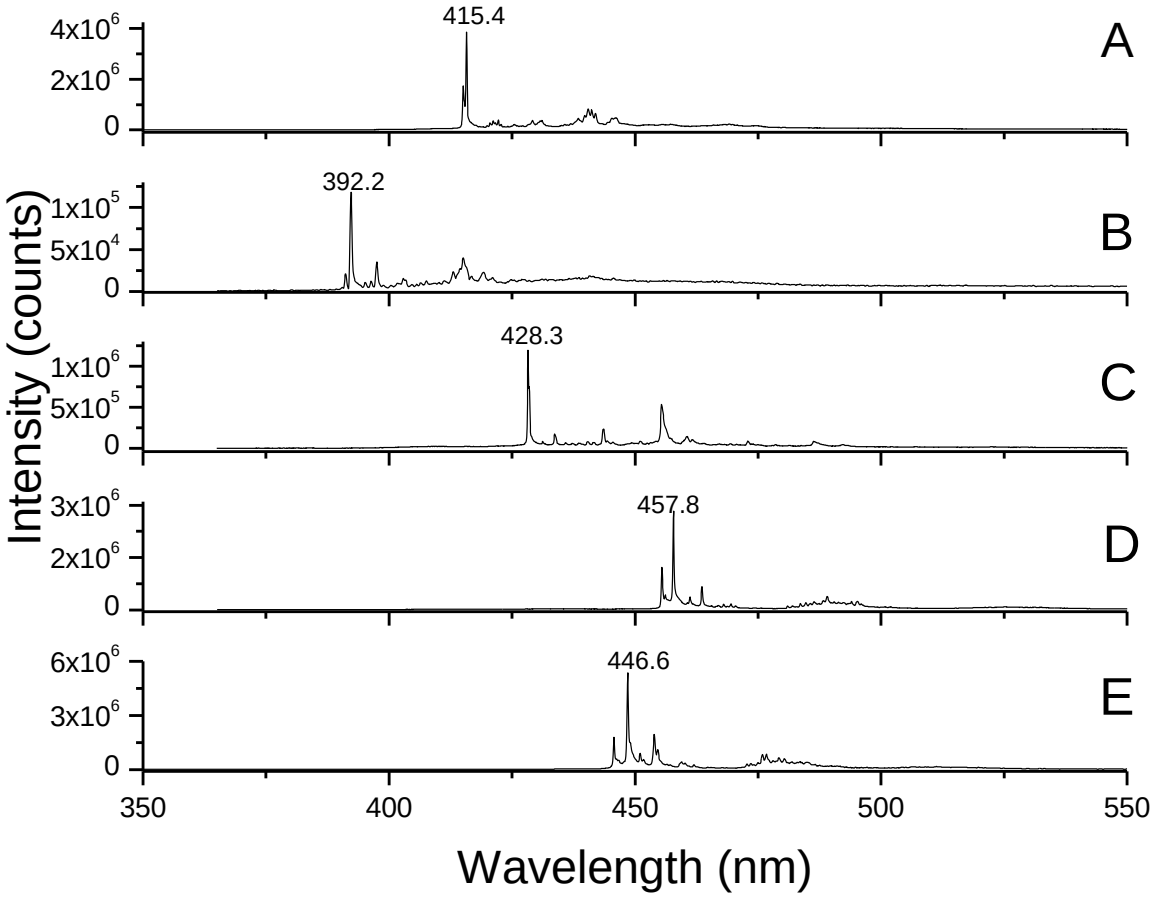

Figure 22. 4.2 K LETRSS fluorescence spectra of 100 ng mL^{-1} (A) DB[*a*,*l*]P in n-octane (λ_{exe}= 318.0 nm, λ_{em} = 415.4 nm, 0 ns delay and 250 ns gate time); (B) DB[*a*,*e*]P in n-octane (λ_{exe}= 306.4 nm, λ_{em} = 392.4 nm, 10 ns delay and 150 ns gate time); (C) DB[*a*,*i*]P in n-decane (λ_{exc}= 312.0 nm, λ_{em} = 428.3 nm, 10 ns delay and 650 ns gate time); (D) N[*2*,*3*-*a*]P in n-decane (λ_{exe}= 317.0 nm, λ_{em} = 457.8 nm, 0 ns delay and 25 ns gate time) and (E) DB[*a*,*h*]P in n-decane (λ_{exc} = 310.0 nm, λ_{em} = 446.6 nm, 0 ns delay and 15 ns gate time). All spectra correspond to the accumulation of 100 laser pulses. The spectrograph slit was 42µm

Table 5 Spectral comparison of five HMW-PAH isomers via 4.2 K LETRSS

HMW-PAHs [a]	n-alkane	$\lambda_{exc}/\lambda_{em}$ [b,g] (nm)	$t_d/t_g/t_s$ [c] (ns)	I_F (x 10^5) [d] (counts)	FWHM [e] (nm)	τ [f,h] (ns)
DB[*a,l*]P	n-octane	318.0/415.4	10/250/6	39.4 ± 0.81	0.23 ± 0.01	78.1 ± 1.03
	n-nonane	318.0/415.7		7.28 ± 0.17	0.69 ± 0.01	77.5 ± 0.83
	n-decane	318.0/415.6		6.92 ± 0.11	0.52 ± 0.01	77.3 ± 0.86
DB[*a,e*]P	n-octane	306.4/392.2	10/150/5	1.19 ± 0.07	0.28 ± 0.01	54.3 ± 1.39
	n-nonane	305.0/391.9		0.64 ± 0.01	0.38 ± 0.03	63.9 ± 2.49
	n-decane	306.0/392.4		0.72 ± 0.03	0.61 ± 0.03	67.0 ± 1.25
DB[*a,i*]P	n-octane	312.0/428.3	10/650/20	11.6 ± 0.20	0.32 ± 0.01	216.2 ± 1.70
	n-nonane	312.0/428.8		8.57 ± 0.10	0.51 ± 0.01	226.2 ± 2.40
	n-decane	312.0/428.3		11.9 ± 0.30	0.33 ± 0.01	211.6 ± 7.20
N[*2,3-a*]P	n-octane	318.0/456.9	0/25/1	16.5 ± 0.70	0.72 ± 0.05	7.90 ± 0.11
	n-nonane	317.0/455.8		10.2 ± 0.50	1.12 ± 0.09	7.90 ± 0.01
	n-decane	317.0/457.8		26.4 ± 0.30	0.29 ± 0.01	6.83 ± 0.05
DB[*a,h*]P	n-octane	310.0/445.6	0/15/1	17.1 ± 0.10	0.44 ± 0.01	6.17 ± 0.14
	n-nonane	310.0/446.5		31.6 ± 0.60	0.58 ± 0.02	6.30 ± 0.10
	n-decane	310.0/446.6		50.0 ± 0.60	0.31 ± 0.01	6.31 ± 0.09

[a] All HMW-PAH solutions were made in their perspective n-alkane solvents.

[b] Excitation (λ_{exc}) and fluorescence (λ_{em}) wavelengths.

[c] Optimum gate delay (t_d), gate width (t_g) and gate step (t_s).

[d] Fluorescence intensity (I_F) of HMW-PAHs in the frozen n-alkane matrices. All fluorescence intensities represent an average of nine independent measurements made at the maximum emission wavelengths of each HMW-PAH.

[e] Full width at half-maximum (FWHM).

[f] Average fluorescence lifetime of three measurements taken from three frozen aliquots.

[g, h] See appendices B and C respectively.

Table 6 AFOM for the five HMW-PAHs via 4.2 K LETRSS in their optimal n-alkane solvents

HMW-PAH[a,f]	n-alkane	LDR[b] (µg L^{-1})	R^{2} [c]	LOD[d] (µg L^{-1})	RSD[e] (%)
DB[*a,l*]P	n-octane	0.05 – 100	0.9981	0.02	3.96
DB[*a,e*]P	n-octane	0.94 – 100	0.9996	0.29	5.88
DB[*a,i*]P	n-decane	0.19 – 100	0.9974	0.06	2.19
N[*2,3-a*]P	n-decane	0.17 – 50	0.9975	0.05	2.15
DB[*a,h*]P	n-decane	0.12 – 50	0.9998	0.04	2.67

[a] All HMW-PAH solutions were made in their perspective n-alkane solvents.

[c] LDR, linear dynamic range; lower concentration limit =LOQs were calculated on the basis of equation 3.6.

[d] R = correlation coefficient.

[e] LODs were calculated on the basis of equation 3.4.

[e] Relative standard deviation (RSD) = S_F/I_F x 100, where S_F is the standard deviation of the average calculated from six fluorescence measurements at medium linear PAH concentrations.

[f] see appendix D for calibration curves.

3.3.3. Pre-concentration of HPLC Fractions for 4.2 K LETRSS Analysis

Several approaches have been reported for the pre-concentration of PAHs from HPLC fractions. These include liquid-liquid extraction (LLE) [117,127,130], solid-phase extraction (SPE) [117,127,130], evaporation (EVAP) [94,128] and SPNE [118]. This section compares the analytical performance of EVAP and SPNE for the LETRSS analysis of the five targeted isomers. Both methods have the strengths of simplicity, cost effectiveness and reduced solvent consumption. Pre-concentration via EVAP is accomplished by applying a steady stream of ultrapure nitrogen gas for approximately 30 min and re-dissolving the solid residue with microliters of Shpol'skii solvent for LETRSS analysis. SPNE pre-concentrates PAHs by mixing the HPLC fraction with Au NPs. After centrifugation and decantation of the supernatant, the Au NPs precipitate is mixed with a PAH releasing solvent mixture (1-pentanethiol/methanol/n-alkane) for LETRSS analysis.

Table 7 summarizes the AFOMs of HPLC-EVAP-LETRSS and HPLC-SPNE-LETRSS analysis for the five HMW-PAHs. Overall recovery (OR) values were calculated according to equation 3.7:

$$OR\ (\%) = \frac{[PAH]_A * V_A}{C_{PAH} * V_S} * 100 \qquad (3.7)$$

where C_{PAH} refers to the PAH concentration in the original sample, V_S to the extracted volume of sample, $[PAH]_A$ corresponds to the concentration of PAH in the final volume of n-alkane solvent (V_A). As shown in Figure 23, the optimum V_A values for EVAP were 400 µL. Previous work in our lab has shown that 50 µL of n-alkane solvent is sufficient to achieve excellent analytical recoveries of PAHs[118-123].

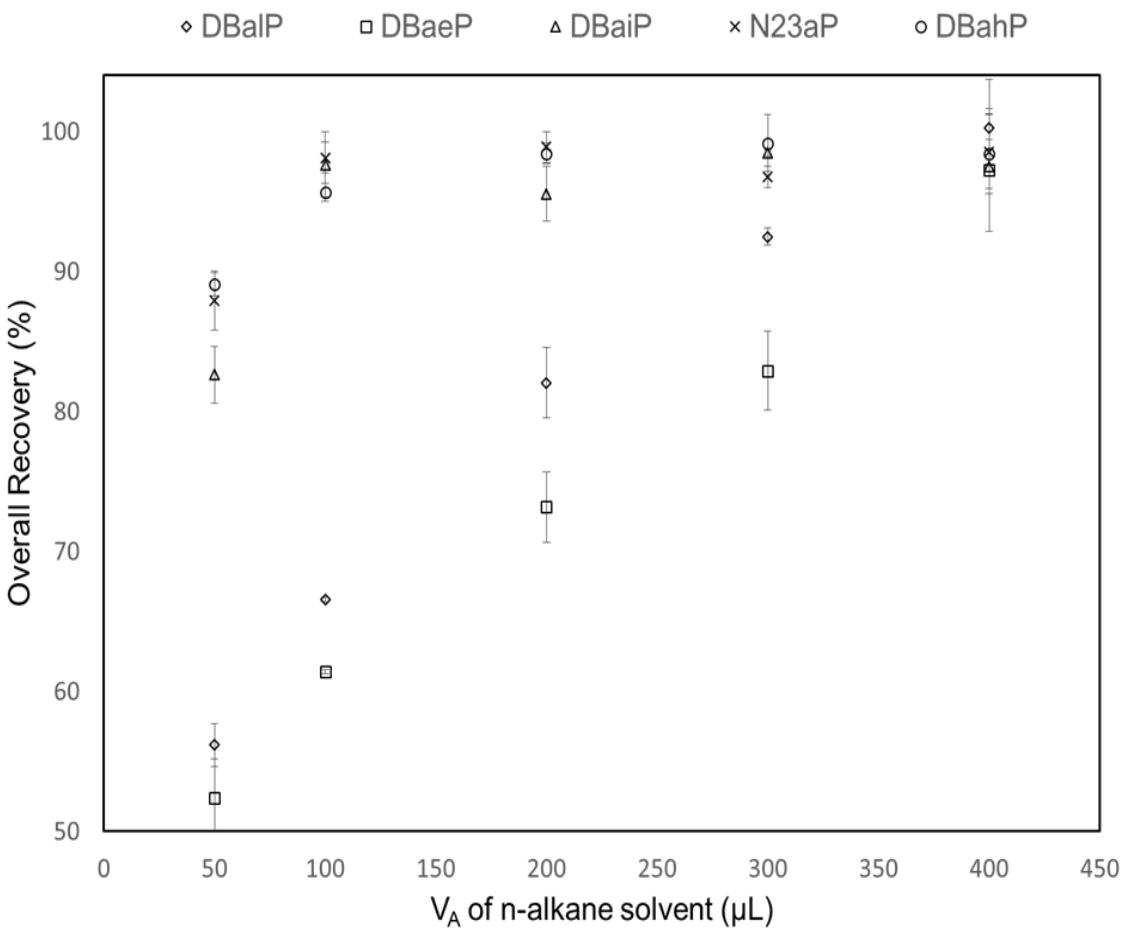

Figure 23. The overall recoveries for the evaporation step of the HPLC fractions when adding different amounts of the appropriate n-alkane solvent (see Table 6). V_A values were obtained from three chromatographic runs of a five PAH synthetic mixture containing 10 ng mL^{-1} individual isomer concentrations

Table 7 AFOM comparison for the pre-concentration of the 5 HMW-PAHs in HPLC fractions

	EVAP-LETRSS[g]					SPNE-LETRSS[h]				
HMW-PAH [a]	OR [b] (%)	LDR [c] (µg L^{-1})	R^2 [d]	LOD [e] (µg L^{-1})	RSD [f] (%)	OR [b] (%)	LDR [c] (µg L^{-1})	R^2 [d]	LOD [e] (µg L^{-1})	RSD [f] (%)
DB[*a*,*l*]P	100. ± 3.42	0.94 – 100	0.9981	0.29	3.41	98.2 ± 5.5	0.12 – 10	0.9990	0.04	5.60
DB[*a*,*e*]P	97.2 ± 4.37	18.0 – 100	0.9996	5.45	4.49	99.5 ± 2.8	2.30 – 10	0.9940	0.70	2.81
DB[*a*,*i*]P	97.5 ± 1.93	3.68 – 100	0.9974	1.12	1.98	102.7 ± 3.2	0.47 – 10	0.9994	0.14	3.12
N[*2*,*3*-*a*]P	98.6 ± 2.63	3.36 – 100	0.9975	1.02	2.67	102.6 ± 4.1	0.43 – 10	0.9955	0.13	4.00
DB[*a*,*h*]P	98.4 ± 2.84	2.61 – 100	0.9998	0.79	2.89	102.2 ± 6.0	0.27 – 10	0.9992	0.09	5.87

[a] All HMW-PAH synthetic mixture solutions were made in methanol.

[b] OR, overall recovery of HMW-PAHs.

[c] LDR, linear dynamic range; lower concentration limit =LOQs were calculated on the basis of equation 3.6.

[d] R = correlation coefficient.

[e] LODs were calculated on the basis of equation 3.4.

[f] Relative standard deviation (RSD) = S_F/I_F x 100, where S_F is the standard deviation of the average calculated from six fluorescence measurements at medium linear PAH concentrations.

[g, f] see appendices E and F respectively for calibration curves.

Within a confidence interval of 95% and three replicate trials ($\alpha = 0.05$; $N = 3$), the obtained overall recoveries in Table 7 for both pre-concentration methods were statistically equivalent to 100% [128]. Each calibration curve was built with at least five synthetic mixtures of HMW-PAHs. Each signal plotted in the calibration graph was the average of at least three HPLC-LETRSS measurements recorded from three independent aliquots. AFOM were calculated based on the same equations described in section 3.2.2. No efforts were made to reach the upper linear concentration of the LDR. SPNE provided better LODs than EVAP. The LOD improvements result from the 8x smaller n-alkane volume (V_A) of the procedures of SPNE (50 µL) in comparison to the EVAP (400 µL). All further studies were then carried out using SPNE as the pre-concentrating approach for HPLC-LETRSS analysis.

3.3.4. Accuracy of HPLC-SPNE-LETRSS

Table 8 compares the NIST mass fraction certified values of the five targeted HMW-PAHs to those obtained in our lab via HPLC-SPNE-LETRSS. The NIST certified values correspond to the averages of the mass fractions obtained with methods I-V (see Figure 14). Within a confidence interval of 95% and three replicate trials ($N = 3$), the mass fractions obtained via HPLC-SPNE-LETRSS were statistically equivalent to the NIST certified values. It should be noted that only one of the NIST methods (Method III) was able to determine all five isomers in the coal tar sample extract.

Table 8 Comparison of certified and the experimental concentrations for 5-HMW PAHs

HMW-PAH	Reported Values [a] (mg Kg^{-1})	Experimental [b] (mg Kg^{-1})	t-test [c]
DB[*a*,l]P	1.12 ± 0.08	0.93 ± 0.16	1.50
DB[*a*,*e*]P	9.08 ± 0.20	9.47 ± 0.51	1.43
DB[*a*,*i*]P	3.87 ± 0.17	3.64 ± 0.36	1.14
N[*2*,*3*-*a*]P	4.29 ± 0.45	3.67 ± 0.79	1.45
DB[*a*,*h*]P	2.57 ± 0.15	2.50 ± 0.27	0.48

[a] Mass fraction and standard deviations from the certificate of analysis for SRM 1597a.
[b] Mass fraction and standard deviations determine from the HPLC fractions via 4.2 K SPNE-LETRSS.
[c] t-test of PAH concentrations from HPLC fractions compared to concentration values listed in the certificate of analysis. $t_{critical} = 2.78$ ($\alpha = 0.05$; $N_{rep} = 2 – 5$ and $N_{exp} = 3$)

Figure 24A – E shows the 4.2 K fluorescence spectra and lifetimes of the five targeted isomers obtained from the HPLC fractions of the coal tar sample. Each spectrum was recorded using the best gate and excitation wavelengths listed in Table 1.

Table 9 compares the 4.2 K fluorescence lifetimes of pure standards to those recorded from HPLC fractions of the SRM 1597a sample. The statistical equivalence observed in all cases ($\alpha = 0.05$; $N_1 = N_2 = 6$) [128] confirms peak assignments for the unambiguous determination of each molecular mass 302 isomer. Single exponential decays were observed in all cases demonstrating peak purity of HPLC fractions for accurate quantitative analysis of HMW-PAHs.

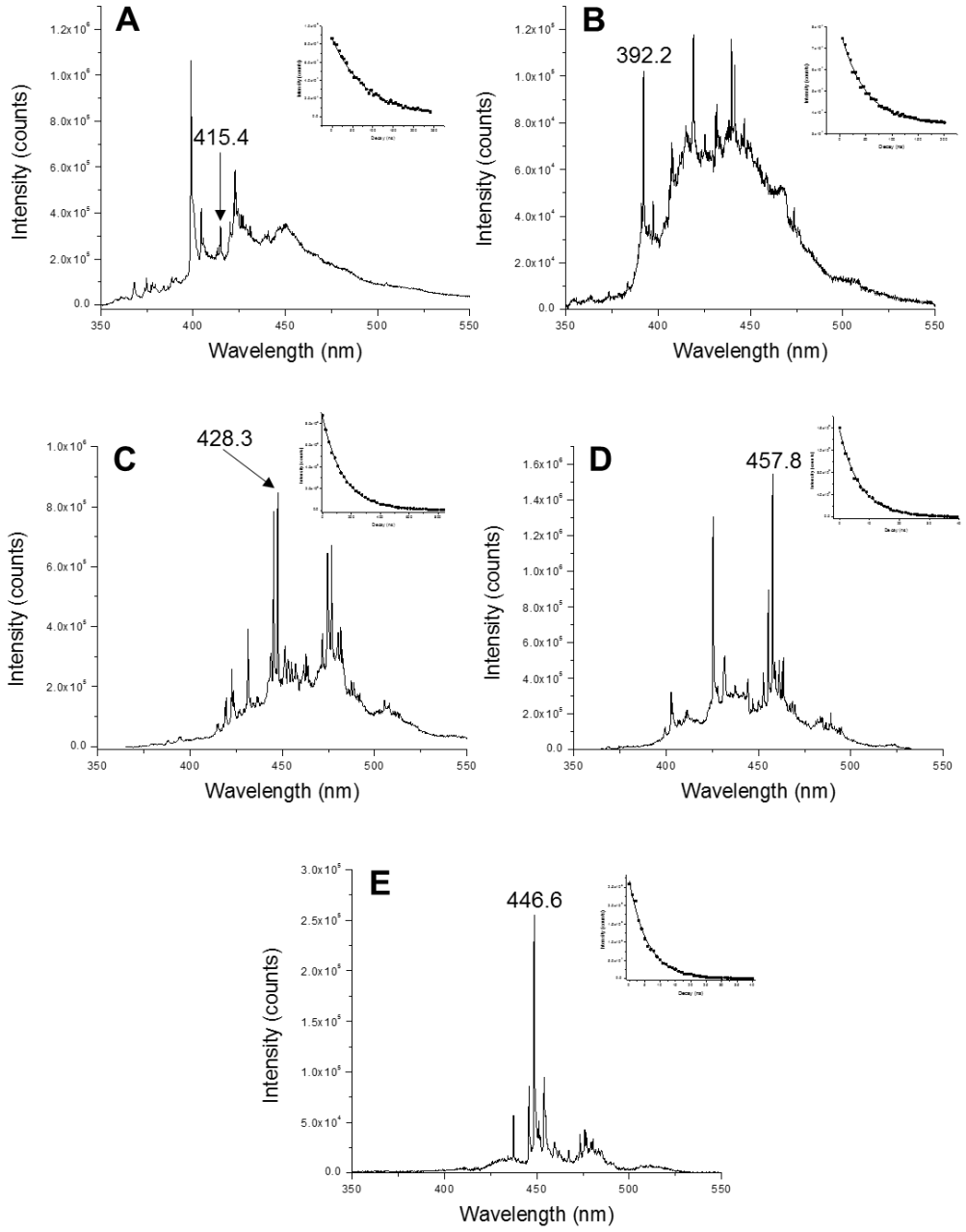

Figure 24. 4.2 K LETRSS fluorescence spectra of the HPLC fractions obtained from the SRM 1597a. In each spectrum, the target HMW-PAH isomer and experimental parameters were the following: (A) DB[*a*,*l*]P in n-octane (λ_{exc} = 318.0 nm, λ_{em} = 415.4 nm, 0 ns delay and 250 ns gate time); (B) DB[*a*,*e*]P in n-octane (λ_{exc} = 306.4 nm, λ_{em} = 392.4 nm, 10 ns delay and 150 ns gate time); (C) DB[*a*,*i*]P in n-decane (λ_{exc} = 312.0 nm, λ_{em} = 428.3 nm, 10 ns delay and 650 ns gate time); (D) N[*2*,*3*-*a*]P in n-decane (λ_{exc} = 317.0 nm, λ_{em} = 457.8 nm, 0 ns delay and 25 ns gate time) and (E) DB[*a*,*h*]P in n-decane (λ_{exc} = 310.0 nm, λ_{em} = 446.6 nm, 0 ns delay and 15 ns gate time). All spectra correspond to the accumulation of 100 laser pulses. The spectrograph slit was 42 μm.

Table 9. Lifetime analysis[a] of 5 HMW-PAH isomers

HMW-PAH	Standard [b]	SRM 1597a [c,e]	t-test [d]
DB[*a*,l]P	78.1 ± 1.03	80.4 ± 2.73	0.37
DB[*a*,*e*]P	54.3 ± 1.39	51.4 ± 0.64	2.34
DB[*a*,*i*]P	212. ± 7.20	200. ± 5.17	2.29
N[*2*,*3*-*a*]P	6.83 ± 0.05	7.13 ± 0.23	2.23
DB[*a*,*h*]P	6.31 ± 0.09	6.14 ± 0.10	0.81

[a] The fluorescence lifetime corresponds to the average of three individual measurements taken from three frozen aliquots at the maximum fluorescence wavelength.
[b] Lifetime recorded from a PAH standard solution prepared in the optimum n-alkane solvent.
[c] Lifetime recorded from the PAH in the HPLC fraction of the coal tar sample extracted with the optimum n-alkane solvent.
[d] t-test of PAH lifetimes from HPLC fraction compared to standard values. $t_{critical} = 2.78$ ($\alpha = 0.05$; $N = 6$)
[e] see appendix G for PAHs fluorescence decays.

3.4. Conclusion

Chemical analysis of PAHs with MM 302 is of great environmental and toxicological importance. Many of them are highly suspect as etiological agents in human cancer. Because their carcinogenic properties differ significantly from isomer to isomer, it is of paramount importance to determine the most toxic isomers even if they are present at much lower concentrations than their less toxic isomers. The main problems that confront HPLC and GC/MS arise from the large number of HMW-PAH isomers with very similar elution times and similar, possibly even virtually identical, mass fragmentation patterns. The approach presented here is based on HPLC-SPNE-LETRSS analysis. The spectral and lifetime information obtained with LETRSS provide the required selectivity for the unambiguous determination of PAH isomers in the HPLC fractions. Prior to LETRSS analysis, HPLC fractions are pre-concentrated via SPNE, an environmentally friendly extraction procedure based on the adsorption of PAHs on the surface of Au NPs [118-127]. Complete SPNE-LETRSS analysis is possible with microliters of HPLC fractions and organic solvent. The excellent analytical figures of merit associated to its non-destructive nature, which provides ample opportunity for further analysis with other instrumental methods makes this approach an attractive alternative for the analysis of isomers of HMW-PAHs in complex environmental samples.

CHAPTER 4. ROOM TEMPERATURE FLUORESCENCE SPECTROSCOPY OF BENZO[*a*]PYRENE METABOLITES ON OCTADECYL EXTRACTION MEMBRANES

4.1. Introduction

Considerable efforts have been made to improve luminescence measurements of compounds adsorbed on solid substrates [131, 132]. As a result, solid surface luminescence analysis is a widely accepted tool in environmental, pharmaceutical, food and agricultural science [133]. Particularly attractive is the use of SPE membranes for the on-site analysis of polycyclic aromatic compounds in water samples [134-138]. Attractive features include a simple experimental procedure and compatibility with portable instrumentation. Due to the non-destructive nature of luminescence measurements, extraction membranes can be brought to the lab for subsequent sample elution and fluorophore confirmation via high-resolution techniques [139-142].

Solid surface room temperature fluorescence (RTF) spectroscopy on solid phase extraction (SPE) membranes was first proposed for the analysis of polycyclic aromatic hydrocarbons (PAHs) in water samples [135, 143]. Octadecyl silica membranes were cut into tabs and subsequently immersed into aqueous solution for PAHs extraction. Depending on the PAH, the extraction step varied from one to two hours of immersion time. After drying for 5 min, the tabs were examined via front surface room-temperature fluorescence spectroscopy to reach LODs at the parts-per-billion (ng mL^{-1}) level [135, 143]. Later reports from Campiglia and co-workers extended the use of SPE membranes to the room temperature phosphorimetry (RTP) analysis of PAHs [136, 144-146], polychlorinated biphenyls [145, 147] and polychlorinated dibenzofurans[148].

Bulky glassware and vacuum pumps, common to classic SPE lab procedures, were replaced with a syringe kit well-suited for manual extraction under field conditions. A rapid air-drying step, which was accomplished by applying positive pressure to the syringe, removed the excess of water from the extraction membrane prior to spectroscopic measurements. Total analysis time took less than 10min per sample and provided LODs at the parts-per-billion ($pg.mL^{-1}$) concentration level.The same extraction procedure was later applied to the water analysis of PAHs via SPE-RTF [147].

This chapter focuses on the urine analysis of PAH metabolites via SPE-RTF. Although chromatographic techniques provide reliable results for the analysis of PAH metabolites [163-171], the development of easy-to-use and cost effective techniques with high sample throughput is relevant to assess PAHs uptake by large populations [167]. Previous articles on the urine analysis of PAH metabolites targeted monohydroxy-PAHs (OH-PAHs) [161,162]. Signal reproducibility was improved with the aid of a sample holder specifically designed for the manual optimization of luminescence signals. Background correction of solid substrates was carried out with the aid of Asymmetric Least Squares (ALS), a smoothing algorithm originally devised for baseline correction of chromatographic data [150] and often applied to matrix interference in chromatographic analysis [151,152]. 2-hydroxy-fluorene (2OH-FLU), 1-hydroxypyrene (1OH-PYR), 3-hydroxy-benzo[a]pyrene (3OH-B[a]P) and 9-hydroxy-phenanthrene (9OH-PHE) were determined in synthetic urine samples at the parts-per-trillion concentration level [161]. Recovery values varied from 99.0 ± 1.2% (3OH-B[a]P) to 99.9 ± 0.05% (1OH-PYR). The sample holder improved the precision of measurements with relative standard deviations (RSD) varying from 3.5% (2OH-FLU) to 9.5% (9OH-PHE). The application of ALS to SPE-RTF improved the LODs by

approximately two orders of magnitude. With only 10 mL of urine sample, the LODs of OH-PAHs varied from 57 pg mL^{-1} (2OH-FLU) to 2 pg mL^{-1}(1OH-PYR).

Herein, the application of SPE-RTF is extended to the urine analysis of benzo[*a*]pyrene-*trans*-9,10-dihydrodiol (B[*a*]P-diol), benzo[a]pyrene-r-7,t-8,c-9-tetrahydrotriol (B[*a*]P-triol) and benzo[*a*]pyrene-*r*-7,*t*-8,*c*-9,*c*-10-tetrahydrotetrol (B[*a*]P-tetrol). RTF measurements from extraction membranes are carried out with the aid of fiber optic probe that eliminates the need for manual optimization of signal intensities. RSDs varying from 2.07% (B[*a*]P-triol) to 8.55% (3-OH B[*a*]P) were obtained with a straightforward procedure. ALS background correction provided LODs at the pg.mL^{-1} range. Analytical recoveries from human urine samples varied from 87.54 ± 3.11% (3OH-B[*a*]P) to 99.77 ± 2.48% (B[*a*]P-tetrol). The excellent analytical figures of merit and the simplicity of the experimental procedure demonstrate the potential of SPE-RTF for screening biomarkers of PAH exposure in numerous urine samples.

4.2. Experimental

4.2.1. Chemicals and Materials

All solvents were Aldrich HPLC grade. All chemicals were analytical-reagent grade and utilized without further purification. Unless otherwise noted, Nanopure water was used throughout. B[*a*]P-diol, B[*a*]P-triol and B[*a*]P-tetrol were purchased from Sigma–Aldrich. 3OH-B[*a*]P was from Midwest Research Institute. All other chemicals were purchased from Fisher Chemical. The Sep-Pak C-18 membranes were purchased from Varian/Agilent. The synthetic urine solution was manufactured by RICCA Chemical Company (Arlington, TX) and purchased from Fischer Scientific. Its chemical composition mimicked main components of human urine at

the concentrations found in healthy urine samples. Human urine samples obtained from an anonymous volunteer group of healthy non-smoking individuals were pooled, frozen and stored at 4 °C until further analysis.

4.2.2. Preparation of stock solution of B[a]P metabolites

Stock solutions of B[*a*]P metabolites (100 µg/mL) were prepared by dissolving 1.0 mg of standard in 10 mL of methanol. All stock solutions were kept in the dark at 4 ^{o}C. Prior to use, stock solutions were monitored via RTF spectroscopy for possible photo-degradation of metabolites. Spectral profiles and fluorescence intensities of stock solutions remained the same for a period of six months. Working solutions of B[*a*]P metabolites were prepared daily by serial dilution of stock solutions.

4.2.3. Hydrolysis of urine samples

Urine samples (8 mL) were spiked with 1 mL of metabolite stock solution of appropriate concentration and equilibrated for 30 min to allow for the interaction of B[*a*]P metabolites with urine components such as urea and various salts. Then 500 µL of 0.1 M HCl was added to the sample and the mixture was buffered with 500 µL of 0.05 M potassium biphthalate sodium hydroxide buffer (pH 5.0). The buffered sample was shaken for 30 min at 1400 rpm to allow for urine hydrolysis. [161, 162]

4.2.4. SPE with octadecyl membranes

A cork borer with an inside diameter of 8 mm was used to dissect a 47 mm C18 membrane into 8 mm extraction disks. An 8 mm disk was loaded into a stainless steel filter syringe kit (Alltech) and connected to a 10 mL Hamilton syringe (see Figure 13B). Positive pressure was used to force all liquid solutions through the disk. Prior to sample application, the extraction membrane was conditioned with 5 mL of methanol and 5 mL of water.

Optimization of experimental parameters concerning the retention of B[*a*]P metabolites on extraction membranes led to the following procedure: aqueous metabolite solutions or synthetic urine samples were processed through extraction membranes previously conditioned with 5 mL methanol and 5 mL water. Following sample extraction, each membrane was sequentially rinsed with 5 mL of water and 5 mL of 1% ammonium hydroxide. Void water was mechanically removed from the membrane with a 100 mL syringe forcing three 100 mL volumes of air through the disk.

4.2.5. RTF measurements

The FOP used for these studies was described in the previous chapters of this dissertation. Fluorescence measurements were carried out with a FluoroMax-3 (Horiba Jobin Yvon, Edison, NJ) equipped with a 450 W xenon arc source. The 1200 grooves/mm gratings in the single excitation and emission monochromators were blazed at 330 and 500 nm, respectively. Their reciprocal linear dispersion was equal to 4.25 nm/ mm. The uncooled photomultiplier tube (Hamamatsu, Model R928) detector was operated in the photon- counting mode. Commercial software (DataMax, version 2.20, Horiba Jobin Yvon) was used for automated scanning and fluorescence data acquisition. The excitation fiber and the emission bundle of the FOP were coupled to the sample compartment of the spectrofluorimeter with the aid of a commercial fiber optic mount (F-3000, Horiba Jobin Yvon) that optimized collection efficiency via two concave mirrors (see Figure 25). Position alignment of each end of the FOP with the respective focusing mirror was facilitated using commercially available adapters (Horiba Jobin Yvon).

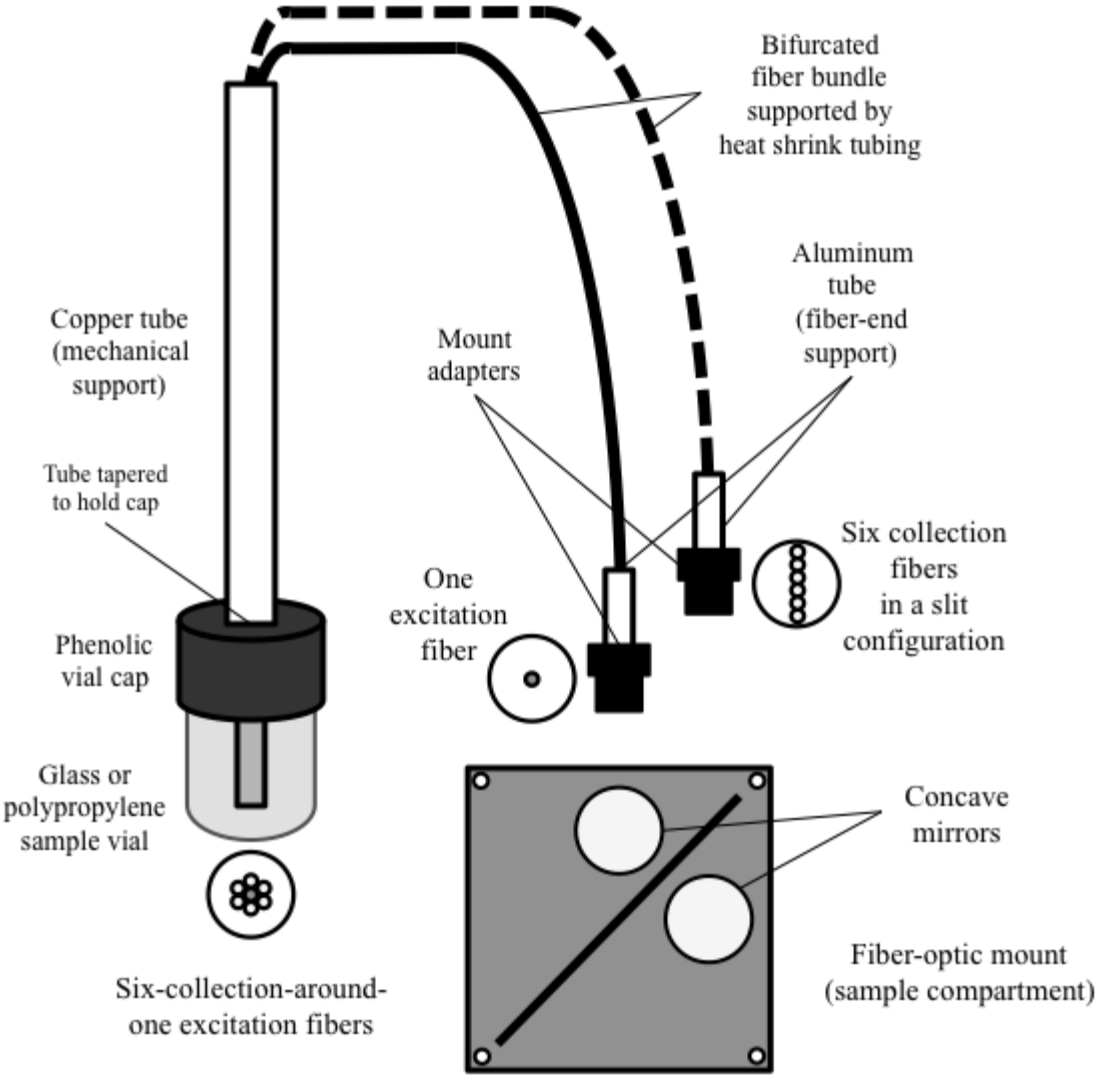

Figure 25 Schematic diagrams of the fiber optic probe and the fiber optic mount used for room-temperature fluorescence measurements.

4.2.6. ALS Software

Routines for data pre-treatment and processing were written in MATLAB [153]. Baseline routines for emission background correction were adapted from routines previously described in the literature for baseline correction of chromatographic data [154]. Implementation of the ALS algorithm included a smoothing parameter equal to 1×10^7, an asymmetry parameter equal to 0.001, an order of differences in penalty equal to 3 and a single regularization parameter, whose value was 1.

4.3. Results and Discussion

During the past decades, considerable efforts have been made to develop bio-analytical assays for the determination of PAH metabolites in physiological fluids. Depending on the complexity of the sample and the relative concentrations of the targeted metabolites, a combination of preparation techniques is often necessary to reach the limits of detection of the instrumental method of analysis.[56-59] Analysis of metabolites has been accomplished via HPLC, capillary electrophoresis (CE) and GC. Ultraviolet –visible absorption and room temperature fluorescence detection have been widely used with both HPLC and CE [60-65]. The ultimate specificity belongs to high-resolution MS either coupled to gas chromatography (GC-MS) or HPLC (HPLC-MS).[52-54, 66-68].

The molecular structures of the metabolites chosen for this study are shown in Figure 26. These four compounds provide an example of the rich and heterogeneous distribution of metabolic products B[a]P produce. B[a]P is the most toxic PAH in the EPA priority pollutants list and it is often used as a measure of risk. A summary of the analytical approaches developed for their determination in urine samples is presented in Table 10. Our literature search revealed no reports on the analysis of B[*a*]P-triol in urine samples. Examination of Table 10 shows a wide range of SPE recoveries for the studied metabolites. SPE procedures often elute B[*a*]P metabolites with milliliter volumes of methanol, which are then evaporated to micro-litters (or even dryness) for sample pre-concentration. These steps are prone to metabolite loss and poor analytical recoveries.

Table 10 Analytical figures of merit reported for B[*a*]P metabolites analysis in urine samples by different analytical methods

Metabolites	LOD (ng L^{-1})	Recovery %	Sample preparation	Instrumental method	Analysis time (min)[a]	Reference
3-OH B[*a*]P	1615	40	SPE, evaporation	HPLC	40	169
3-OH B[*a*]P	40	48	SPE, evaporation	HPLC	45	170
3-OH B[*a*]P	44	68	SPE, evaporation	HPLC	41	171
3-OH B[*a*]P		80	SPE, evaporation	LC-MS/MS	7	166
B[*a*]P-diol		79	SPE, evaporation	HPLC	70	167[b]
B[*a*]P-diol		90	SPE, evaporation	Spectrofluorometric detection		172
B[*a*]P-diol	70		LLE[a], evaporation, HPLC fraction ,derivatization	GC-MS	45	168[b]
B[*a*]P-tetrol	10	34	SPE, evaporation, HPLC fraction	Fluorescence spectroscopy		173
B[*a*]P-tetrol	50		SPE, evaporation	HPLC	14	163
B[*a*]P-tetrol		44	SPE, evaporation	GC-MS/MS	14	164
B[*a*]P-tetrol			SPE, evaporation, HPLC fraction, derivatization	GC-MS/MS	15	165

[a] instrumental analysis only; does not include sample preparation procedures
[b] in rat urine
[b] LCC= liquid –liquid extraction

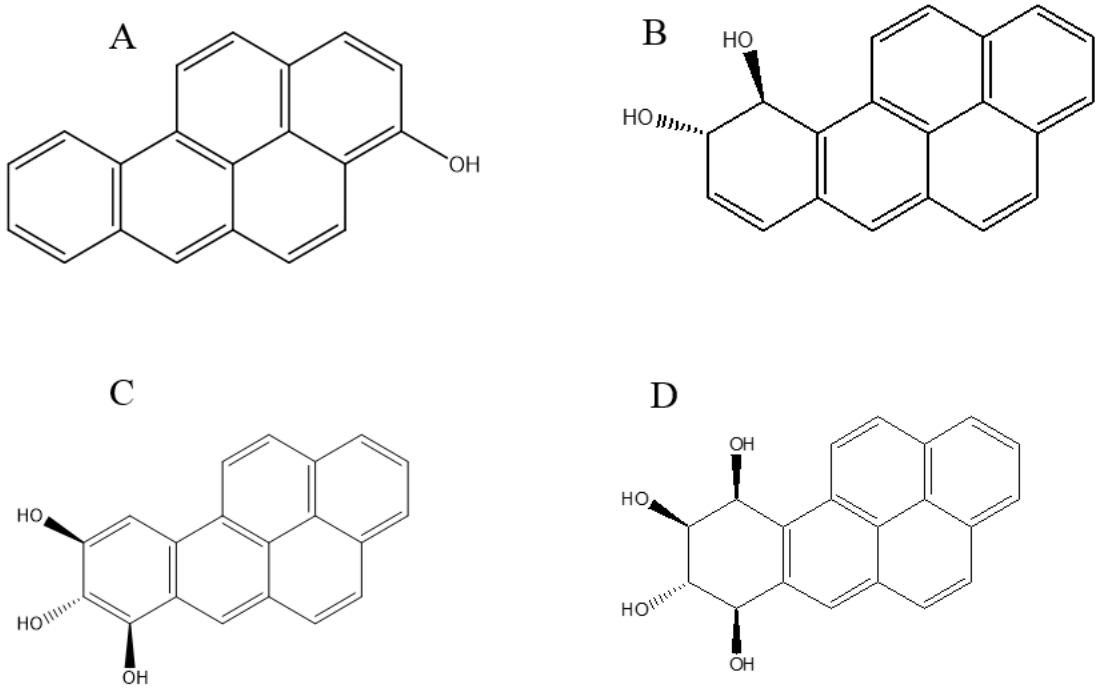

Figure 26. Molecular structures of (A) 3-hydroxy-benzo[a]pyrene (B) benzo[*a*]pyrene-*trans*-9,10-dihydrodiol (C) benzo[*a*]pyrene-r-7,t-8,c-9-tetrahydrotriol and (D) benzo[*a*]pyrene-*r*-7,*t*-8,*c*-9,*c*-10-tetrahydrotetrol

4.3.1. RTF analytical figures of merit (AFOM) of B[a]P metabolites in aqueous solutions

Figure 27 shows the initial survey of room-temperature excitation and fluorescence spectra of B[*a*]P metabolites in methanol/water (10% v/v) solutions. All measurements were made from standard (1 × 1 cm) quartz cuvettes filled with undegassed solutions. All spectra were collected at 90◦ from the excitation beam using 3 nm excitation and emission band-pass. No attempts were made to adjust slit widths for optimum spectral resolution, nor were the spectra corrected for instrumental response. The 3 nm band-pass provided signal-to-blank ratios higher than 3 for all the studied metabolites at the trace concentration level. No significant changes were observed from spectra of B[*a*]P metabolites in hydrolyzed urine samples or adsorbed on extraction membranes.

Table 11 summarizes the RTF AFOM of the studied metabolites. All measurements were made at the maximum excitation and fluorescence wavelengths of each compound. Each calibration curve was built with a minimum of four B[*a*]P metabolites concentrations. For each concentration plotted in the calibration graph, the RTF intensity was the average of three determinations taken from three sample aliquots (N = 3). No efforts were made to experimentally obtain the upper concentration limit of the calibration curve. The correlation coefficients of the calibration curves were close to unity, indicating a linear relationship between metabolite concentration and signal intensity. The linearity was also evaluated by an ANOVA test as suggested by IUPAC [160] with satisfactory results. The LOD were calculated using the equation LOD = 3 ×SB/m, were S_B is the standard deviation of 16 blank determinations and m is the slope of the calibration curve. The limits of quantitation (LOQ) were calculated with the formula LOQ = 10 × SB/m. The slopes of the calibration curves were obtained with the least squares method.

The strong fluorescence intensity resulting from the rigid and delocalized $\boldsymbol{\pi}$ -electron system of B[*a*]P metabolites provides LOD and LOQ values at the ng mL^{-1} concentration level.

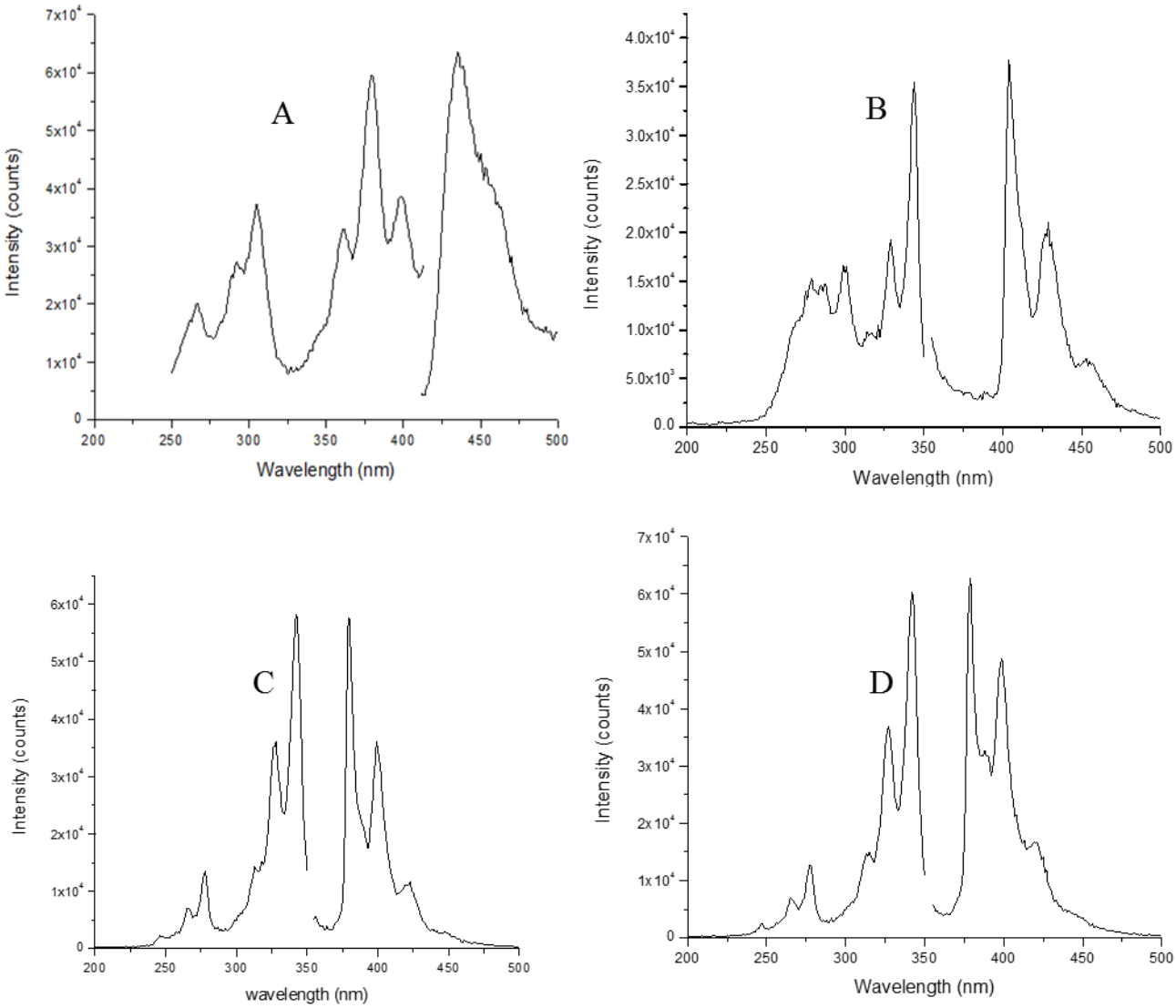

Figure 27. Room-temperature excitation and fluorescence spectra of (A) 20ng.mL^{-1} 3-hydroxy-benzo[a]pyrene, (B) 20ng.mL^{-1} benzo[*a*]pyrene-*trans*-9,10-dihydrodiol, (C) 20ng.mL^{-1} benzo[a]pyrene-r-7,t-8,c-9-tetrahydrotriol and (D) 20ng.mL^{-1} benzo[*a*]pyrene-*r*-7,*t*-8,*c*-9,*c*-10-tetrahydrotetrol recorded from pure standard solutions prepared in 10% methanol/water

Table 11 RTF Analytical figures of Merit in 10% methanol/water solutions

B[*a*]P metabolite	λexc/λem[a] (nm)	LDR[b] (ng mL^{-1})	R^{2c}	RSD[d]	LOD[e] (ng mL^{-1})
3-OH B[*a*]P	380/435	3.73-40	0.9902	4.5	1.22
B[*a*]P-diol	344/404	2.40-40	0.9918	1.02	0.72
B[*a*]P-triol	343.5/379	1.06-40	0.9975	1.69	0.32
B[*a*]P-tetrol	344/379	0.97-40	0.9979	2.02	0.29

[a] Excitation and emission wavelengths.

[b] LDR = linear dynamic range extending from the limit of quantification (LOQ) to an arbitrarily chosen upper linear concentration. LOQ defined as 3.3 × LOD.

[c] Correlation coefficient of calibration curve.

[d] RSD = relative standard deviation in %. Calculated as RSD = $[S_{av}/X_{av}]*100$; where S_{av} is the standard deviation and X_{av} is the average intensity of three independent measurements from three aliquots.

[e] Limit of detection in calculated as $3\times S_B/m$, where S_B is the standard deviation of 16 blank measurements and m is the slope of the calibration curve.

4.3.2. Extraction efficiency of SPE membranes

The percentages of extraction (%E) were calculated with the formula %E = ($I_{BE} - I_{AE}$ / I_{BE}) x100, where I_{BE} and I_{AE} refer to the fluorescence signals before and after extraction, respectively. In all cases, the volume of extracted sample was 10mL. The mass of extracted metabolite did not surpass the nominal breakthrough mass (30mg) of extraction membranes. Table 12 compares %E values obtained from standard solutions to those from hydrolyzed urine samples. All values are the averages of three aliquots submitted to the entire extraction procedure. Within a confidence interval of 95% (N=3), all %E are equivalent to 100%. This fact excludes the possibility of matrix interference on the retention of B[*a*]P metabolites. Similar results were obtained with other B[*a*]P metabolites concentrations within the LDR of Table 11. Keeping in mind that metabolite elution is not required for the determination of B[*a*]P metabolites via SPE-RTF, the %E values in Table 12 correspond to the analytical recovery of the method. As shown in Table 13 the %E values obtained from standard solutions are statistically the same as those obtained from urine samples. This is an indication that the chemical compositions of synthetic and human urine samples do not interfere with the retention of B[a]P metabolites on extraction membranes.

.

Table 12 Percentage of metabolite retention on C-18 membranes from aqueous solutions, synthetic urine and human urine samples

B[*a*]P metabolite	From Aqueous solution	synthetic urine	Human urine
3-OH B[*a*]P	87.54 ± 3.11	90.31 ± 2.79	82.11 ± 4.91
B[*a*]P-diol	99.15 ± 3.14	97.76 ± 2.78	93.93 ± 3.53
B[*a*]P-triol	98.65 ± 4.32	98.10 ± 2.17	92.43 ± 3.76
B[*a*]P-tetrol	99.77 ± 2.98	98.87 ± 3.01	91.89 ± 4.10

Table 13 Statistical comparison of %E values in Table 12

B[a]P metabolite	$t_{(expt)}$ H_2O/synthetic	$t_{(expt)}$ H_2O/human	$t_{(expt)}$ synthetic/human
3-OH B[*a*]P	0.469193	0.16714	0.927503
B[*a*]P-diol	0.233704	0.285553	0.582858
B[*a*]P-triol	0.071291	0.228799	0.836501
B[*a*]P-tetrol	0.155645	0.338096	0.922704

* $t_{critical}$ =2.78; P = 95%, N_1 = 3; N_2 = 3.

4.3.3 AFOM of B[a]p metabolites via SPE-RTF

The SPE-RTF AFOMs of the four studied metabolites are summarized in Table 14. SPE was carried out with 10mL of standards prepared in 10% methanol/water (v/v). For each concentration plotted in the calibration graph, the RTF intensity was the average of at least three determinations taken from three extraction disks (N = 9). The LDR were obtained with a minimum of five B[*a*]P metabolites concentrations. No efforts were made to experimentally obtain the upper concentration limits of the calibration curves. It is important to note, however, that the highest concentration plotted in each calibration curve did not surpass the breakdown volume of the SPE device [146]. The correlation coefficients of the calibration curves and the slopes of the log-log plots (data not shown) were close to unity, indicating a linear relationship between B[*a*]P metabolite concentration and fluorescence intensity. Satisfactory results were also obtained by the ANOVA test suggested by IUPAC [160]. The RSD at medium linear concentrations were lower than 10%. The LOD were estimated at the parts-per-billion to sub-parts-per-billion concentration levels. Their comparison to the LOD values in Table 11 shows no advantage of pre-concentrating the sample prior to RTF. Table 15 compares the slopes of the calibration curves, blank intensities and their standard deviations from aqueous solutions to those obtained on extraction membranes. The calibration graphs are shown in Figure 28 and Figure 29. Sample pre- concentration via SPE provides 10-fold improvements on the slopes of the calibration curves. The main reason for the lack of LOD improvements is the higher intensities of blank signals and their respective standard deviations on extraction membranes. Better SPE-RTF LOD could have been obtained by extracting 100mL volumes of standard solutions, i.e. an alternative with little appealing in the screening context of human urine samples.

Table 14 SPE-RTF AFOM of B[*a*]P metabolites

B[*a*]P metabolite	$\lambda_{exc}/\lambda_{em}$ [a]	LDR [b] (ng mL^{-1})	R^2 [c]	LOD [d] (ng mL^{-1})
3-OH-B[*a*]P	381/425	9.91-40	0.9746	2.97
B[*a*]P-diol	345/405	2.78-40	0.9935	0.84
B[*a*]P-triol	345/380	4.23-40	0.9981	1.27
B[*a*]P-tetrol	345/375	2.91-40	0.9967	0.87

[a] Excitation and emission wavelengths.

[b] LDR = linear dynamic range extending from the limit of quantification (LOQ) to an arbitrarily chosen upper linear concentration. LOQ defined as 3.3 x LOD.

[c] Correlation coefficient of calibration curve.

[d] Limit of detection calculated as $3xS_B$ / m; where S_B is the standard deviation of 6 blank measurements and m is the slope of the calibration curve.

Table 15 Slope and blank signals obtained from calibration curves in Table 14

B[*a*]P metabolites	Slope [a]		Average blank intensity ± standard deviation [b] (cps)	
	H_2O ($x10^3$)	Membrane ($x10^4$)	H_2O ($x10^3$)	Membrane ($x\ 10^4$)
3-OH B[*a*]P	3.88	2.33	8.50 ± 0.63	6.15 ± 0.48
B[*a*]P-diol	2.04	8.50	1.32 ± 0.23	5.52 ± 0.25
B[*a*]P-triol	2.60	8.10	2.15 ± 0.28	7.35 ± 0.18
B[*a*]P-tetrol	2.83	8.21	2.27 ± 0.29	7.34 ± 0.21

[a] Slope of linear dynamic range obtained via the least squares method.

[b] Average values based on three individual measurements recorded from the extraction membrane submitted to the entire procedure.

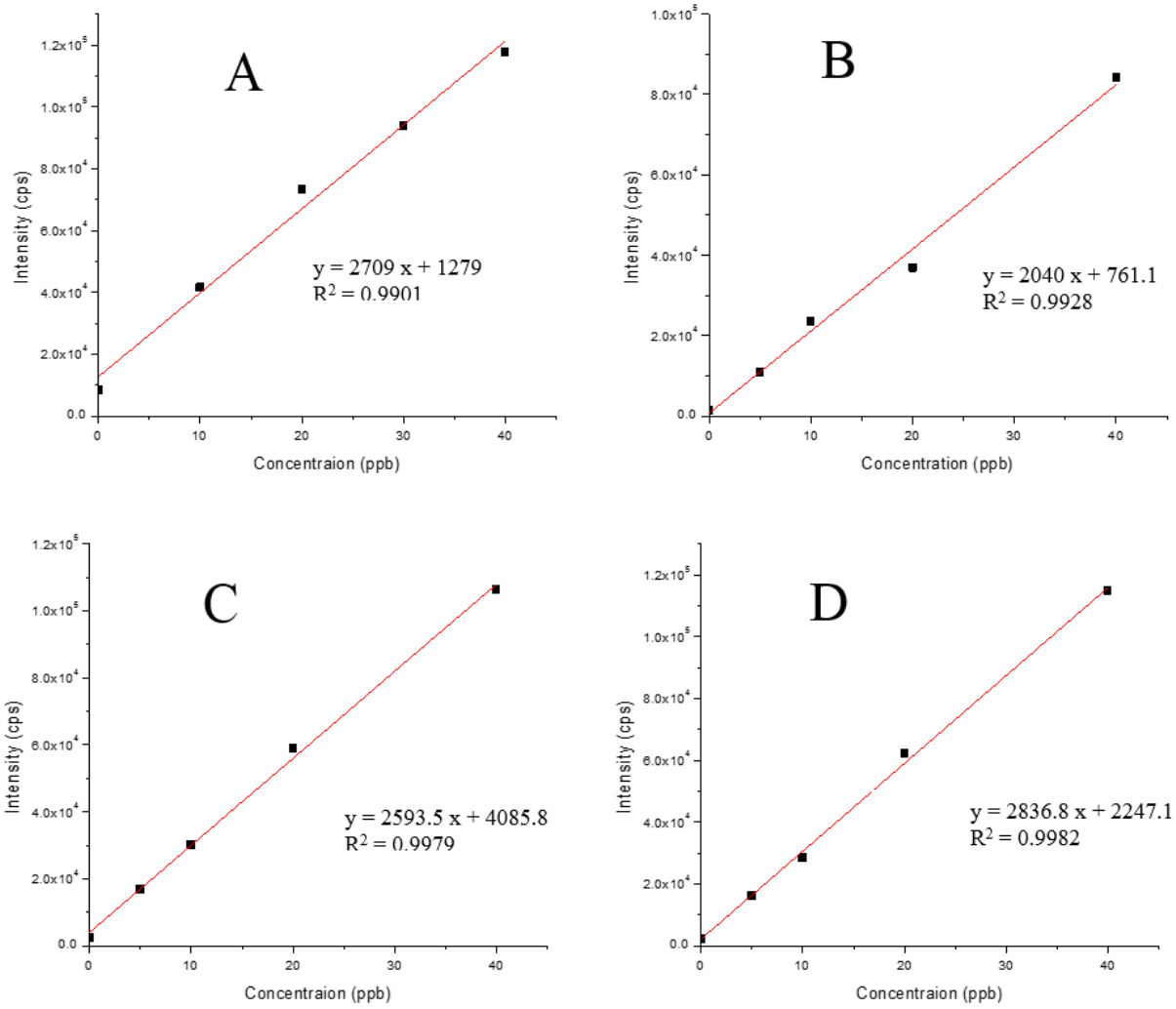

Figure 28. Calibration curve of (A) 3-hydroxy-benzo[*a*]pyrene, (B) benzo[*a*]pyrene-*trans*-9,10-dihydrodiol, (C) benzo[*a*]pyrene-r-7,t-8,c-9-tetrahydrotriol and (D) benzo[*a*]pyrene-*r*-7,*t*-8,*c*-9,*c*-10-tetrahydrotetrol recorded from pure standard solutions prepared in 10% methanol/water (v/v).

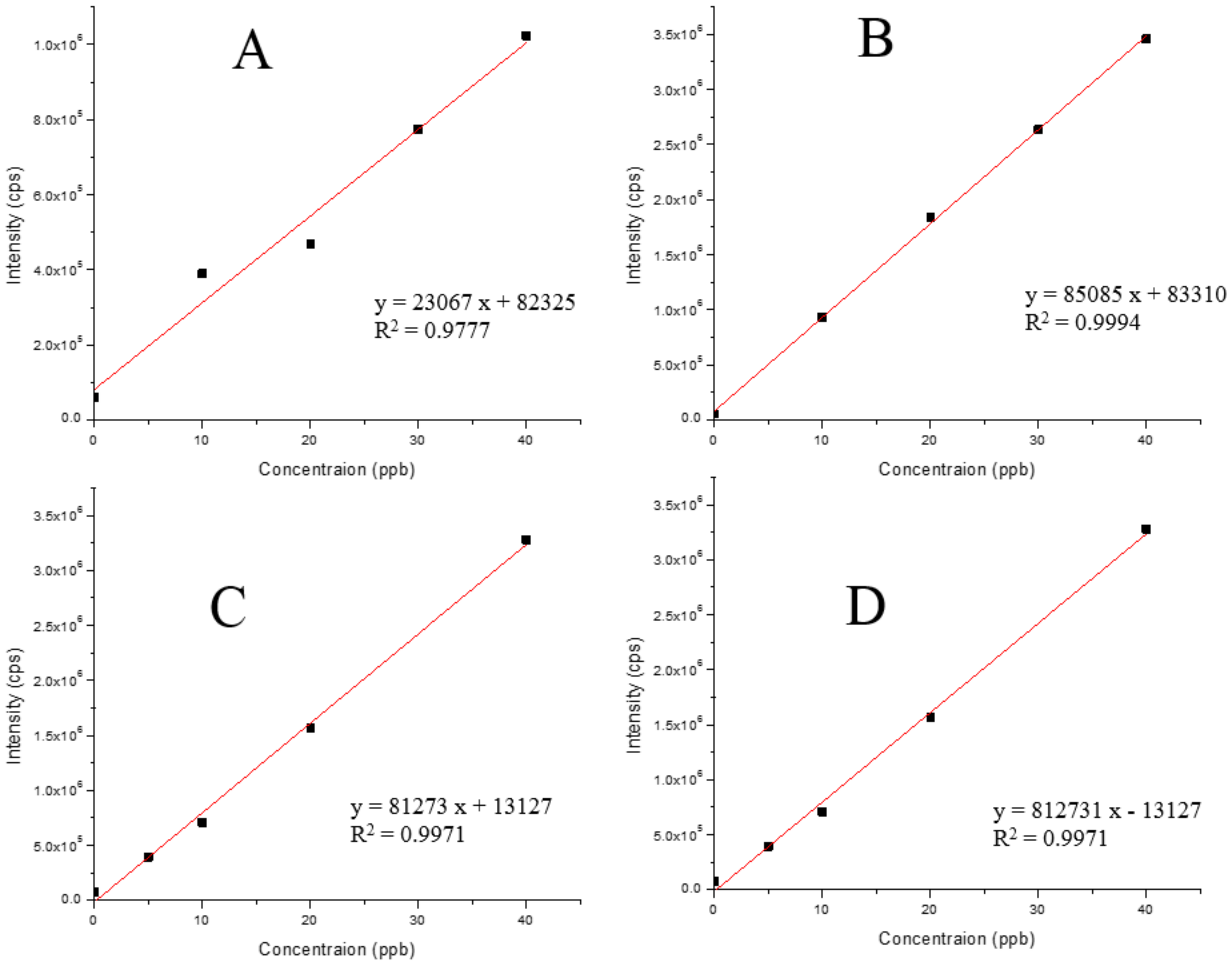

Figure 29. Calibration curve of (A) 3-hydroxy-benzo[*a*]pyrene, (B) benzo[*a*]pyrene-*trans*-9,10-dihydrodiol, (C) benzo[a]pyrene-r-7,t-8,c-9-tetrahydrotriol and (D) benzo[*a*]pyrene-*r*-7,*t*-8,*c*-9,*c*-10-tetrahydrotetrol recorded from extraction membranes.

4.3.4. Background correction via ALS

The ALS algorithm uses the Whittaker smoother for discrete (time) series, which minimizes the function[150]:

$$Q = \sum_i vi\ (yi - fi)^2 + p$$

Where *y* is the data (experimental signal), *f* a smooth trend (or baseline estimation), υ prior weights, and p the asymmetry parameter. The successful implementation of ALS to the background correction of extraction membranes was achieved with a smoothing parameter equal to 1 x 10^7, an asymmetry parameter equal to 0.001, an order of differences in penalty equal to 3 and a single regularization parameter. Figure 30 clearly shows the improvement that was obtained with the implementation of ALS. The background intensity (I_B) of extraction membranes was considerably reduced and so it was the standard deviation (S_B) of the average background signals. Table 16 summarizes the effect of ALS on the SPE-RTF AFOM of the studied metabolites. Comparison to Table 14 reveals LOD improvements ranging from 25x (B[*a*]P-triol) to 42x (B[*a*]P-diol). The LOD in Table 16 meet the expectations for the analysis of B[a]P metabolites in urine samples.

Table 16 SPE-RTF-ALS AFOM of B[*a*]P metabolites

PAH metabolite	$\lambda_{exc}/\lambda_{em}$ [a]	LDR [b] (ng mL^{-1})	R^2 [c]	LOD [d] (ng mL^{-1})
3-OH- B[*a*]P	381/425	0.37-40	0.9924	0.11
B[a]P-diol	345/405	0.10-40	0.9995	0.02
B[a]P-triol	345/380	0.16-40	0.9987	0.05
B[a]P-tetrol	345/375	0.11-40	0.9966	0.03

[a] Excitation and emission wavelengths.
[b] LDR = linear dynamic range extending from the limit of quantification (LOQ) to an arbitrarily chosen upper linear concentration. LOQ defined as 3.3 x LOD.
[c] Correlation coefficient of calibration curve.
[d] Limit of detection calculated as 3xSB / m; where SB is the standard deviation of 6 blank measurements and m is the slope of the calibration curve.

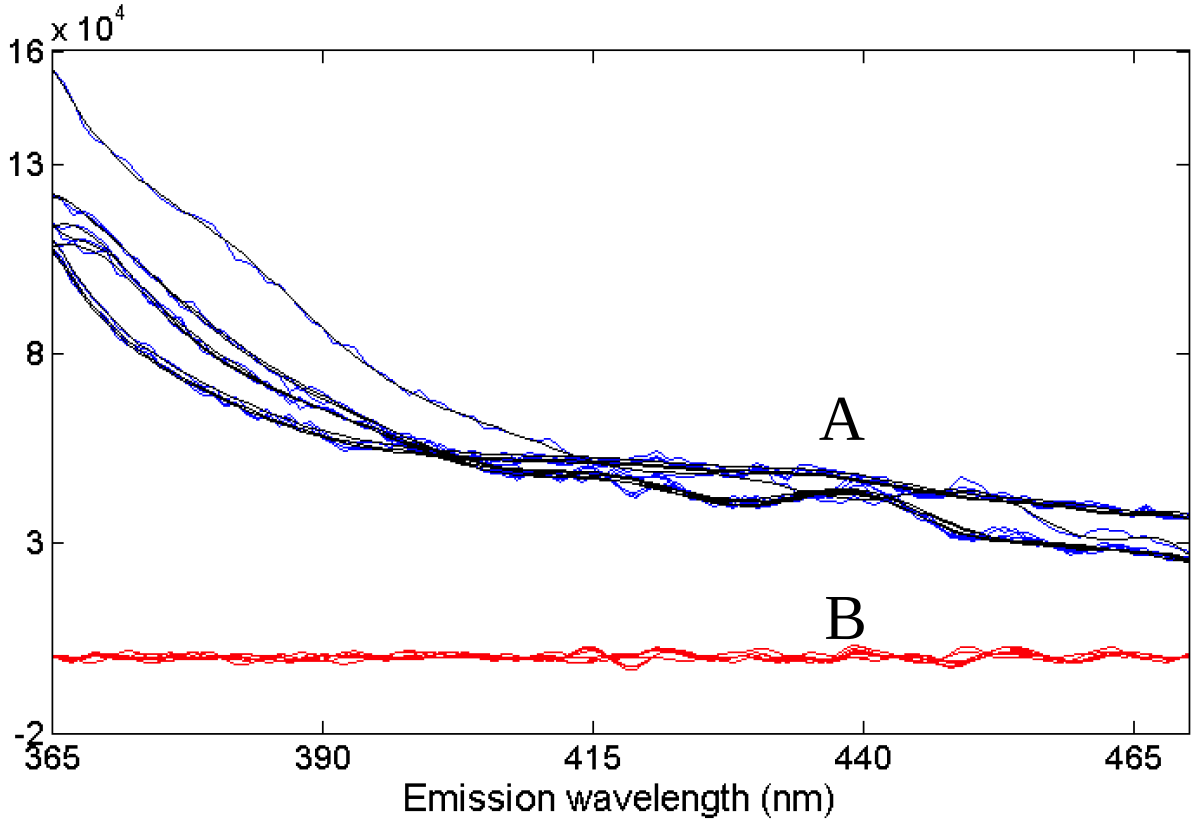

Figure 30. Blank signals (A) before and (B) after blank ALS background correction.

4.4. Conclusion

Several features make SPE-RTF spectroscopy a well-suited approach for screening B[*a*]P metabolites in urine samples. Its straightforward experimental procedure is attractive for routine analysis of numerous samples. The direct determination of B[*a*]P metabolites on the surface of the extraction membrane eliminates the need for subsequent elution steps and provides excellent (~ 100%) metabolite recoveries. Acceptable precision for analytical work is possible with the aid of FOP specifically designed for manual optimization of maximum fluorescence signals. Background correction of extraction membranes via ALS provides LOD at the parts-per- trillion concentration level. With 10mL of urine samples, the LOD varied from 20 $pg.mL^{-1}$ (B[*a*]P-tetrol) to 110 $pg.mL^{-1}$ (3-OH-Pyr). These values compare favorably to LOD previously reported via chromatographic methods [155-159].

CHAPTER 5. FUTURE WORK

That we can measure and analyse DB[*a,l*]P, DB[*a,i*]P, DB[*a,e*]P, N[*2,3-a*]P and DB[*a,h*]P in HPLC fractions of complex environmental extracts is no longer in question. But our ability to do the same with the other 18 commercially available isomers of MW 302 has not been demonstrated yet. Research in our lab will answer this question by removing the limitations that have plagued the analysis of HMW-PAHs for the past decades.

The proposed methodology is not restricted to a single MW and can be extended to significantly large structures in the future. The number of structural isomers increases rapidly with the number of condensed rings. This fact makes chromatographic analysis of organic pollutants with MW higher than 302 even more challenging. Future developments in this direction should have implications in environmental site characterization and remediation, health research, and fundamental laboratory studies.

APPENDIX A: RT FLUORESCENCE EXCITATION-EMISSION SPECTRA OF HMW-PAHS

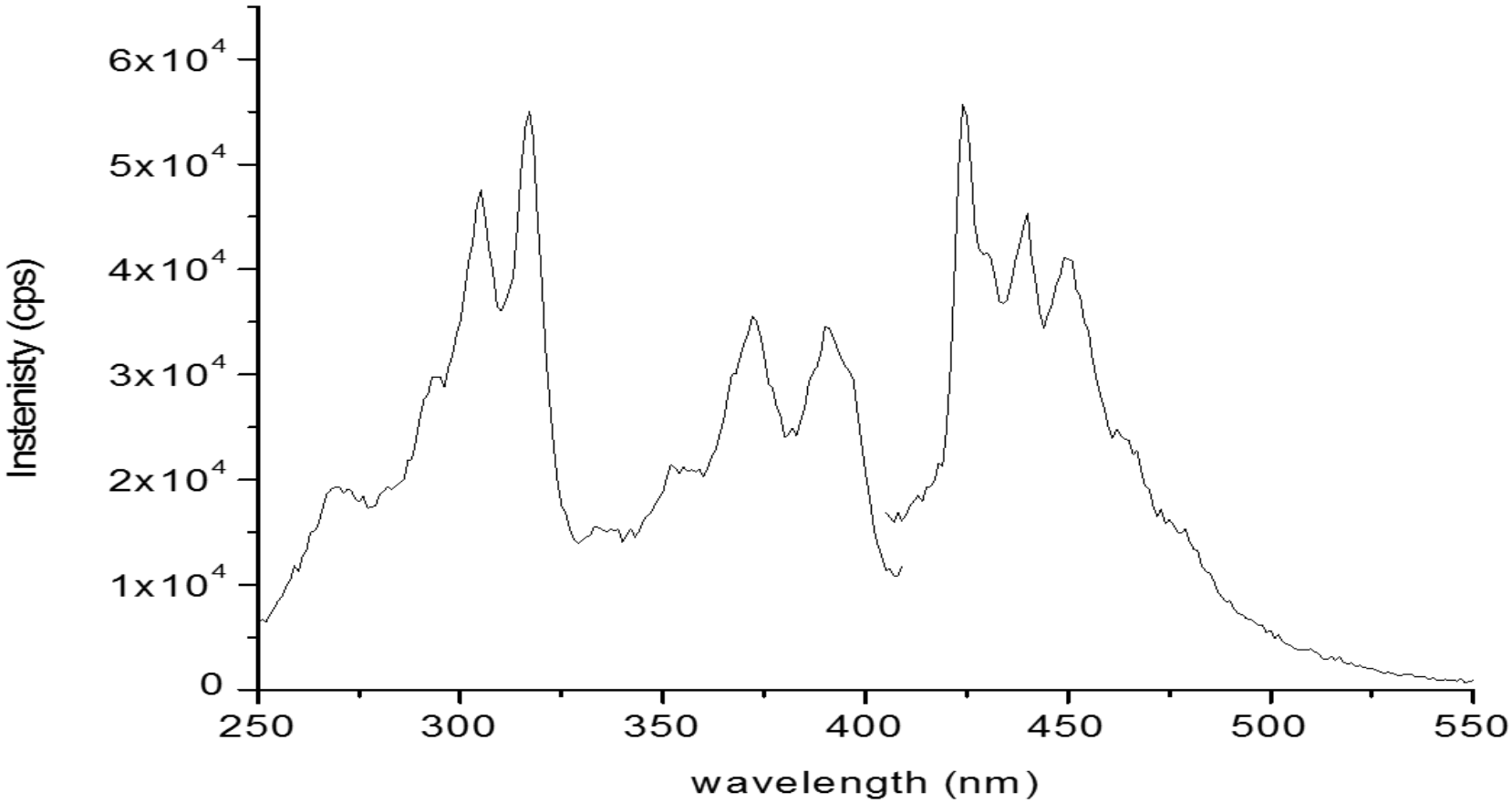

Figure A-1. Room temperature excitation-emission fluorescence spectra of 50 ng mL^{-1} DB[*a*,*l*]P standard were recorded in 100% acetonitrile. Excitation and emission bandpass was 3nm.

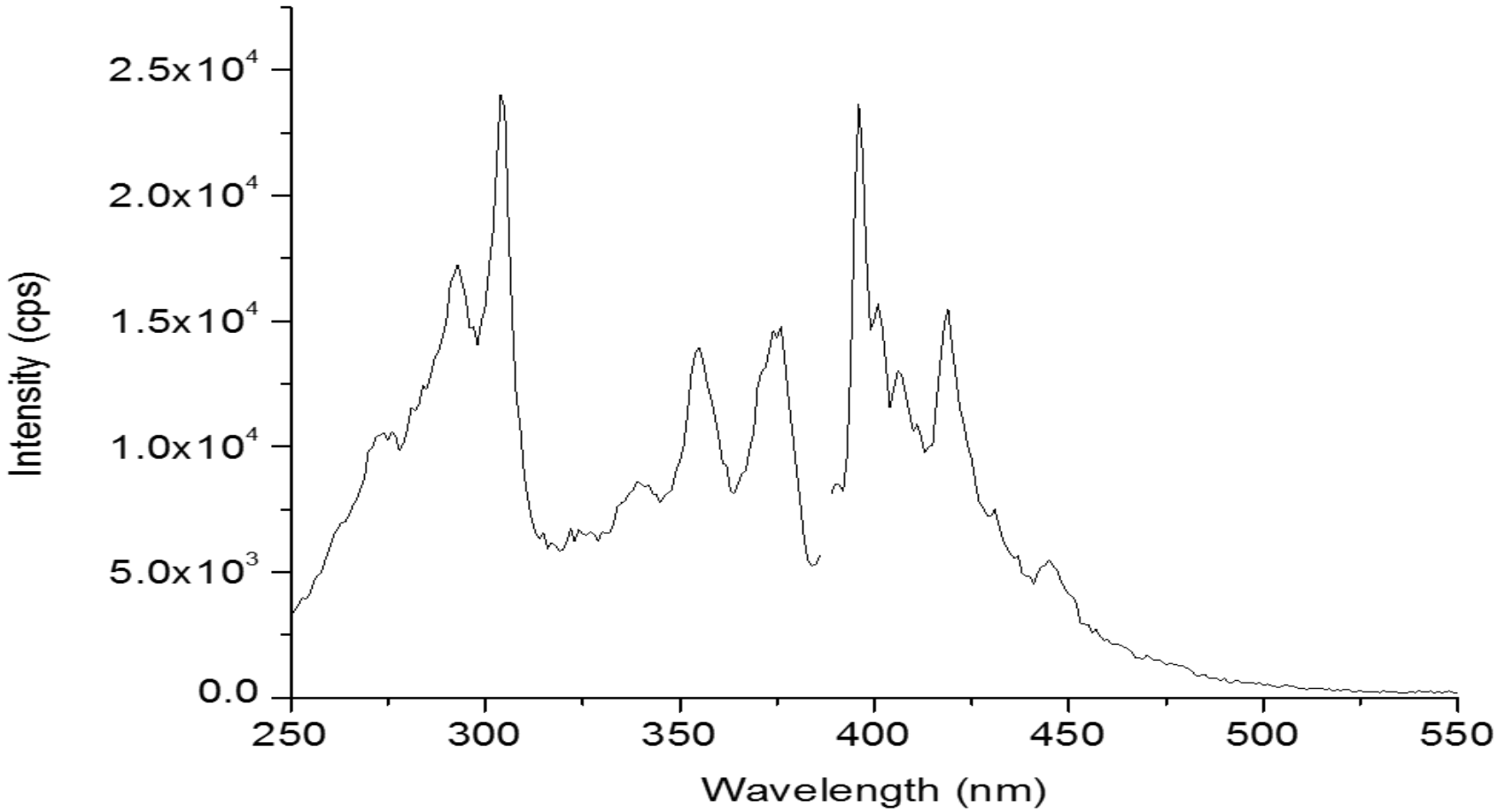

Figure A-2. Room temperature excitation-emission fluorescence spectra of 50 ng mL^{-1} DB[*a*,*e*]P standard were recorded in 100% acetonitrile. Excitation and emission bandpass was 3nm.

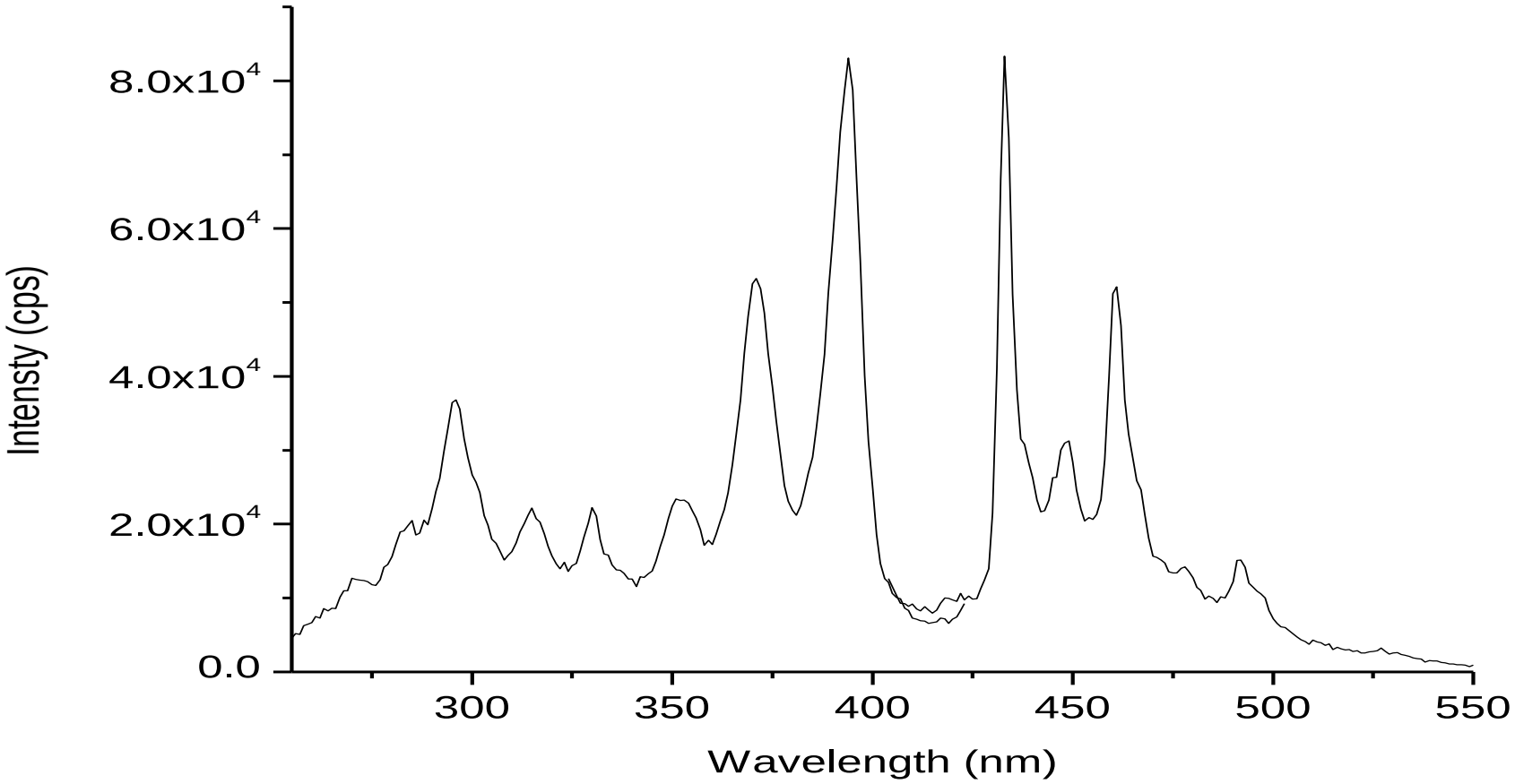

Figure A-3. Room temperature excitation-emission fluorescence spectra of 50 ng mL^{-1} DB[*a*,*i*]P standard were recorded in 100% acetonitrile. Excitation and emission bandpass was 3nm.

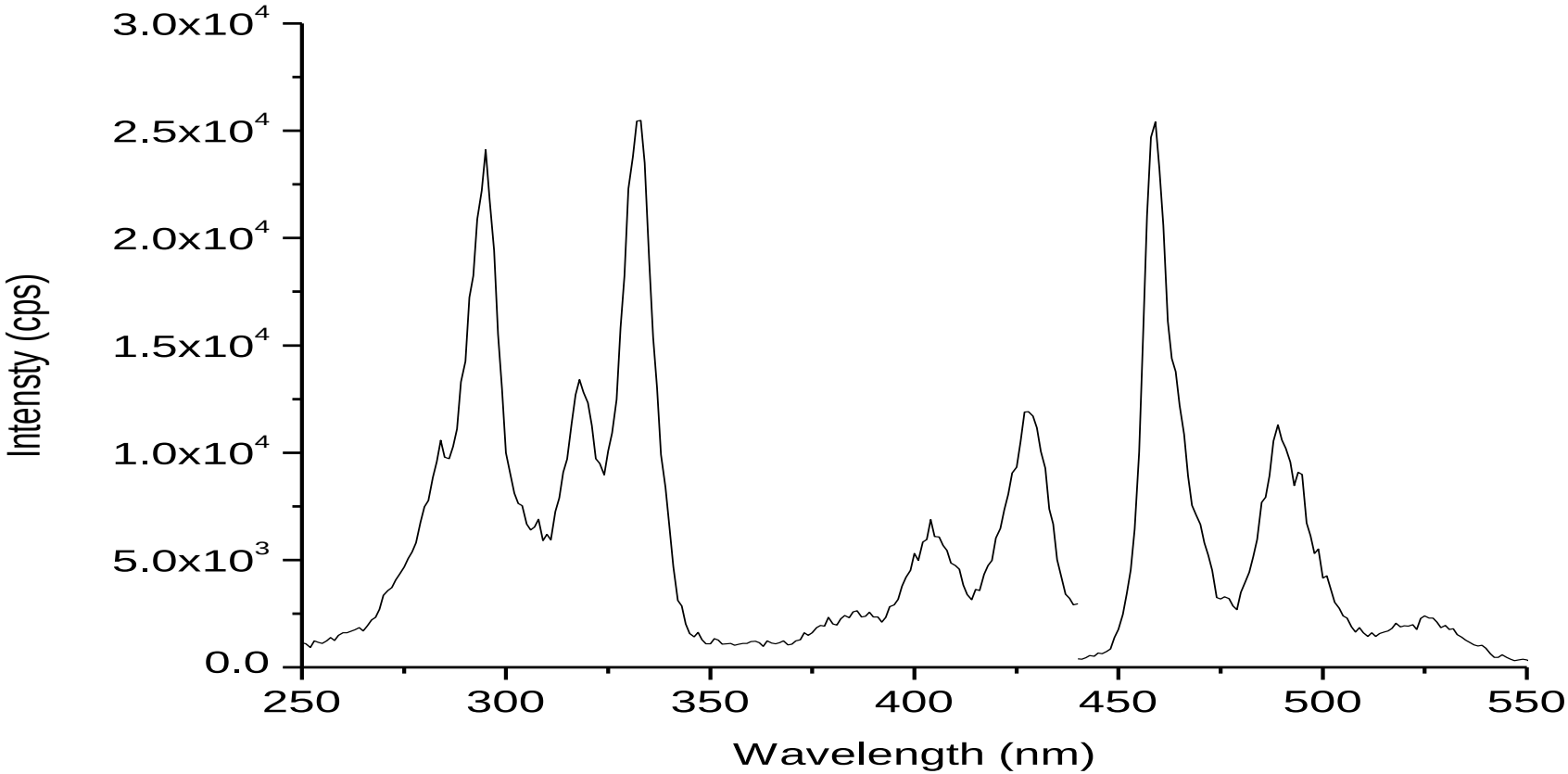

Figure A-4. Room temperature excitation-emission fluorescence spectra of 50 ng mL^{-1} N[*2,3-a*]P standard were recorded in 100% acetonitrile. Excitation and emission bandpass was 3nm.

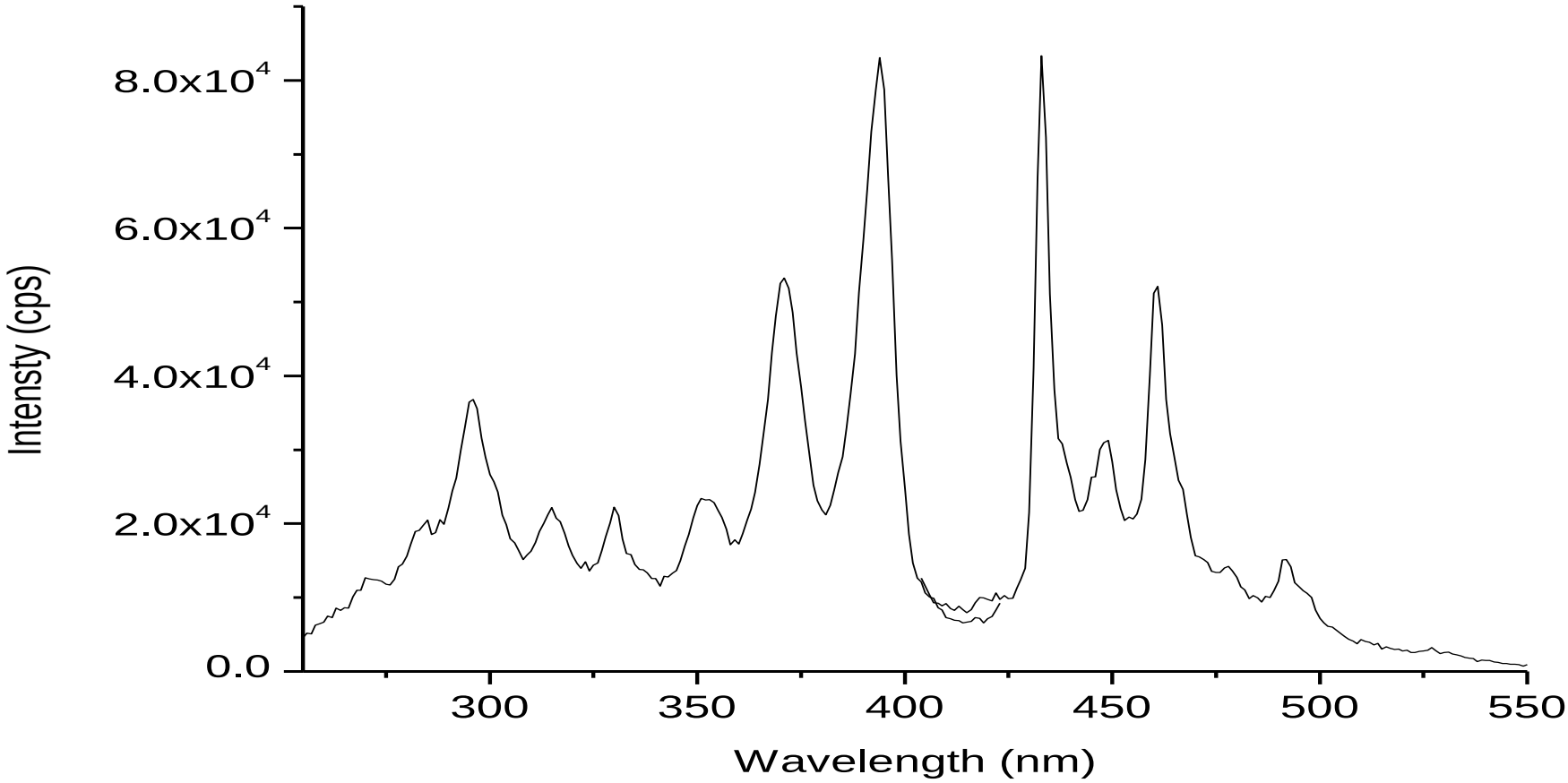

Figure A-5. Room temperature excitation-emission fluorescence spectra of 50 ng mL^{-1} DB[*a*,*h*]P standard were recorded in 100% acetonitrile. Excitation and emission bandpass was 3nm.

APPENDIX B: FLUORESCENCE EMISSION SPECTRA OF HMW-PAHS AT 4.2K

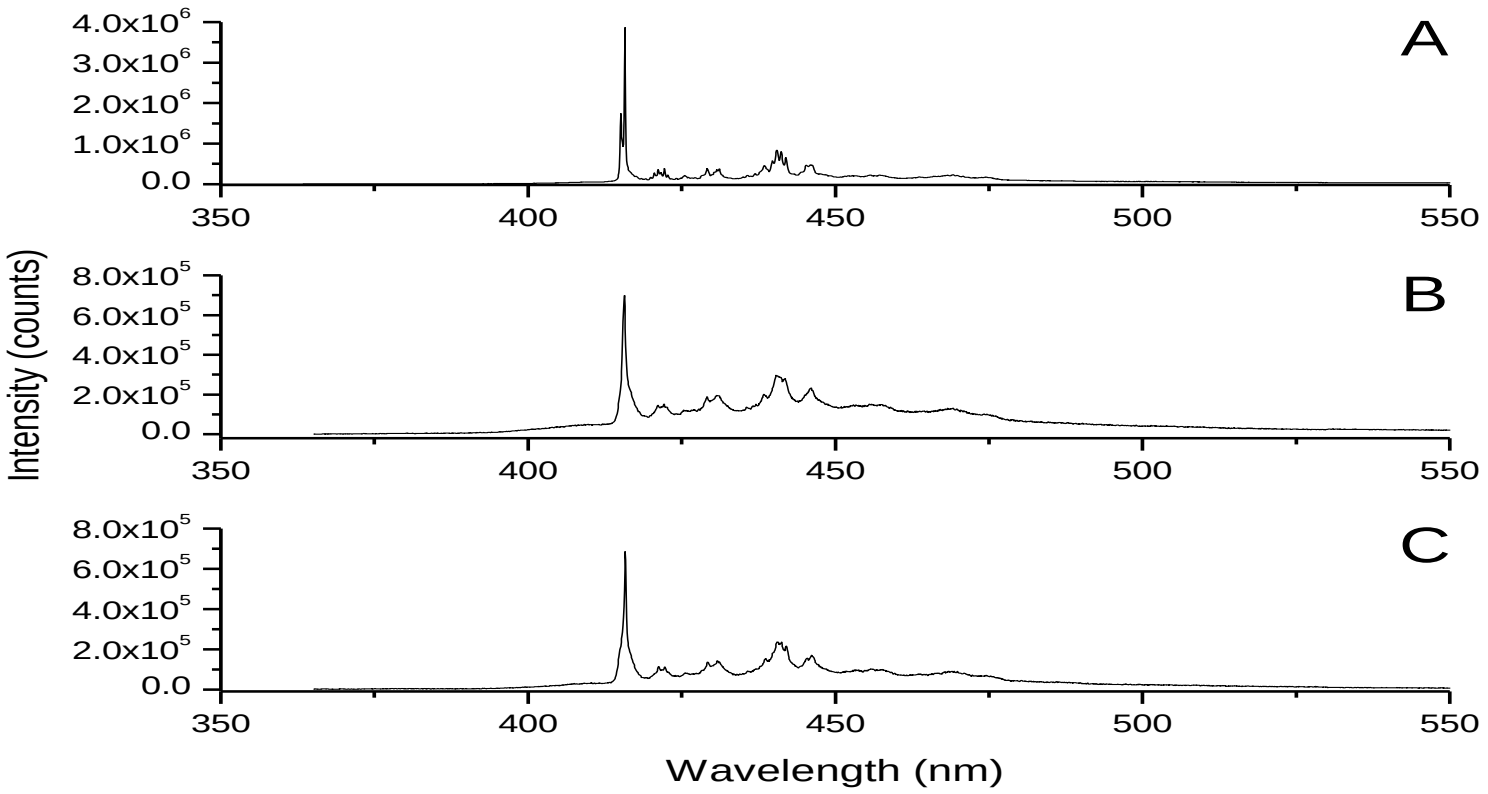

Figure B-1 4.2 K LETRSS fluorescence spectra of 100 ng mL^{-1} DB[*a,l*]P standard were recorded in (A) n-octane; λ_{ex} = 318.0 nm, (B) n-nonane; λ_{ex} = 318.0 and (C) n-decane; λ_{ex} = 318.0 nm using a 0 ns delay and 250 ns gate time. All spectra correspond to the accumulation of 100 laser pulses. The spectrograph slit was 42 μm.

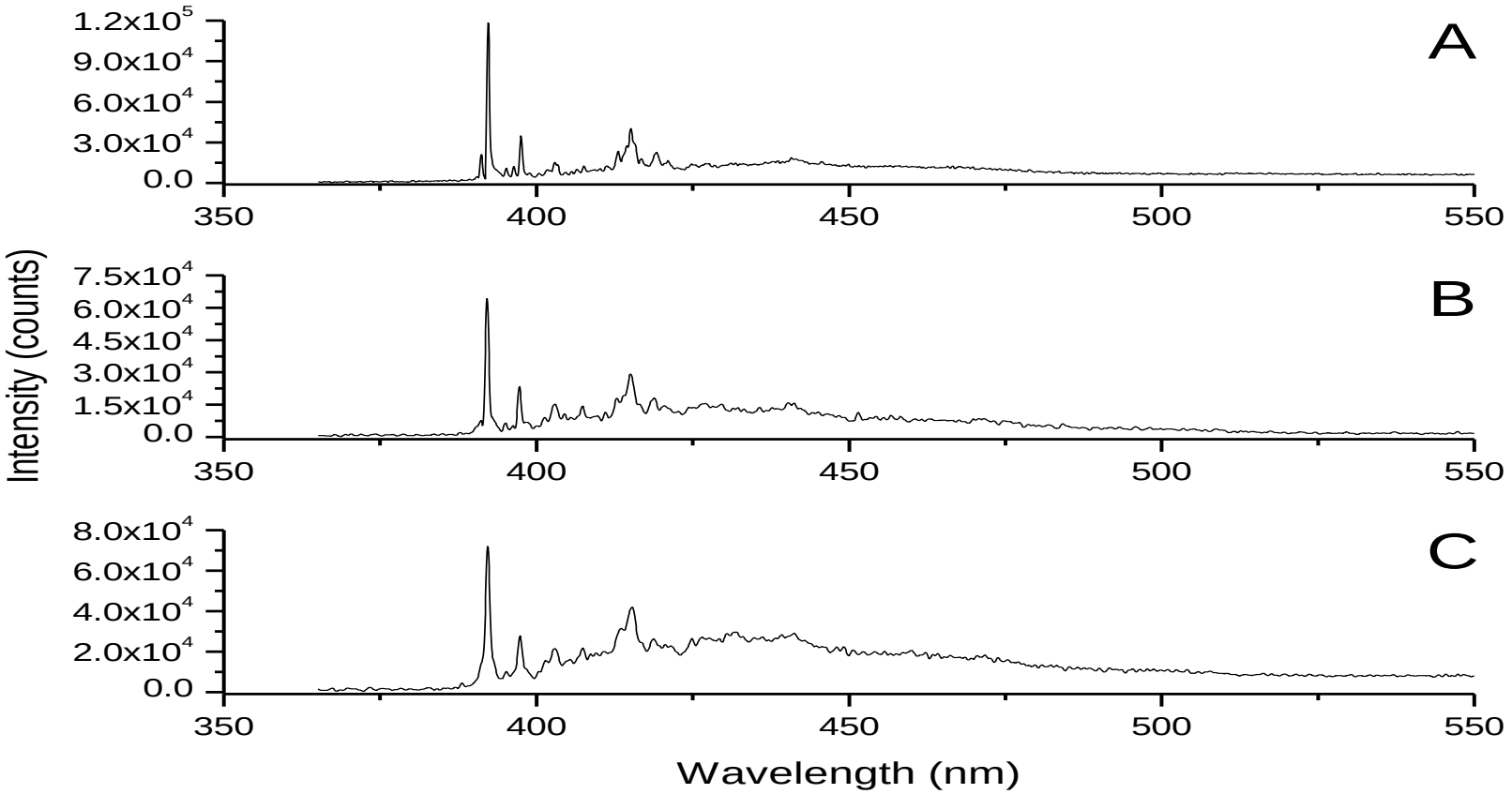

Figure B-2. 4.2 K LETRSS fluorescence spectra of 100 ng mL^{-1} DB[*a*,*e*]P standard were recorded in (A) n-octane; λ_{ex} = 306.4 nm, (B) n-nonane; λ_{ex} = 305.0 and (C) n-decane; λ_{ex} = 306.0 nm using a 10 ns delay and 150 ns gate time. All spectra correspond to the accumulation of 100 laser pulses. The spectrograph slit was 42 μm.

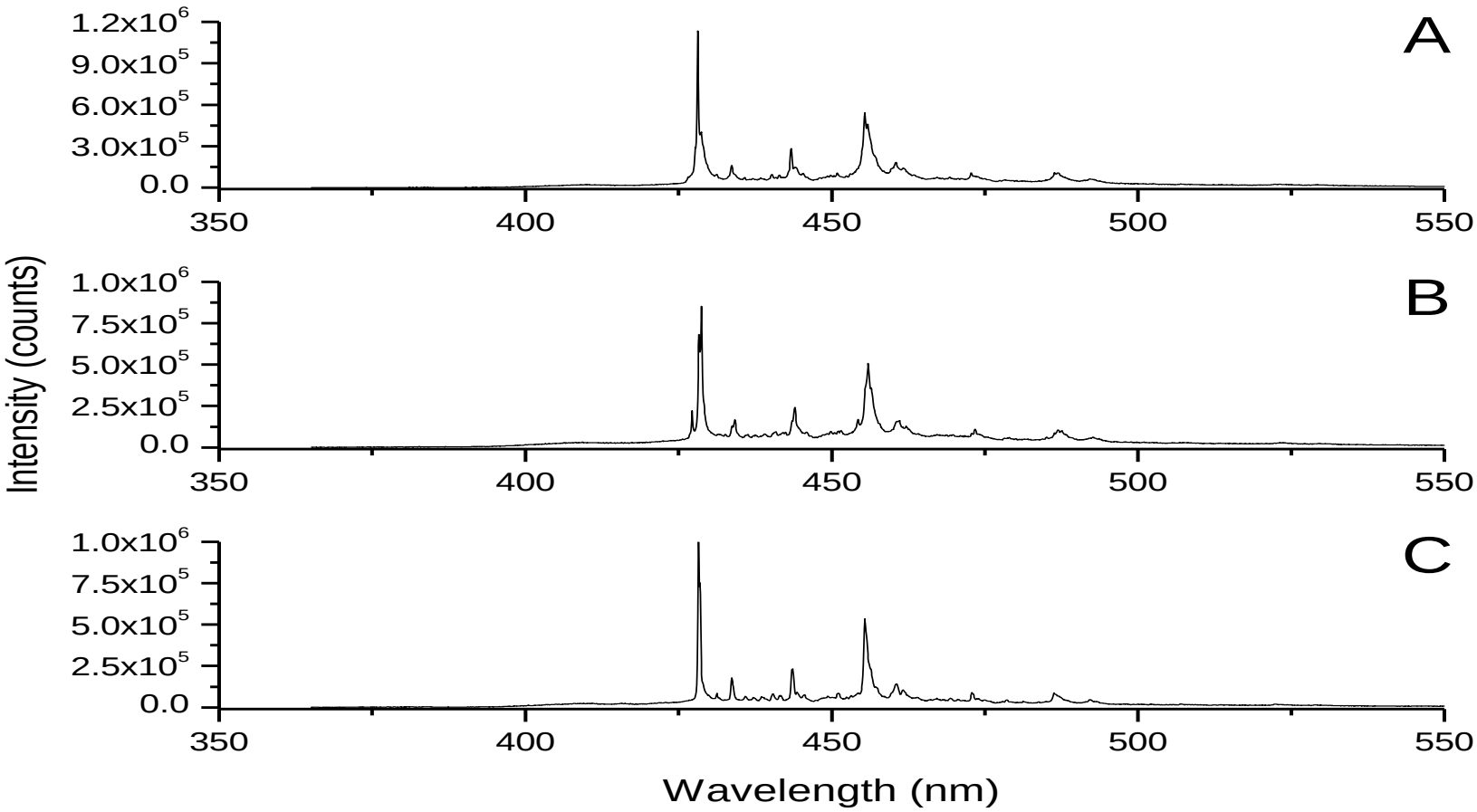

Figure B-3. 4.2 K LETRSS fluorescence spectra of 100 ng mL^{-1} DB[*a*,*i*]P standard were recorded in (A) n-octane; λ_{ex} = 312.0 nm, (B) n-nonane; λ_{ex} = 312.0 and (C) n-decane; λ_{ex} = 312.0 nm using a 10 ns delay and 650 ns gate time. All spectra correspond to the accumulation of 100 laser pulses. The spectrograph slit was 42 μm.

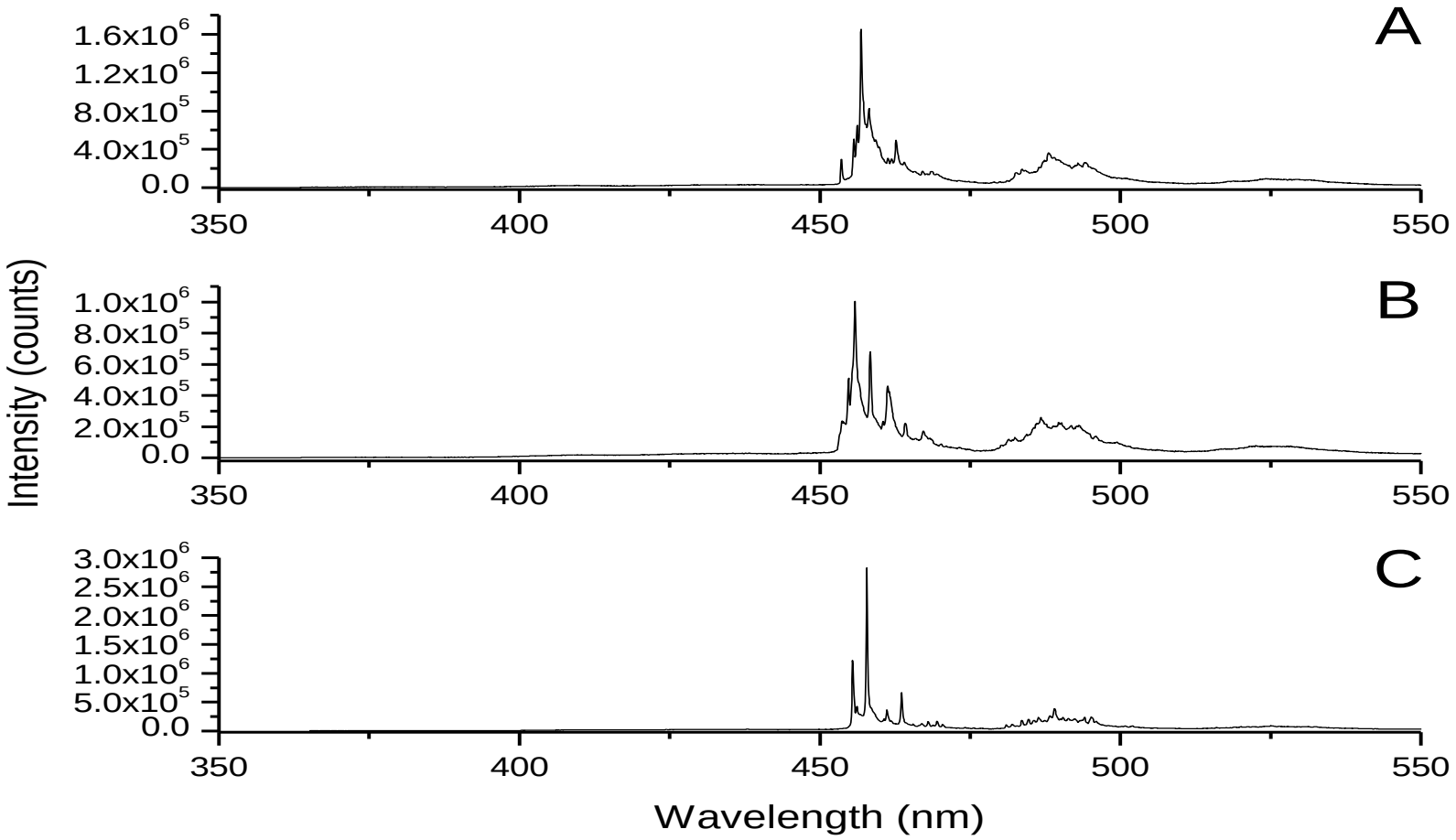

Figure B-4. 4.2 K LETRSS fluorescence spectra of 100 ng mL^{-1} N[*2,3-a*]P standard were recorded in (A) n-octane; λ_{ex} = 318.0 nm, (B) n-nonane; λ_{ex} = 317.0 and (C) n-decane; λ_{ex} = 317.0 nm using a 0 ns delay and 25 ns gate time. All spectra correspond to the accumulation of 100 laser pulses. The spectrograph slit was 42 μm.

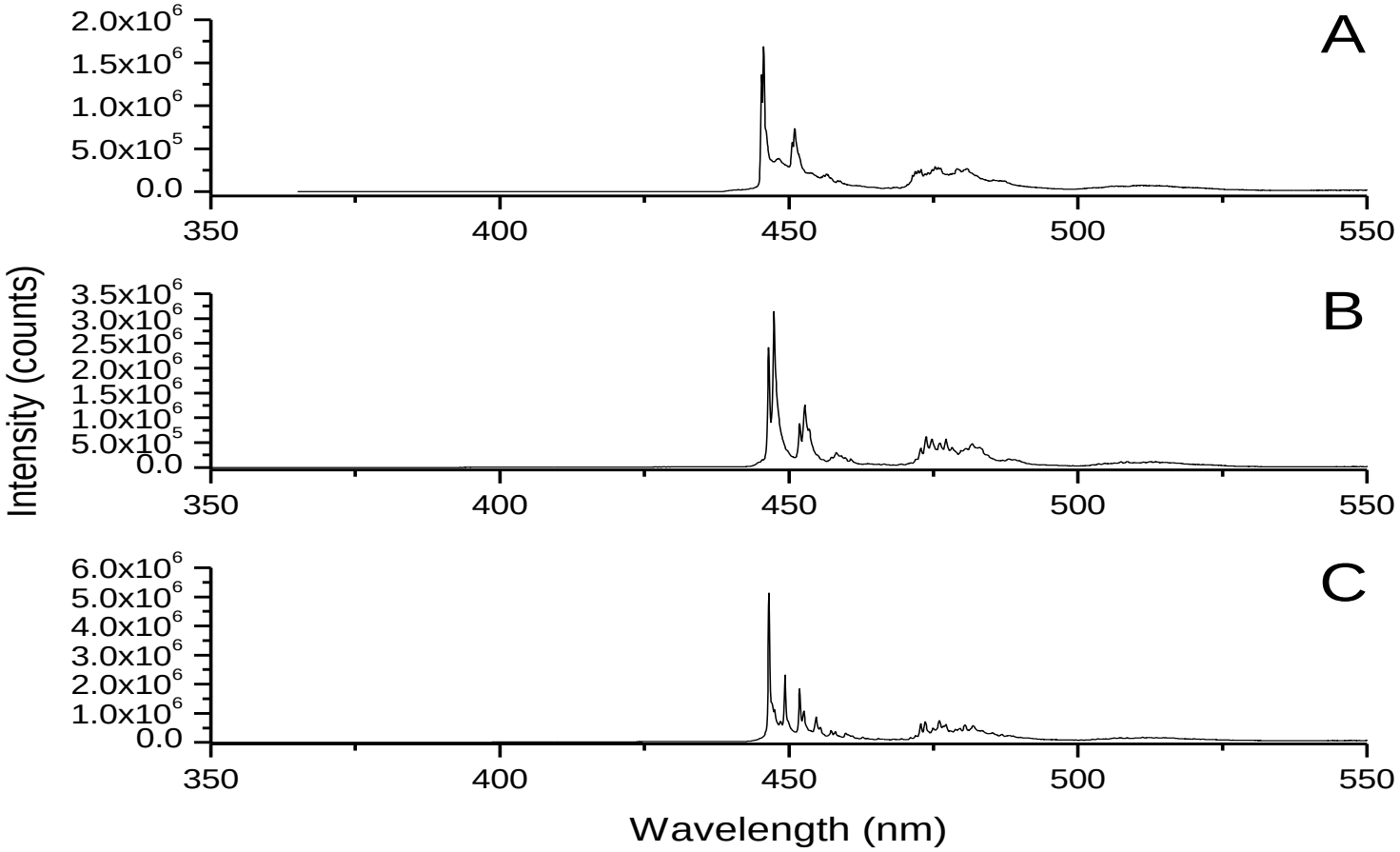

Figure B-5. 4.2 K LETRSS fluorescence spectra of 100 ng mL^{-1} DB[*a,h*]P standard were recorded in (A) n-octane; λ_{ex} = 310.0 nm, (B) n-nonane; λ_{ex} = 310.0 and (C) n-decane; λ_{ex} = 310.0 nm using a 0 ns delay and 15 ns gate time. All spectra correspond to the accumulation of 100 laser pulses. The spectrograph slit was 42 μm.

APPENDIX C: FLUORESCENCE DECAYS OF HMW-PAHS IN DIFFERENT N-ALKANE SOLVENTS AT 4.2K

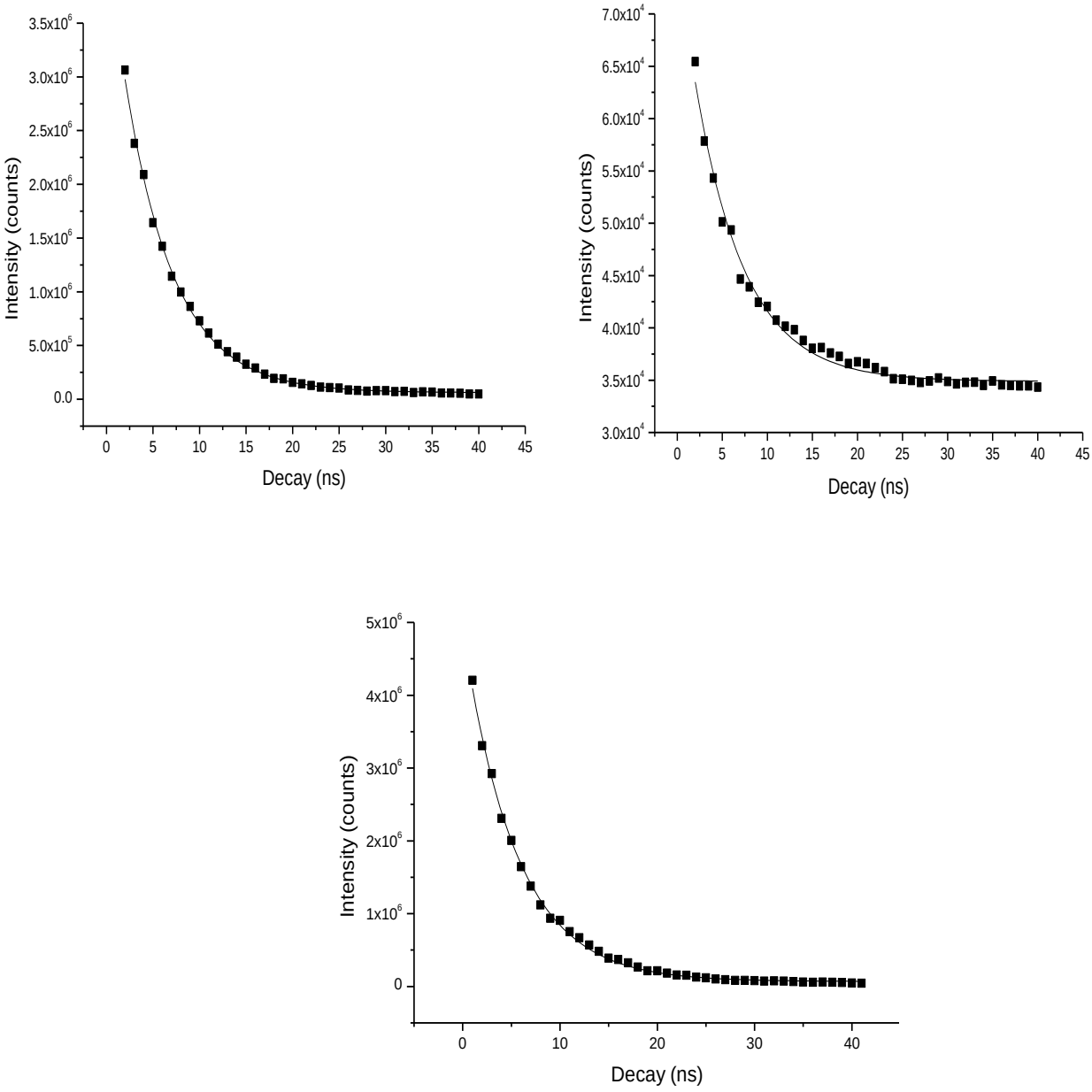

Figure C-1. Fluorescence decay of Db[*a,l*]P in (A) n-octane, (B) n-nonane and (C) n-decane at 4.2k

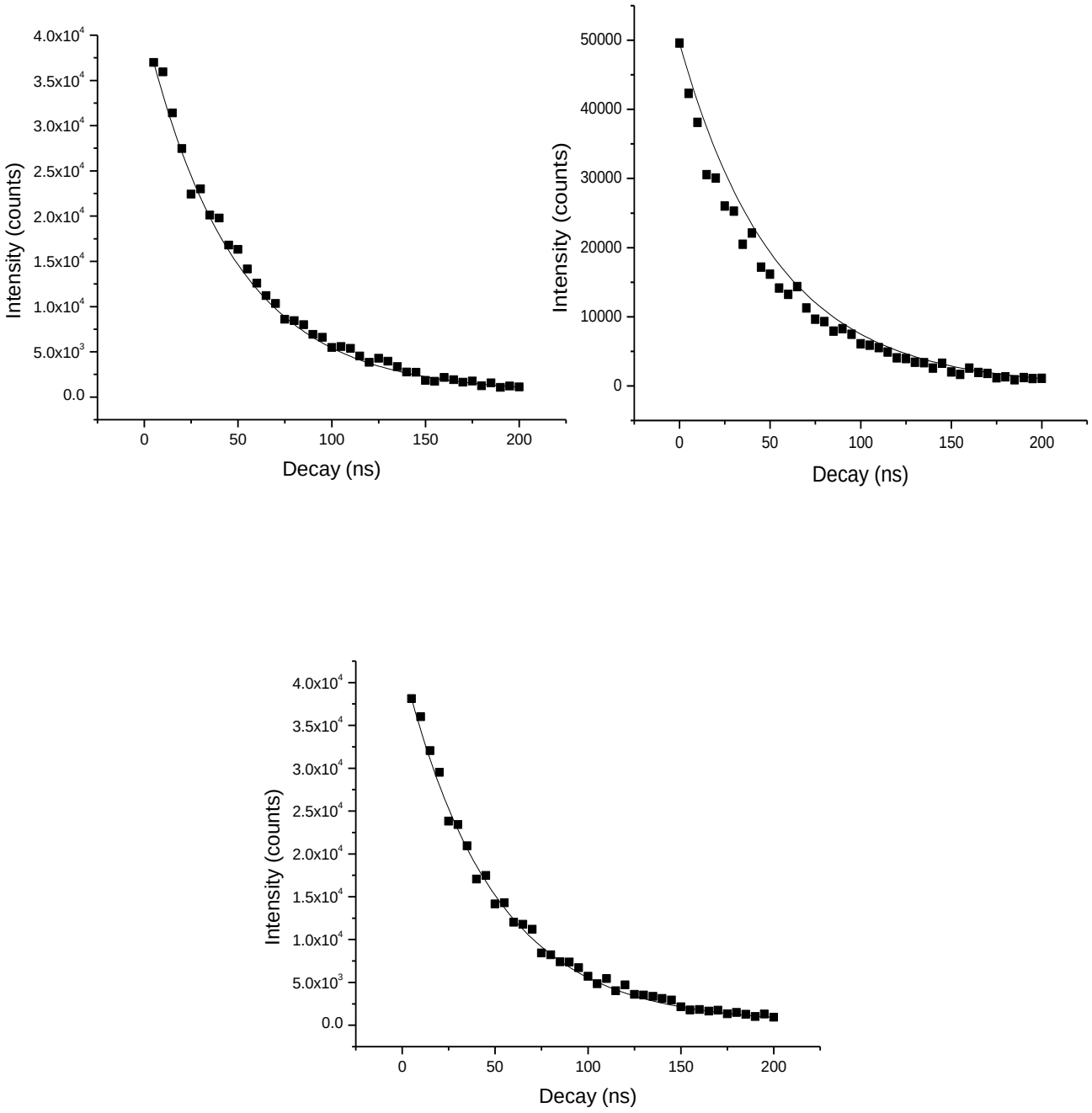

Figure C-2. Fluorescence decay of Db[*a*,*e*]P in (A) n-octane, (B) n-nonane and (C) n-decane at 4.2k

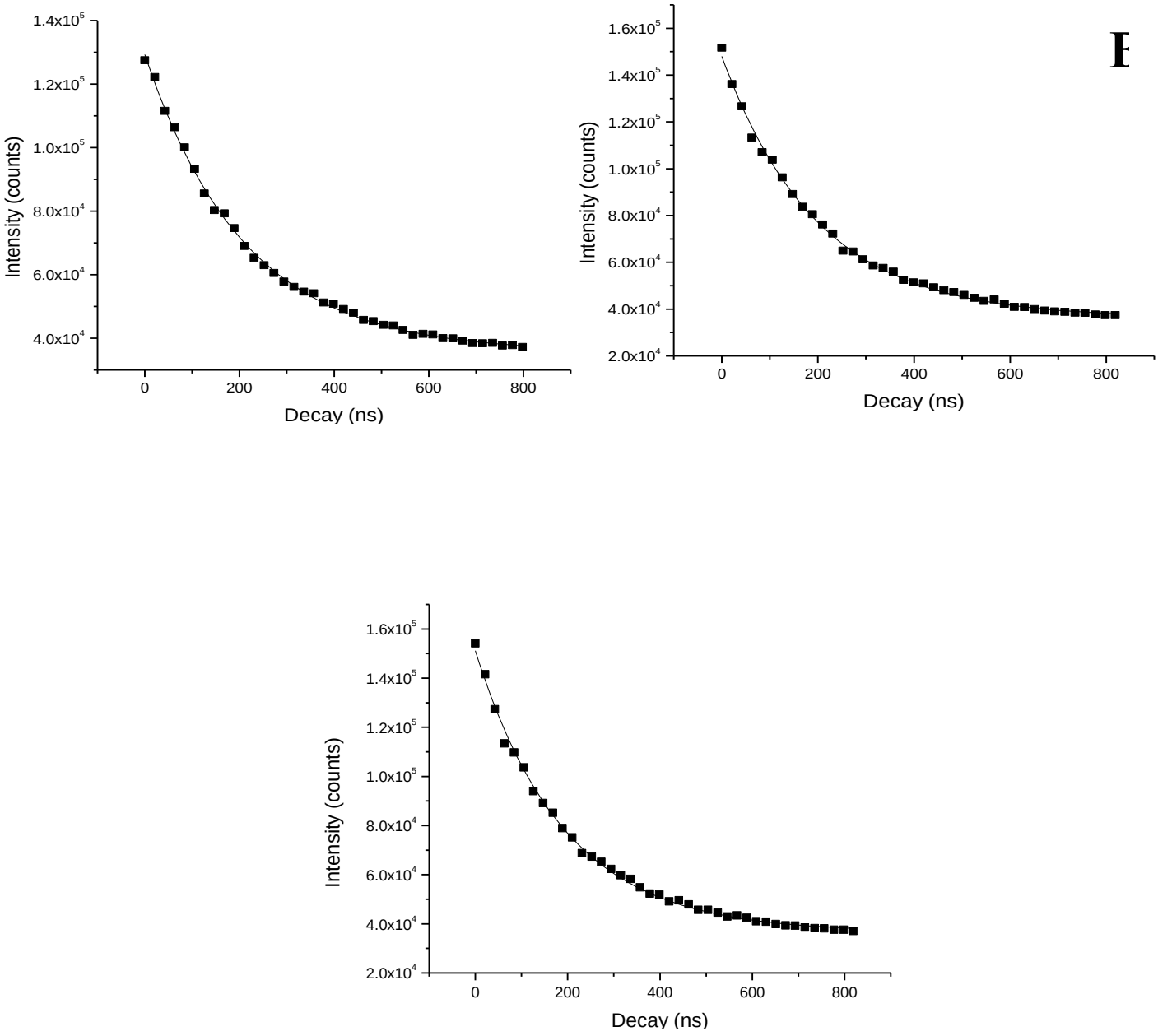

Figure C-3. Fluorescence decay of Db[*a,i*]P in (A) n-octane, (B) n-nonane and (C) n-decane at 4.2k

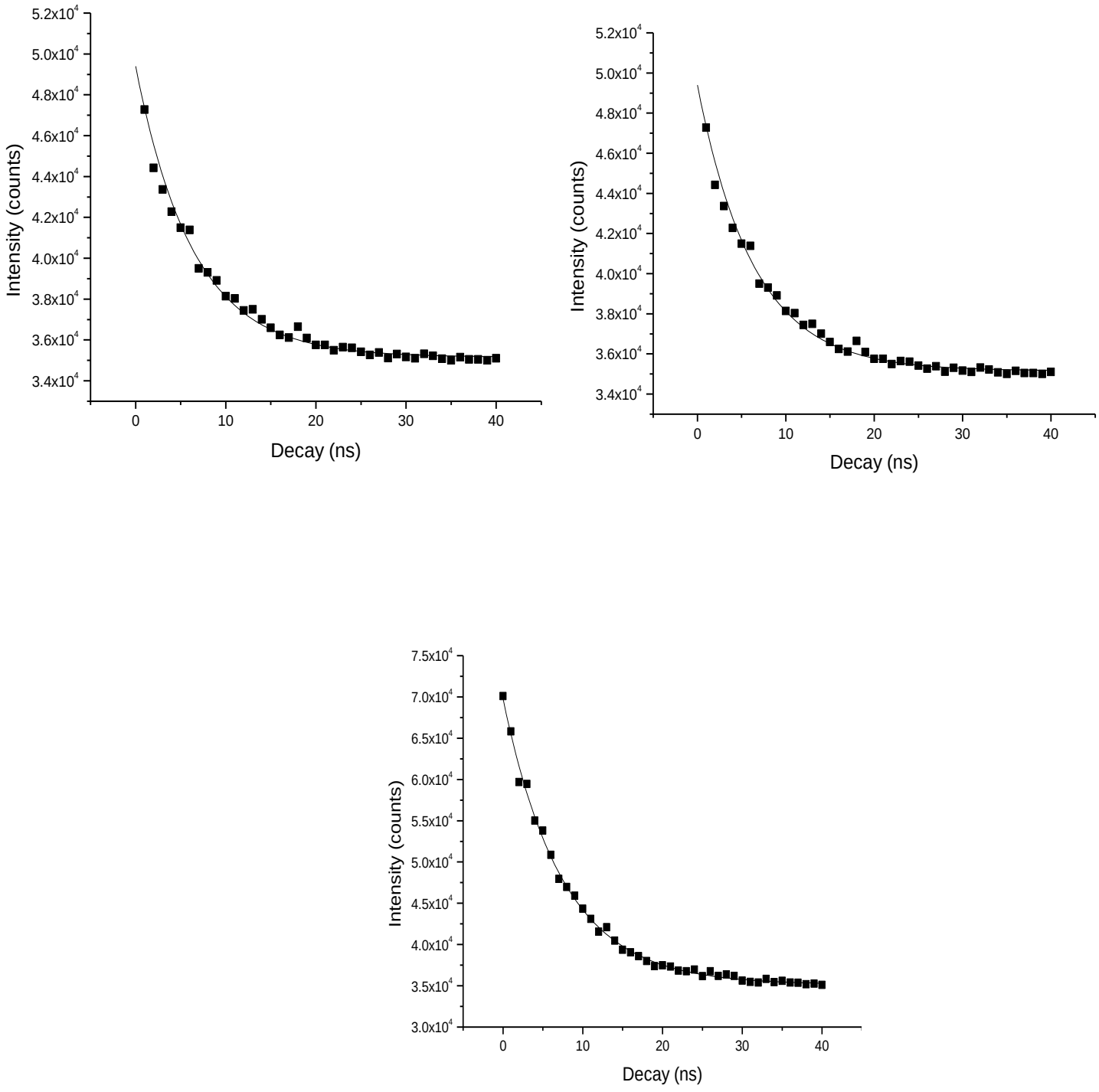

Figure C-4. Fluorescence decay of N[*2,3-a*]P in (A) n-octane, (B) n-nonane and (C) n-decane at 4.2k

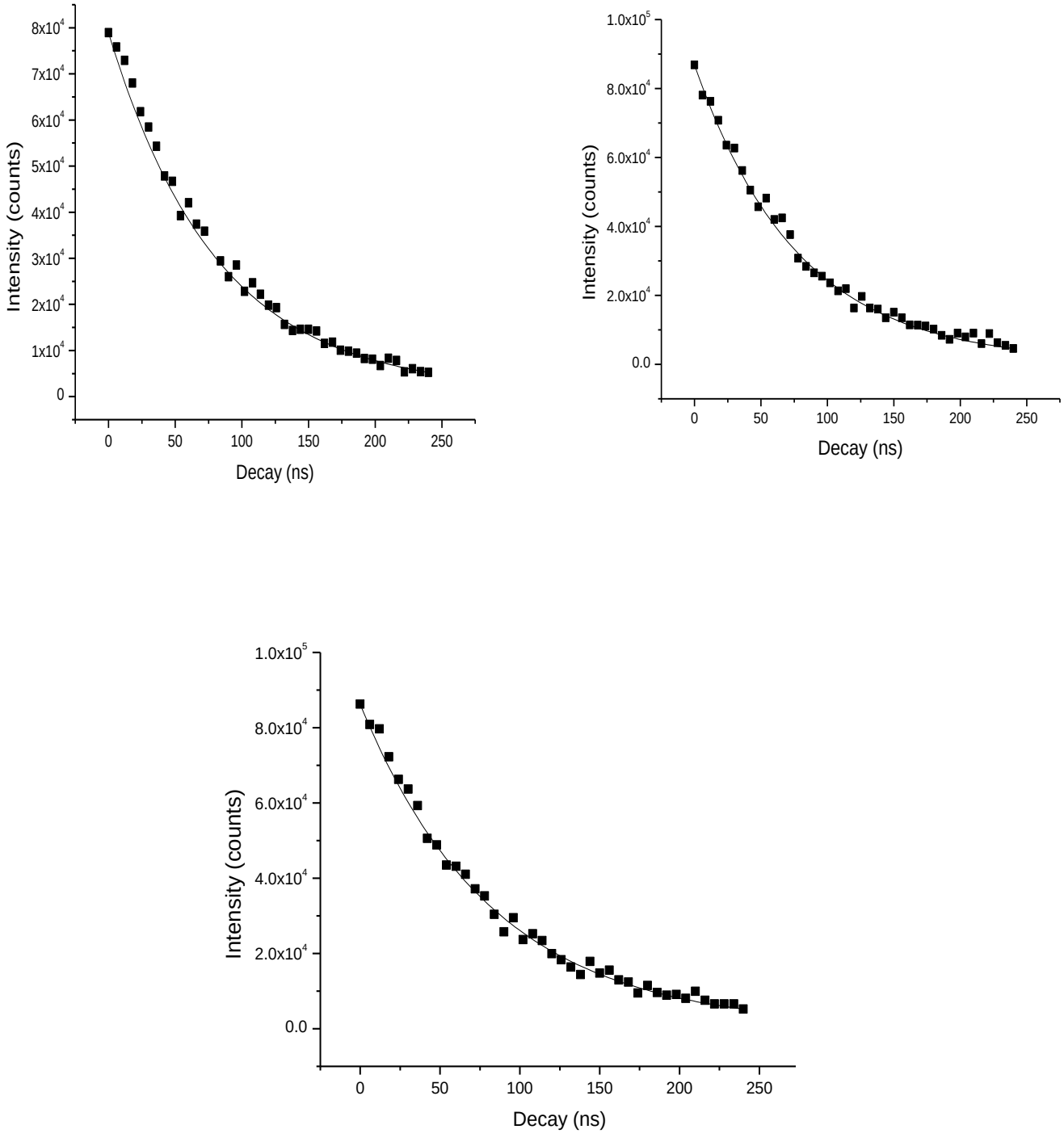

Figure C-5. Fluorescence decay of Db[*a*,*h*]P in (A) n-octane, (B) n-nonane and (C) n-decane at 4.2k

APPENDIX D: CALIBRATION CURVE OF HMW-PAHS AT 4.2K IN OPTIMUM SHPOL'SKII SOLVENT

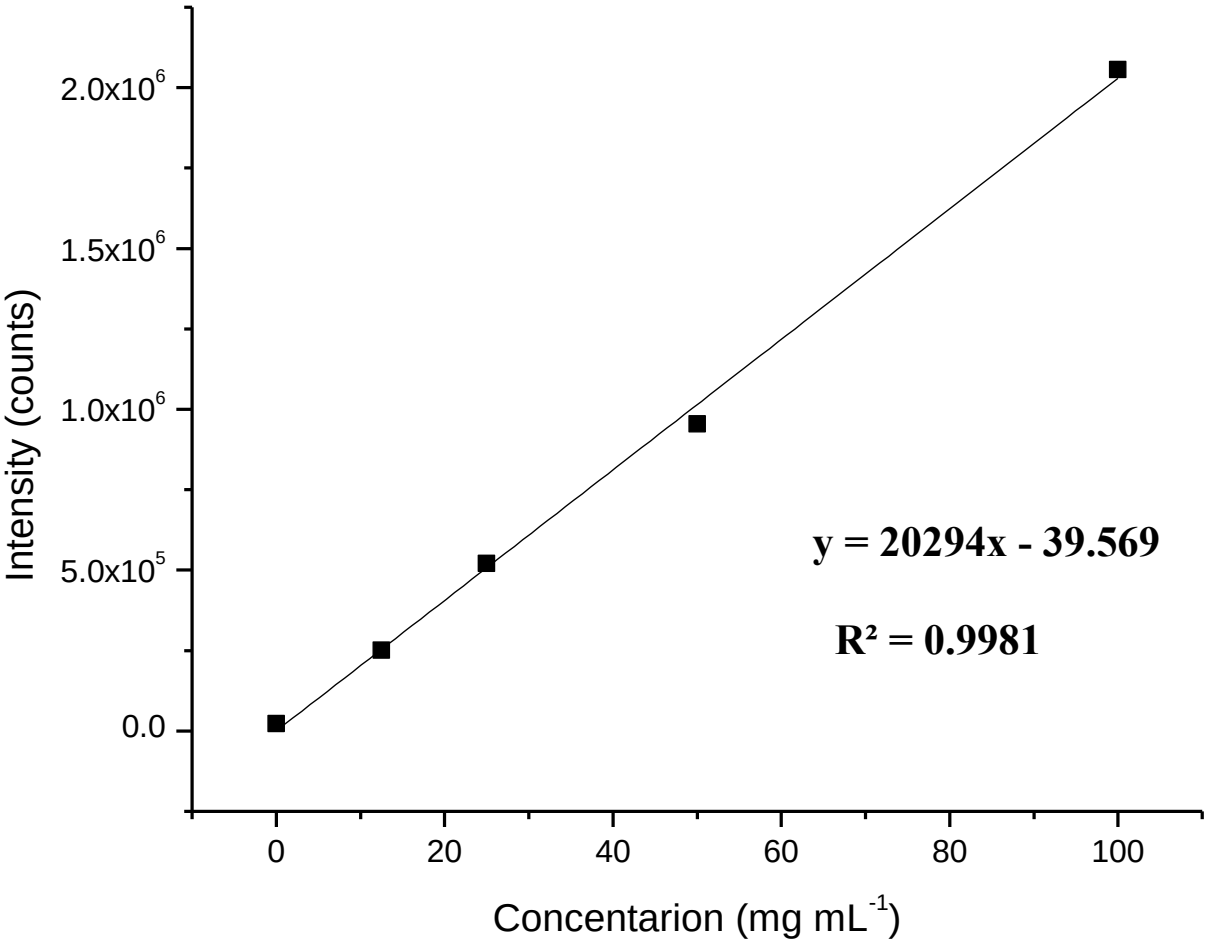

Figure D-1. Fluorescence intensity as a function of Db[*a,l*]P concentration at 4.2k in optimum Shpol'skii solvent

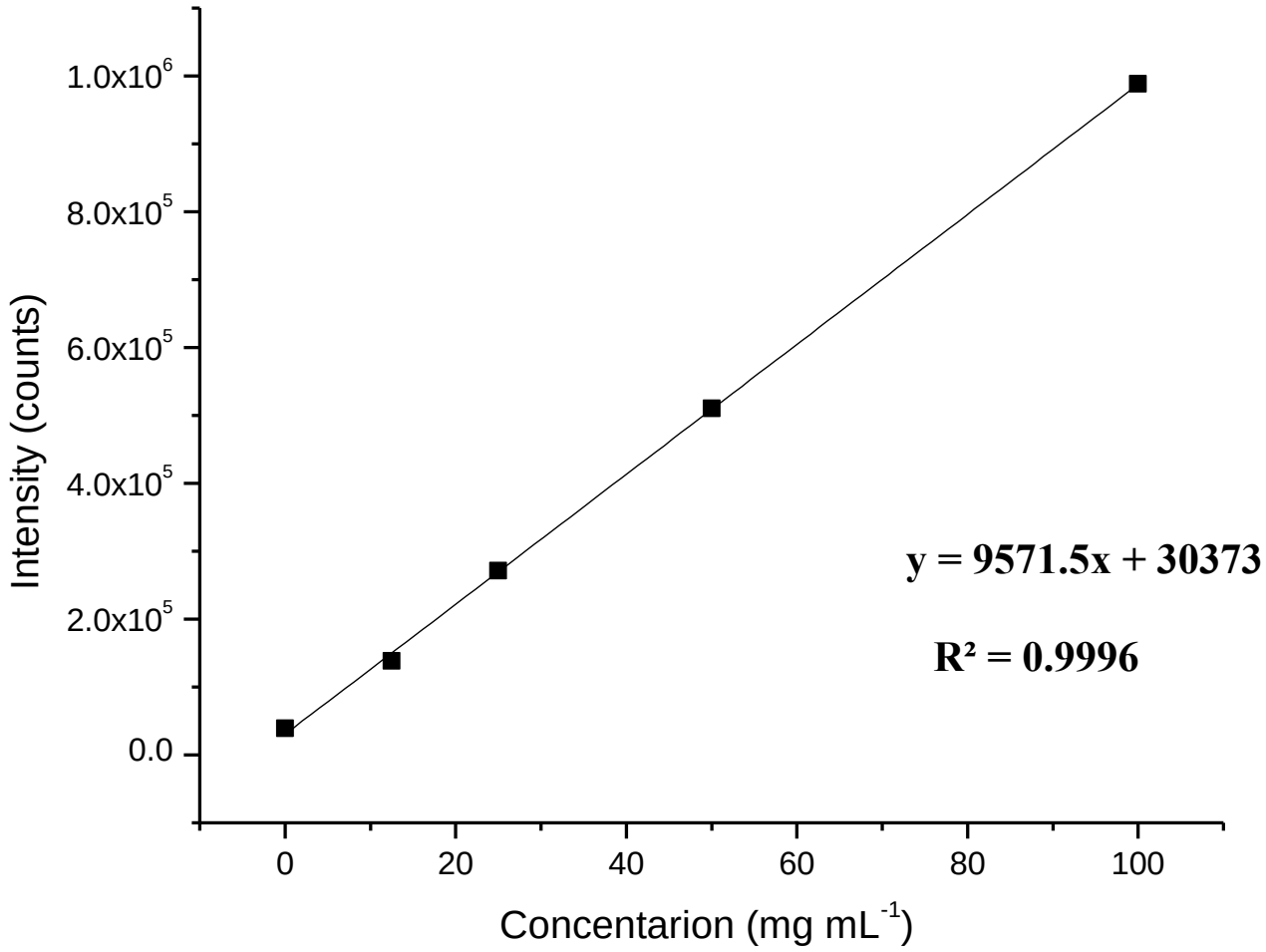

Figure D-2. Fluorescence intensity as a function of Db[*a,e*]P concentration at 4.2k in optimum Shpol'skii solvent

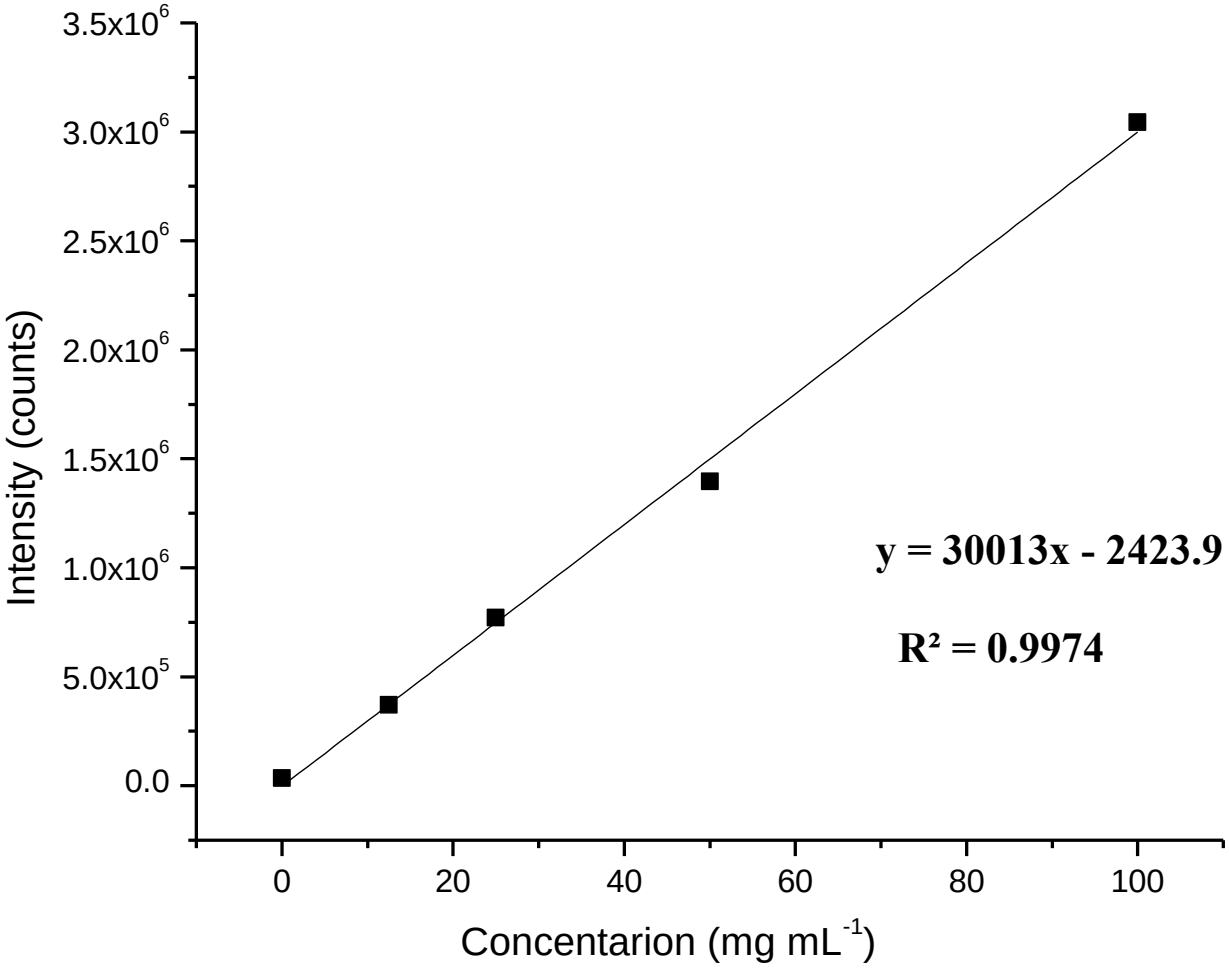

Figure D-3. Fluorescence intensity as a function of Db[*a,i*]P concentration at 4.2k in optimum Shpol'skii solvent

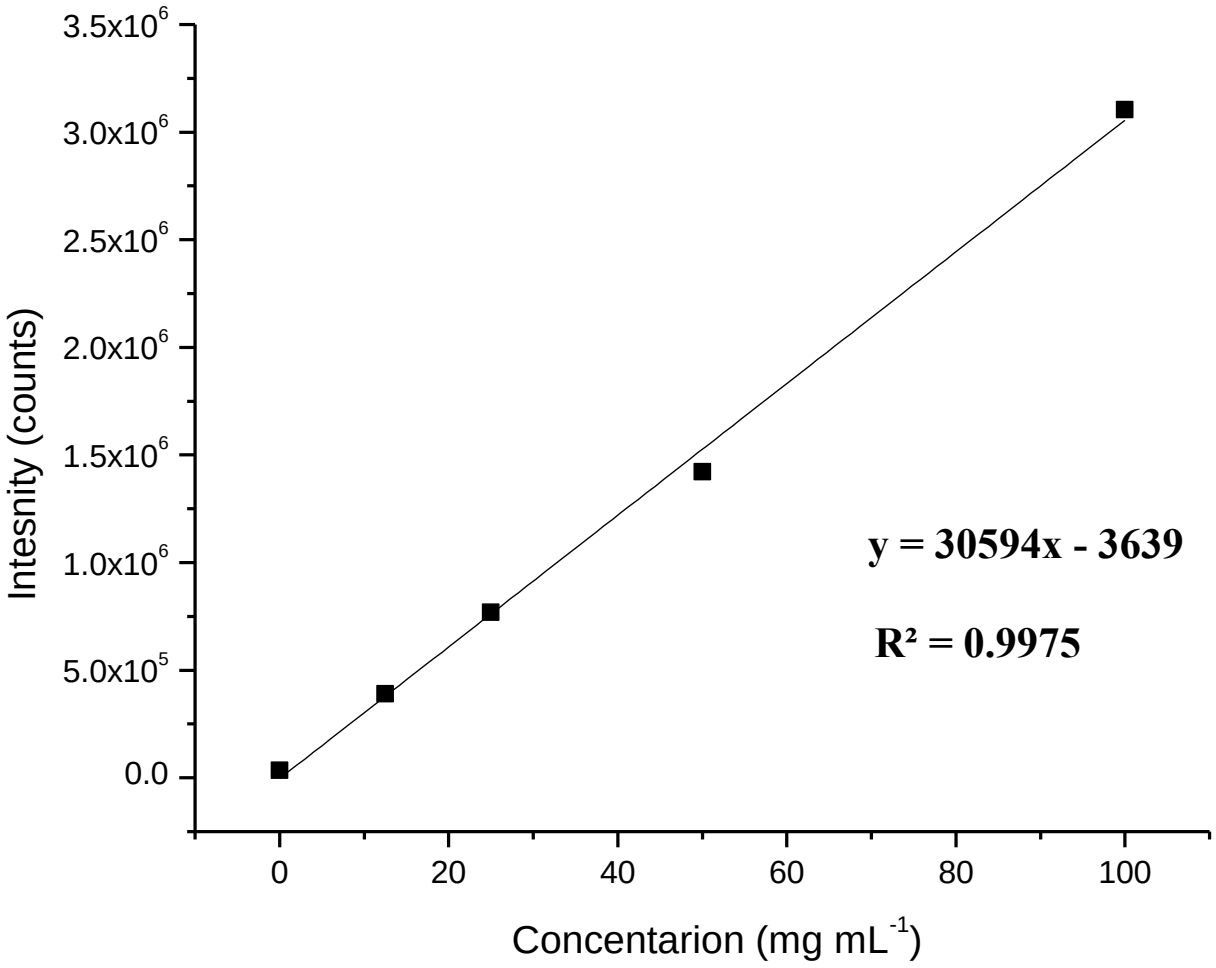

Figure D-4. Fluorescence intensity as a function of N[*2,3-a*]P concentration at 4.2k in optimum Shpol'skii solvent

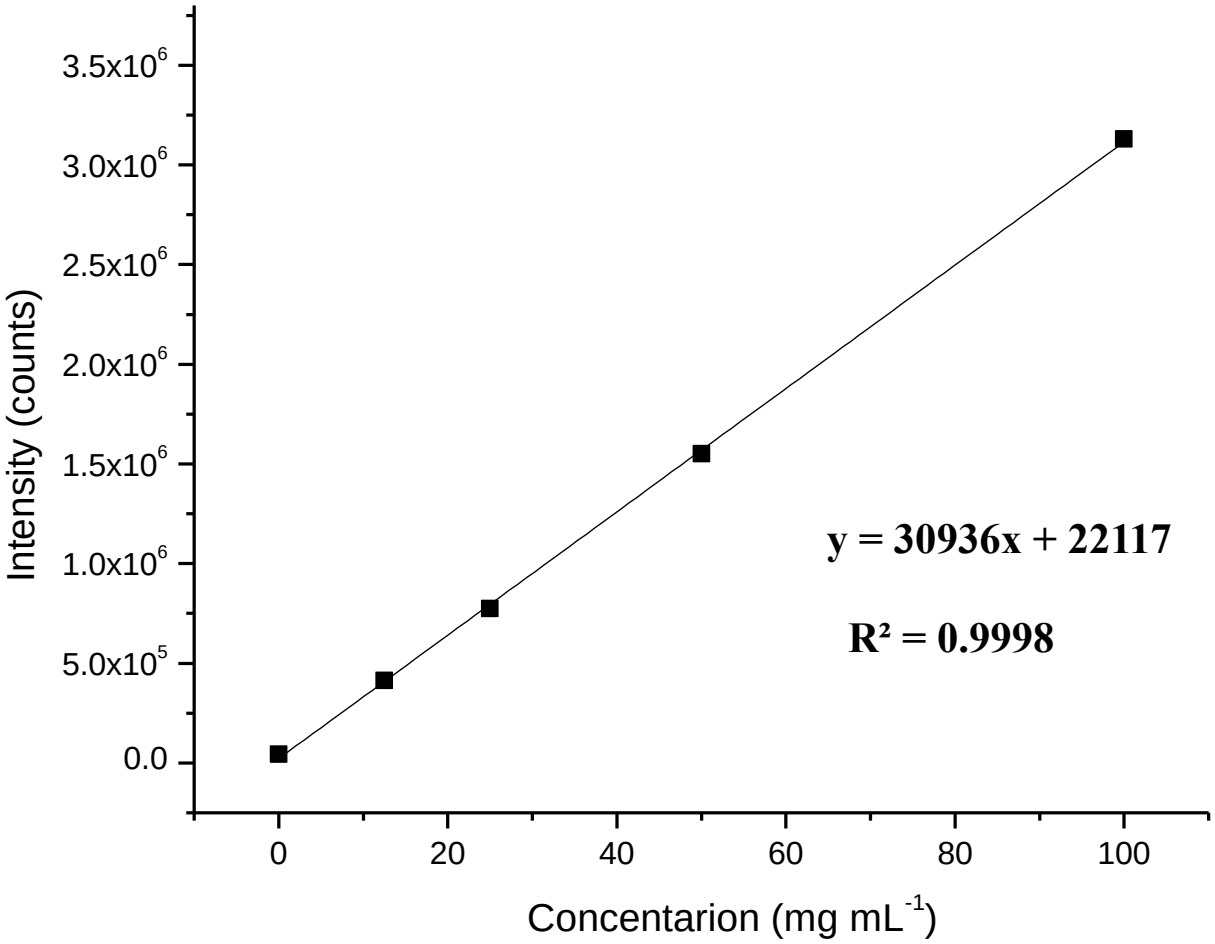

Figure D-5. Fluorescence intensity as a function of Db[*a,h*]P concentration at 4.2k in optimum Shpol'skii solvent

APPENDIX E: CALIBRATION CURVE GENERATED FROM EVAP-LETRSS

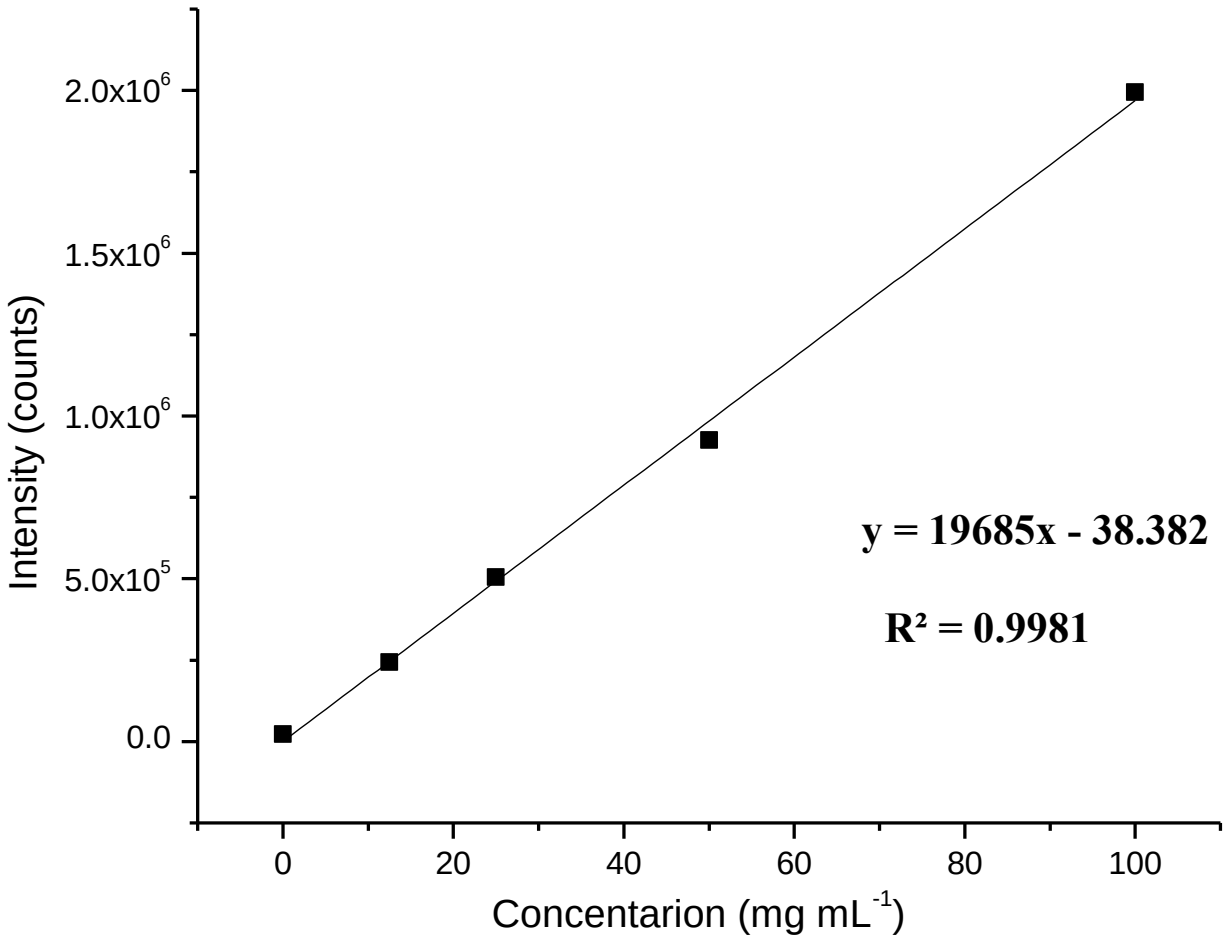

Figure E-1. Fluorescence intensity as a function of Db[*a,l*]P concentration using evaporation as pre-concentration then analysis by LETRSS

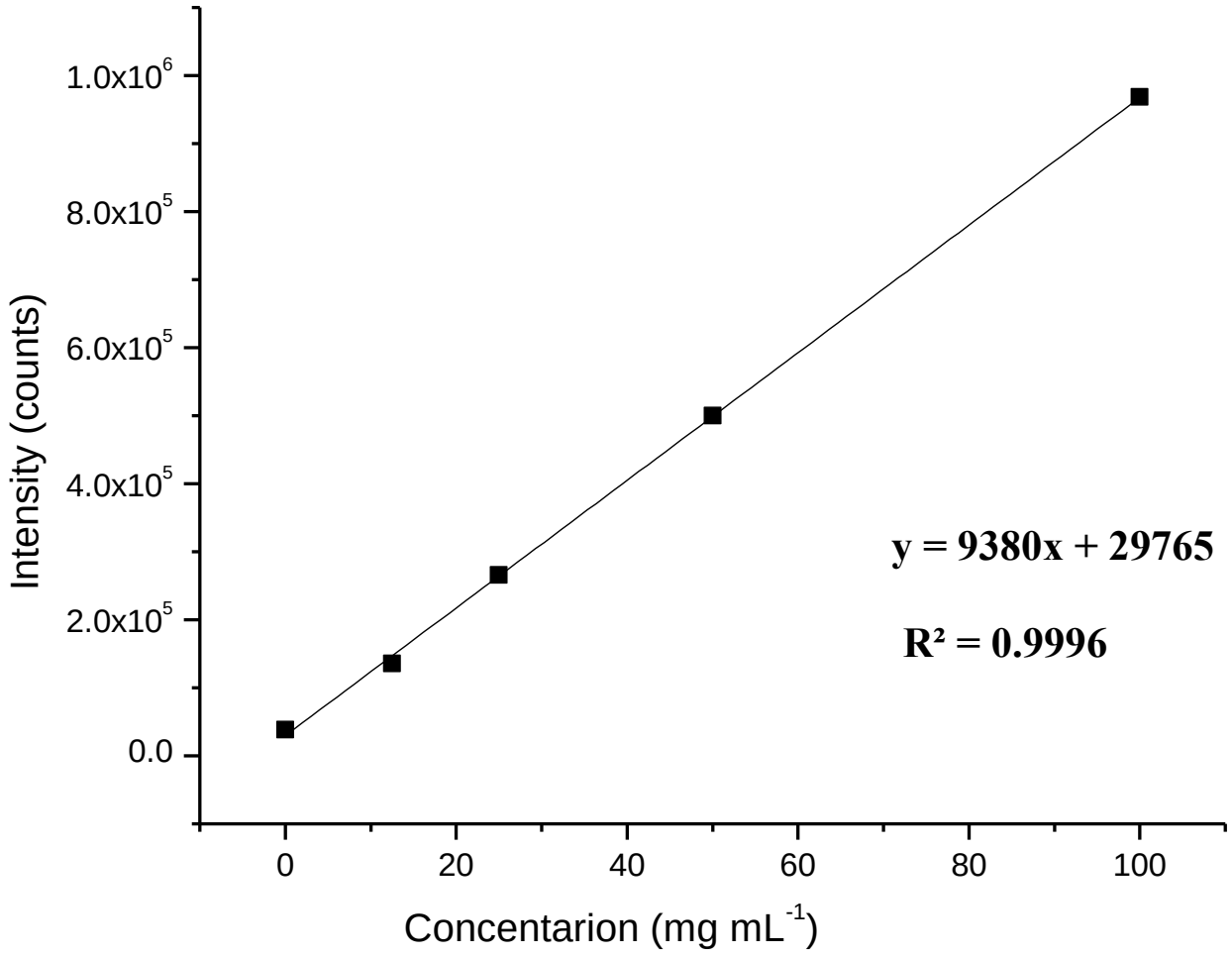

Figure E-2. Fluorescence intensity as a function of Db[*a,e*]P concentration using evaporation as pre-concentration then analysis by LETRSS

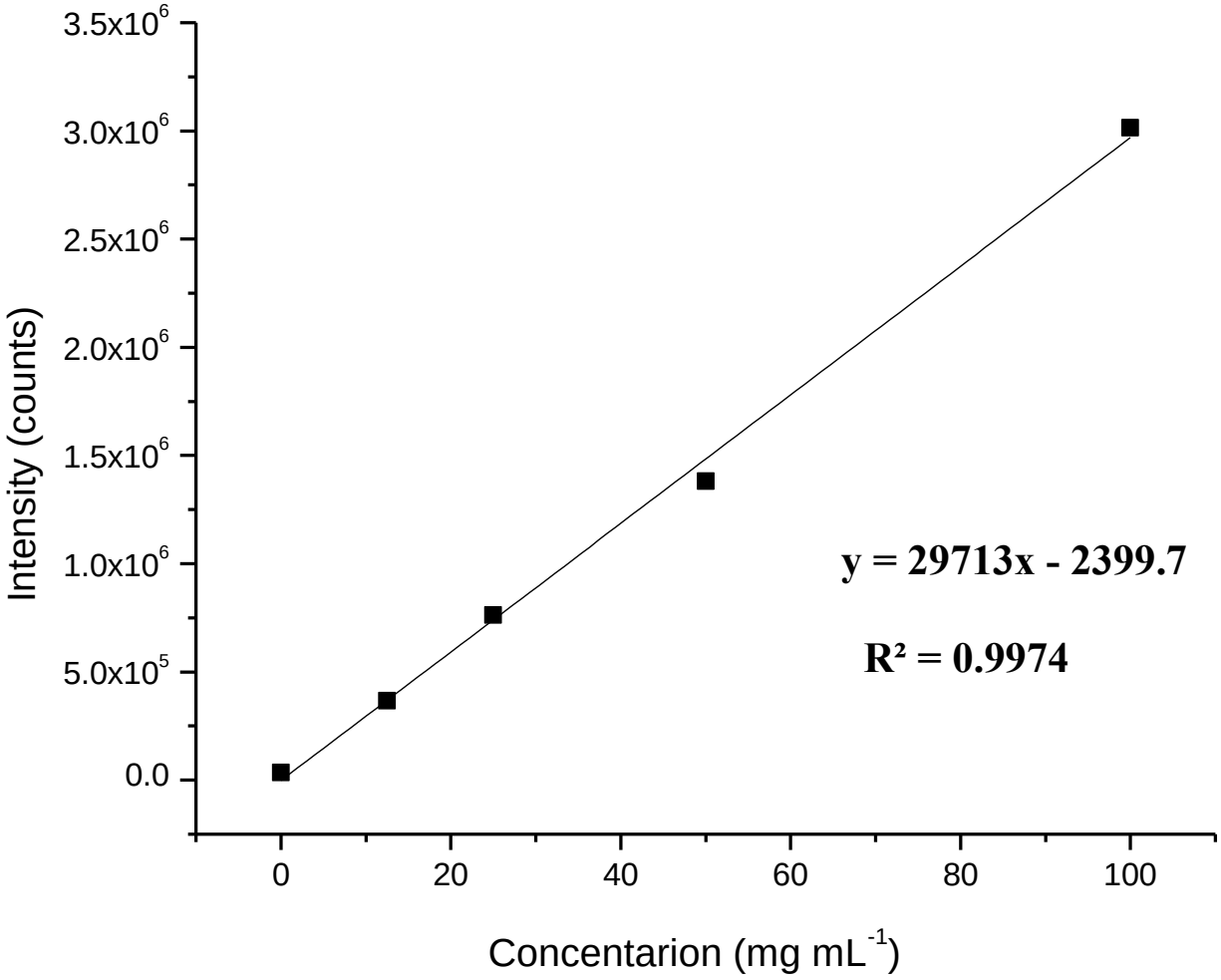

Figure E-3. Fluorescence intensity as a function of Db[*a,i*]P concentration using evaporation as pre-concentration then analysis by LETRSS

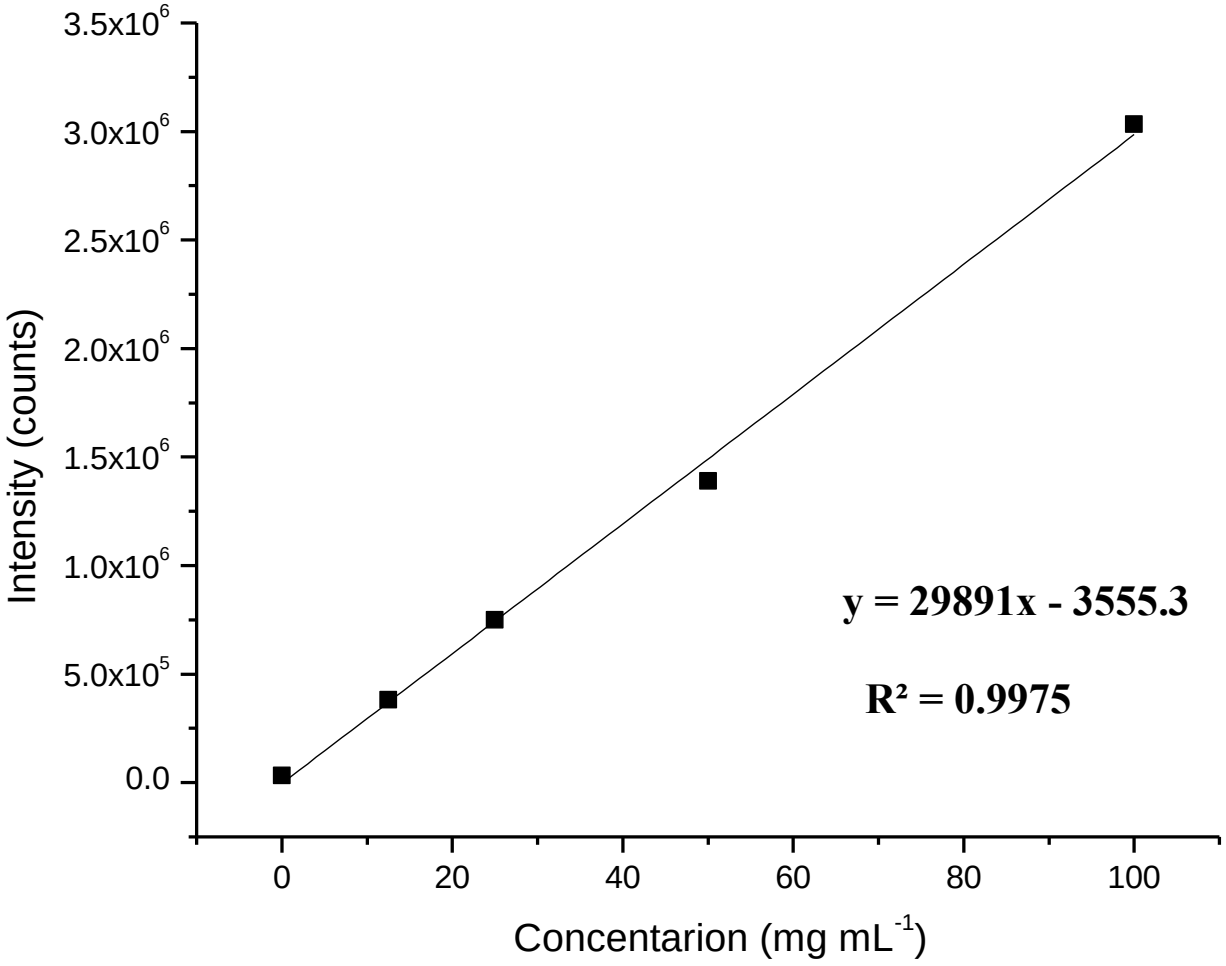

Figure E-4. Fluorescence intensity as a function of N[*2,3-a*]P concentration using evaporation as pre-concentration then analysis by LETRSS

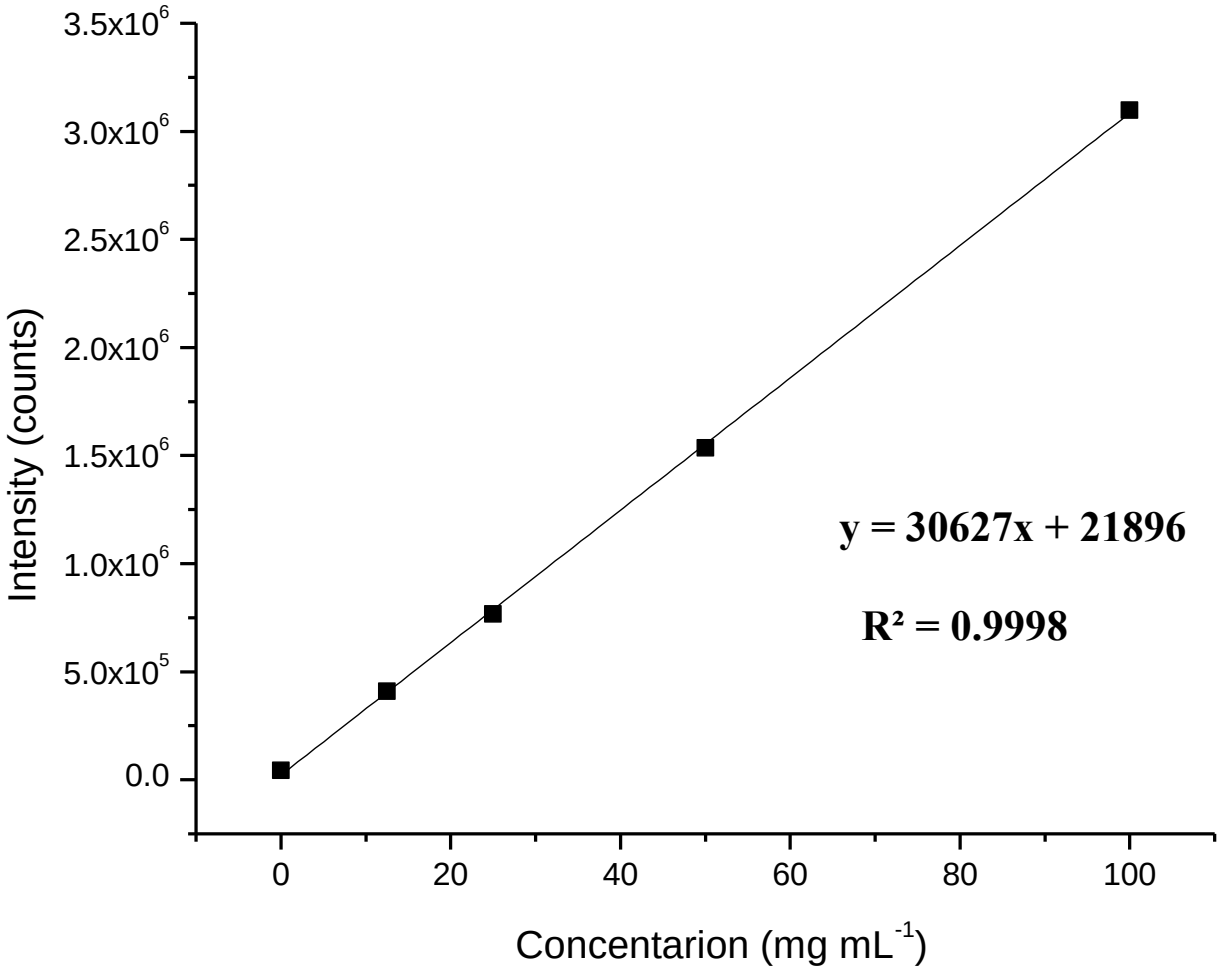

Figure E-5. Fluorescence intensity as a function of Db[*a,h*]P concentration using evaporation as pre-concentration then analysis by LETRSS

APPENDIX F: CALIBRATION CURVE GENERATED FROM SPNE-LETRSS

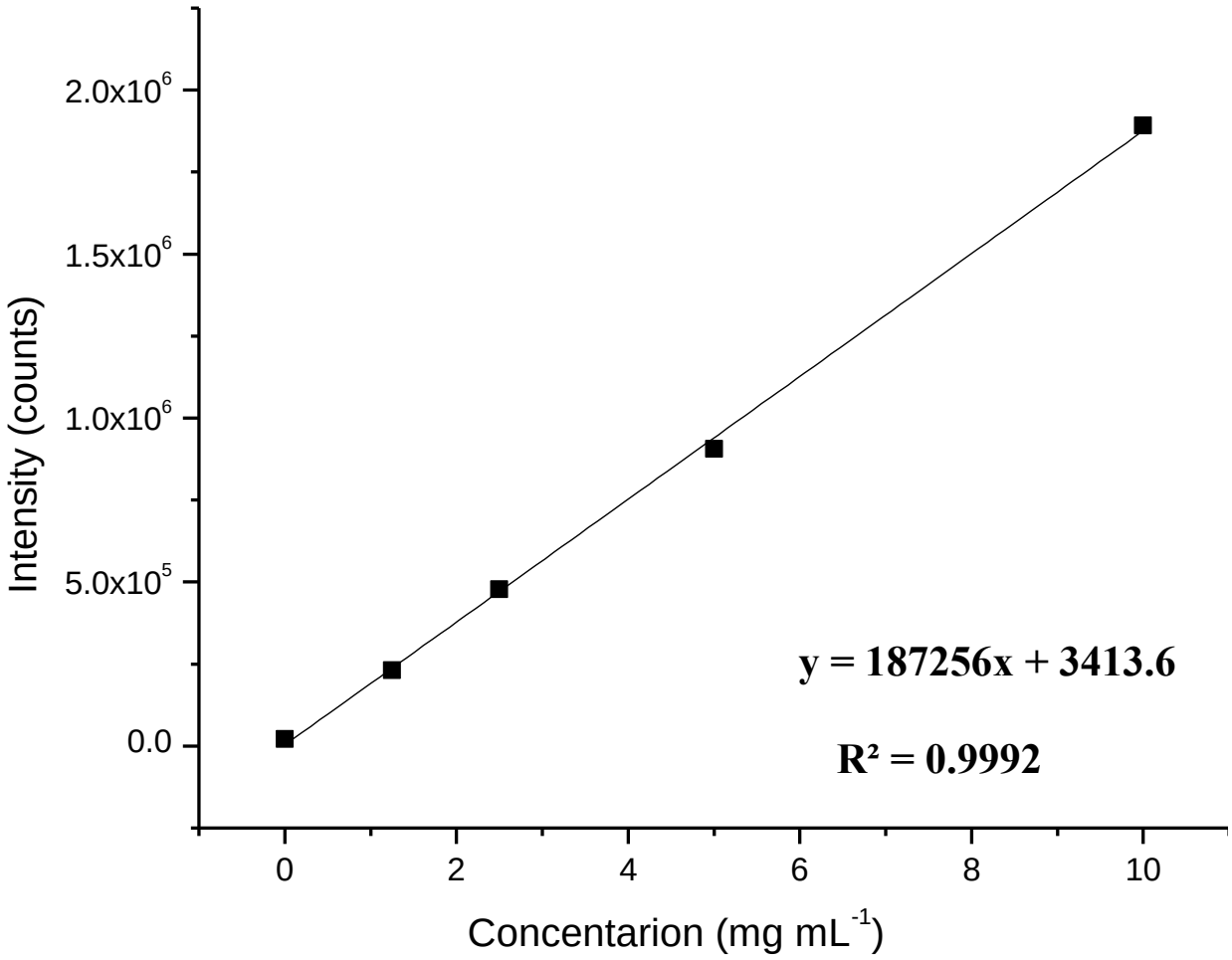

Figure F-1. Fluorescence intensity as a function of Db[*a,l*]P concentration using SPNE as pre-concentration then analysis by LETRSS

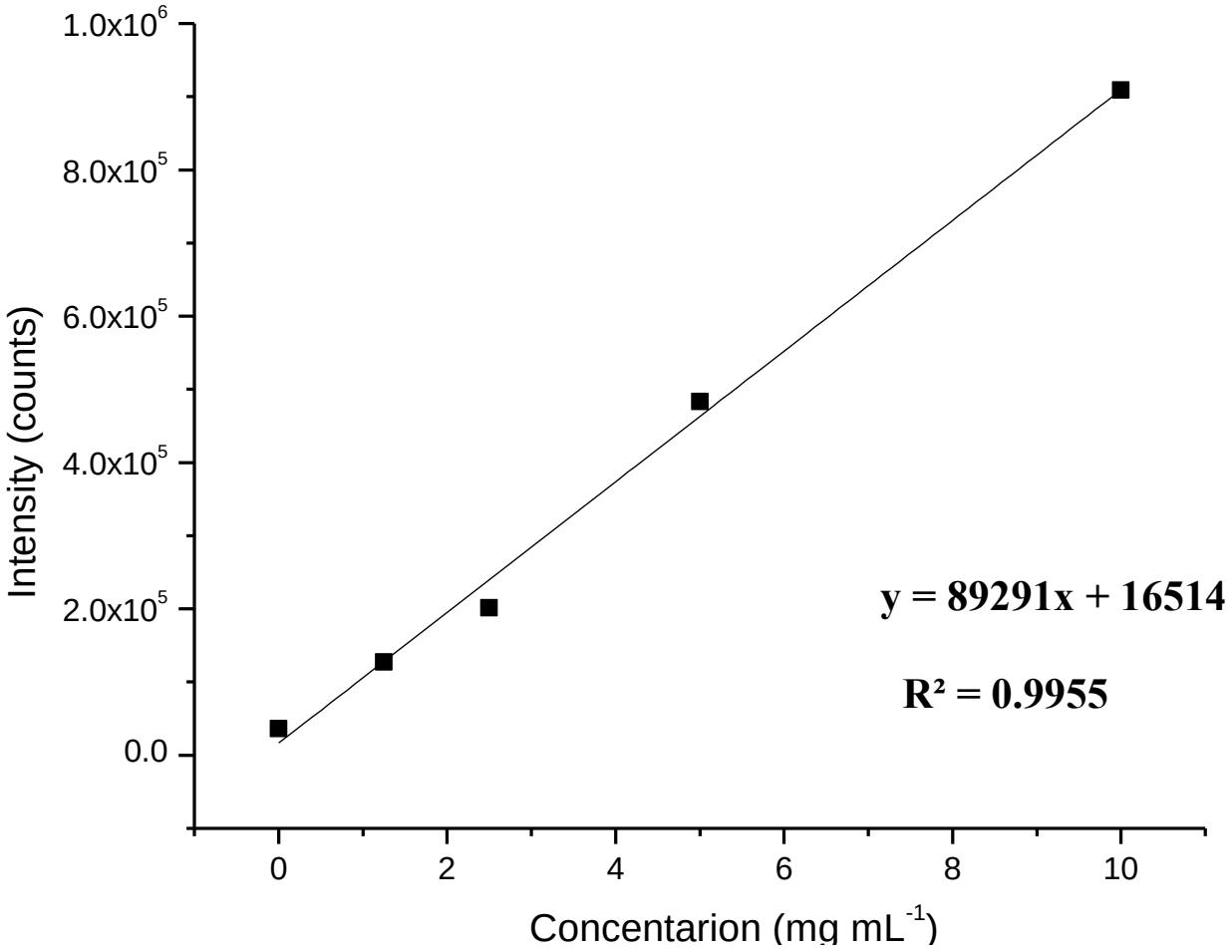

Figure F-2. . Fluorescence intensity as a function of Db[*a,e*]P concentration using SPNE as pre-concentration then analysis by LETRSS

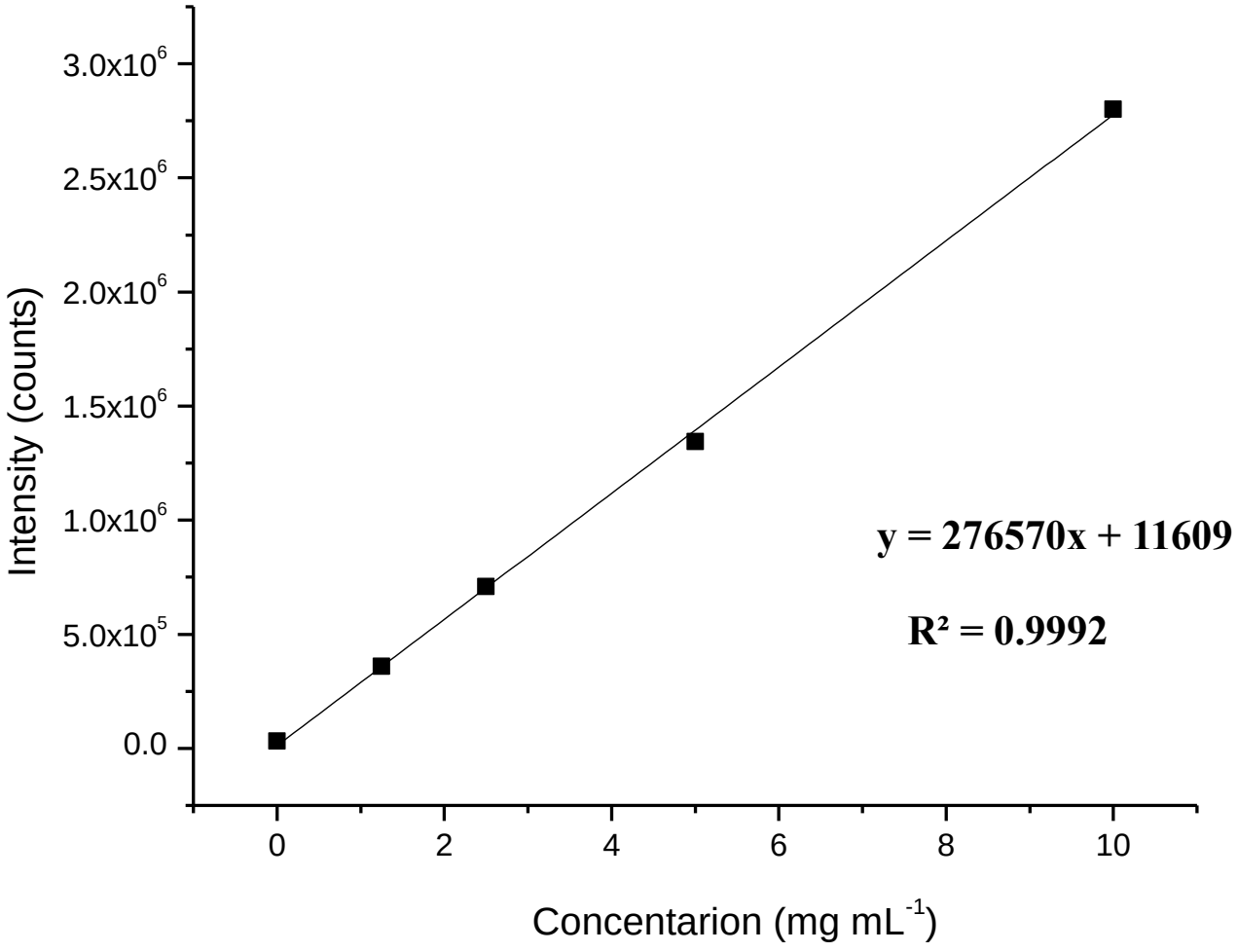

Figure F-3. Fluorescence intensity as a function of Db[*a,i*]P concentration using SPNE as pre-concentration then analysis by LETRSS

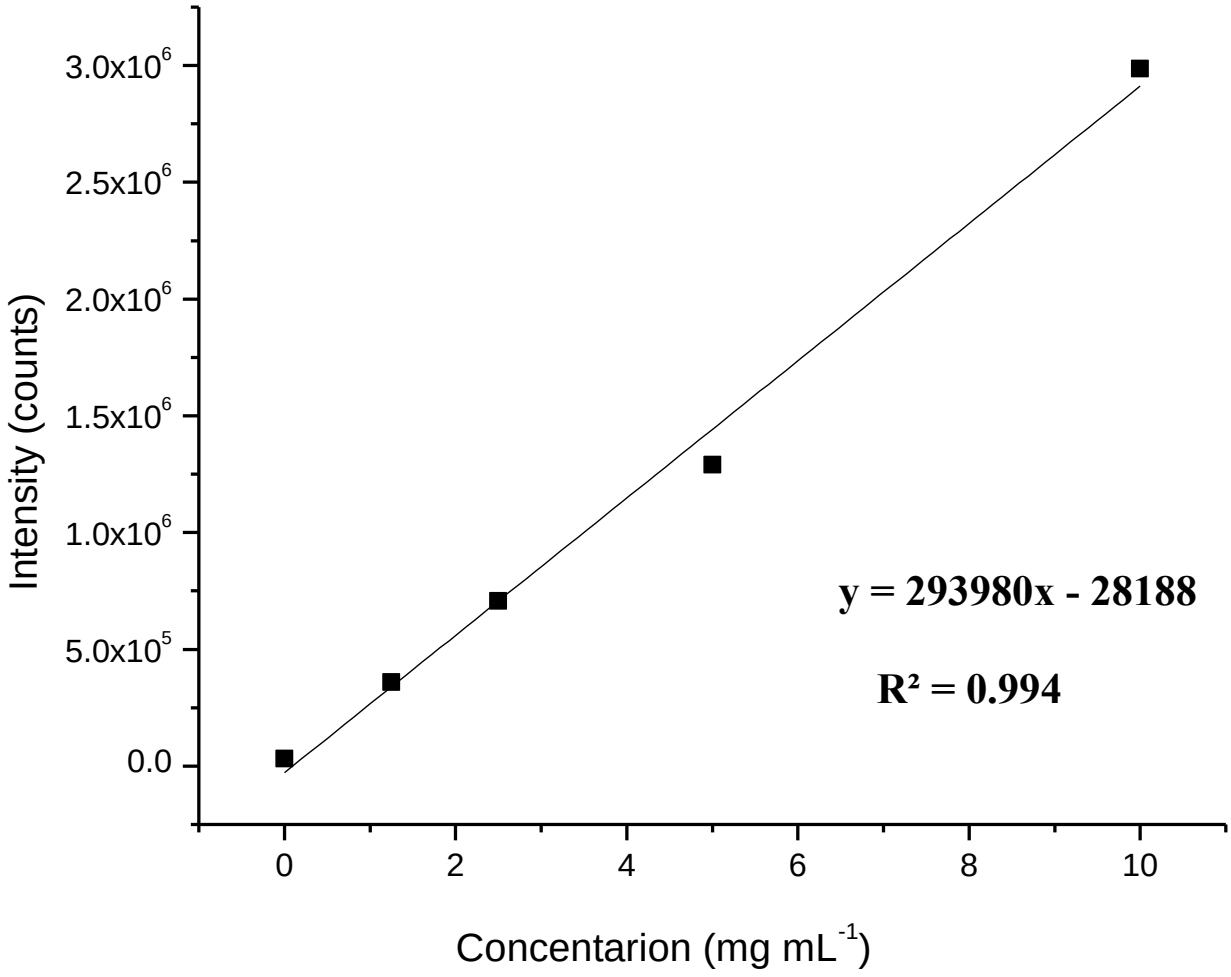

Figure F-4. Fluorescence intensity as a function of N[*2,3-a*]P concentration using SPNE as pre-concentration then analysis by LETRSS

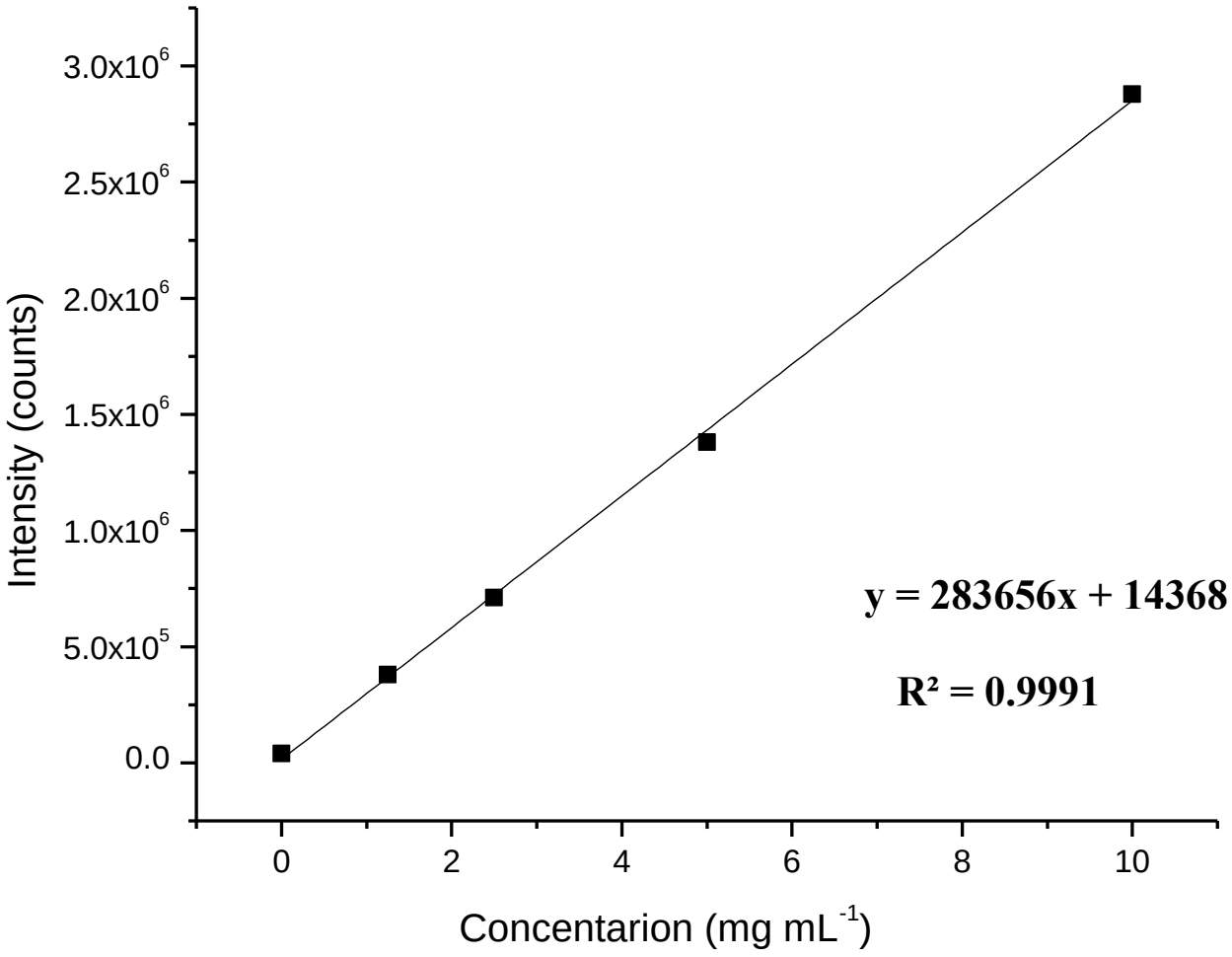

Figure F-5. Fluorescence intensity as a function of Db[*a,i*]P concentration using SPNE as pre-concentration then analysis by LETRSS

APPENDIX G: FLUORESCENCE DECAY OF HPLC FRACTIONS AT 4.2K

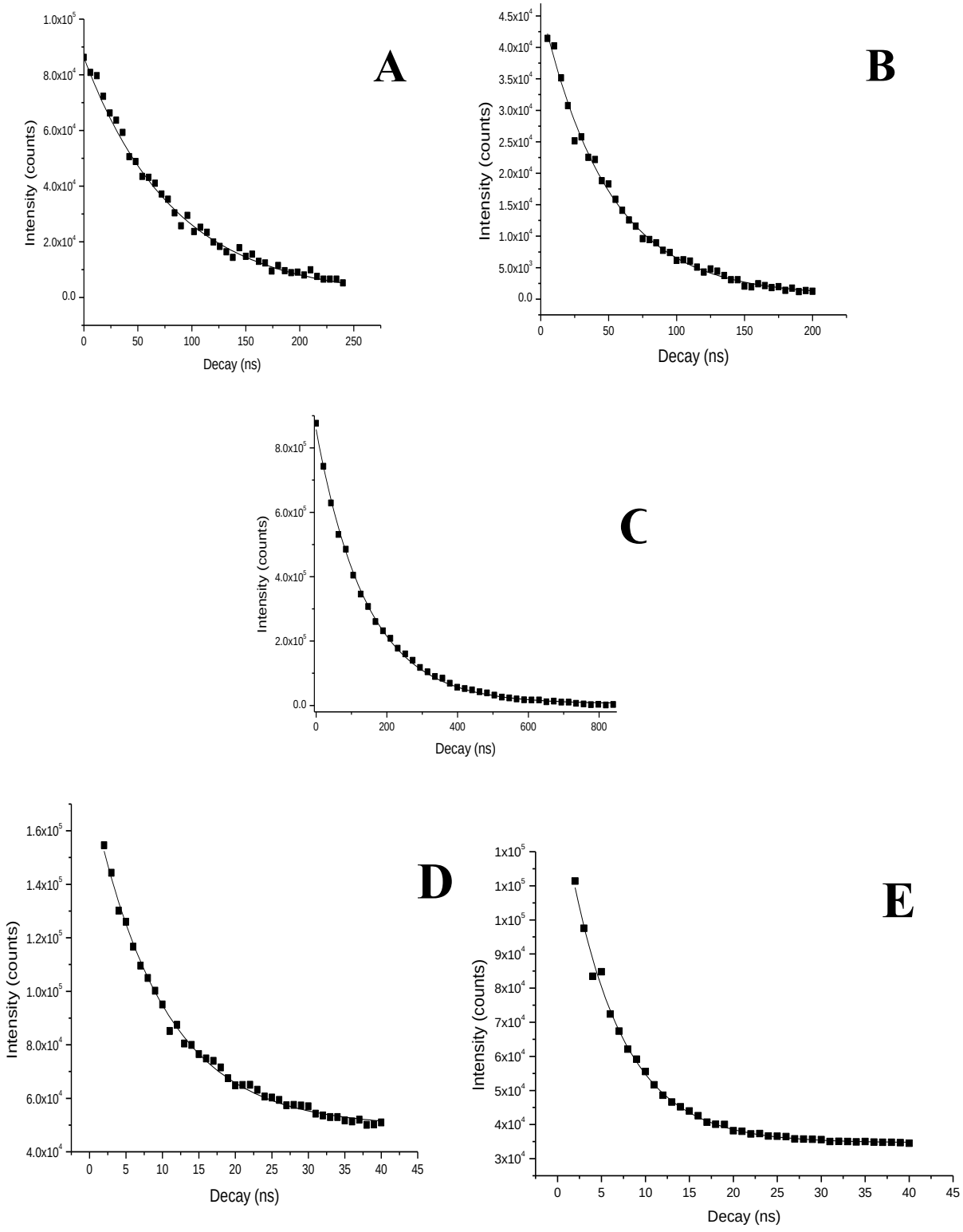

Figure G. Fluorescence decay of (A) Db[*a*,*l*]P, (B) Db[*a*,*e*]P, (C) Db[*a*,*l*]P, (D) N[*2*,*3*-*a*]P and (E) Db[*a*,*h*]P at 4.2k from HPLC fractions and in the optimum Shpol'skii solvent

LIST OF REFERENCES

(1) Skoog, D. A.; Holler, F. J.; Nieman, T. A. Principles of instrumental analysis. 6th edition.

(2) Lakowicz, J. R. Principles of fluorescence spectroscopy. New York 2nd edition.

(3) Orrit, M.; Bernard, J. Phys. Rev. Lett. 1990, 65, 2176.

(4) Renge, I.; Wild U.P. in Shpol'skii Spectroscopy and Other Site-Selection Methods,

(5) Lamotte, M. in Shpol'skii Spectroscopy and Other Site-Selection Methods, Gooijer, C., Ariese, F., Hofstraat, J.W. (Eds.) Wiley Interscience 2000, Chapter 3.

(6) Atkins, P. W.; Paula, J. d. "Physical Chemistry", Oxford University Press, New Yourk, 2002, section 16.3.

(131) Hurtubise, R.J., Phosphorimetry: Theory, Instrumentation, and Applications. 1990, New York: VCH Publishers Inc.

(132) Hurtubise, R., Solid Surface Luminescence Analysis: Theory, Instrumentation, Applications. 1981, New York: Marcel Dekker Inc.

(133) Bateh, R.P., Room Temperature phosphorescence some diagnostic studies in its application to biochemical and drug analysis, 1982, University of Florida: Gainesville, FL.

(134) Algarra, M., et al. Analytical and Bioanalytical Chemistry, 2005. 382(4): p. 1103-1110.

(135) Eastwood, D., et al Analusis, 1994. 22(6): p. 305-310.

(136) Hagestuen, E.D., A.F. Arruda, and A.D. Campiglia. . Talanta, 2000. 52(4): p. 727-737.

(137) Hagestuen, E.D. and A.D. Campiglia. Applied Spectroscopy, 1998. 52(8): p. 1096-1102.

(138) Hagestuen, E.D. and A.D. Campiglia. Talanta, 1999. 49(3): p. 547-560.

(139) Ariese, F., A.N. Bader, and C. Gooijer, Trens Anal. Chem., 2008. 27: p. 127.

(140) Bystol, A.J., J.L. Whitcomb, and A.D. Campiglia. . Environmental Science & Technology, 2001. 35(12): p. 2566-2571.

(141) Campiglia, A.D., A.J. Bystol, and S.J. Yu. Analytical Chemistry, 2006. 78(2): p. 484-492.

(142) Wang, H.Y. and A.D. Campiglia. Talanta, 2010. 83(1): p. 233-240.

(143) Poziomek, E.J., et al. Analytical Letters, 1991. 24(10): p. 1913-1921.

(144) Ackerman, A.H. and R.J. Hurtubise. 1999. 53(7): p. 770-775.

(145) Arruda, A.F. and A.D. Campiglia. Environmental Science & Technology, 2000. 34(23): p. 4982-4988.

(146) Arruda, A.F., et al. Environmental Science & Technology, 2003. 37(7): p. 1385-1391.

(147) Arruda, A.F. and A.D. Campiglia. Analytica Chimica Acta, 1999. 386(3): p. 271-280.

(148) Whitcomb, J.L. and A.D. Campiglia. Talanta, 2001. 55(3): p. 509-518.

(149) Vatsavai, K., H.C. Goicoechea, and A.D. Campiglia. Analytical Biochemistry, 2008. 376(2): p. 213-220.

(150) Eilers, P.H.C., Parametric time warping. Analytical Chemistry, 2004. 76(2): p. 404-411.

(151) Goicoechea, H.C., et al. Talanta, 2011. 83(4): p. 1098-1107.

(152) Jongeneelen, F.J., et al. Health, 1985. **57**(1): p. 47-55.

(153) *MATLAB 7.6.0*, 2008, The Math Works: Natick,MA.

(154) Currie, I.D., M. Durban, and P.H.C. Eilers. B-Statistical Methodology, 2006. **68**: p. 259-280.

(155) J. Bradley Hochalter, Yan Zhong, Shaomei Han. Chem.Res. Toxicol, 2011, 24, 262.

(156) Yan Zhong, Steven G. Carmella. Res. Toxicol. 2011, 24, 73.

(157) Miche`le bouchard and Claude Viau. Toxicology and applied pharmacology, 1996, 139, 301.

(158) Ainsley Weston , Regina M. Santella. Polycyclic Aromatic Compounds, 1994, 5, 241.

(159) Jin J. Wang, David G. Frazer. Anal .Chem. 2003, 75, 5953.

(160) Danzer, K., L.A. Currie, and C. Commission Gen Aspects Analyt, *Guidelines for calibration in analytical chemistry - Part 1. Fundamentals and single component calibration (IUPAC recommendations 1998).* Pure and Applied Chemistry, 1998. **70**(4): p. 993-1014.

(161) Korina C.W, Hector C.G., A. D. Campiglia. Talanta. 2011, 85, 1805-11.

(162) Keerthika V., Hector C. G. and Andres D. Campiglia. Analytical Biochemistry. 2008, 376, 213-220.

(163) J. B. Hochalter, Y. Zhong, S. Han, S. Carmella and S. Hecht. Chemical Research in Toxicology, 2011, 24, 262-268.

(164) Y. Zhong, S. Carmella, S. Balbo, Chem. Res. Toxicol. 2011, 24, 73–80 73.

(165) S. S. Hecht, S. G. Carmella, P. W. Villalta, and J. B. Hochalter, Chem. Res. Toxicol. 2010, 23, 900–908.

(166) X. Zhyang, H. Hou, W. Xiong and Q. Hu, Journal of Analytical Methods in Chemistry Volume 2015 (2015), Article ID 514320.

(167) M. Bouchard and C. Viau, Toxicology and Applied Pharmacology, 1996, 139, 301–309.

(168) W. Lee, H. Shin, J. E. Hong, H. Pyo and Y. Kim. Bull. Korean Chem. Soc. 2003, Vol. 24, No. 5.

(169) Wang, Y., W. Zhang, and Y. Dong. Anal. Bioanal. Chem. 2005. **383**, 804.

(170) Kuusimaki, L., et al. International Archives of Occupational and Environmental Health. 2004. **77**(1), 23-30.

(171) Wang, H., W.B. Wilson, and A.D. Campiglia, J. Chromatogr. A. 2009, 385, 249.

(172) A. Likhachev, D. Beniashvili , K. Bykov , O. Kazanova , N. Loktionova , M. Tyndyk , Yatsuk OS, V. Yermilov, M. Zabezhinski. Int Arch Occup Environ Health. 1993, 65(1), 155-8.

(173) A. Weston, R. Santella, E. Bowman. Polycyclic Aromatic Compounds, 1994, 5, 241-247.